Investigating multiple sulfur isotope variations in active hydrothermal chimneys and fluids from the Arctic Mid Ocean Ridges

Master of Science Thesis

Lotte Hammer Johannessen

Department of Earth Science

University of Bergen

May 2022

Abstract

The four different vent fields Seven Sisters, Soria Moria, Fåvne and Loki's Castle are all located on the ultra-slow spreading AMOR. The Seven Sisters and the Soria Moria vent fields are located on the southern part of the AMOR. Here the ridges are influenced by the Icelandic hostspot resulting in higher magma supply, higher spreading rates, and thicker crust compared to the northern parts of the ridges. Fåvne and Loki's Castle vent fields are located further north where the ridges have a limited magma supply, thinner crust, deeper water depths and exposed ultramafic mantle rocks. There is relatively scarce knowledge on subsurface processes in ultra-slow spreading related hydrothermal systems. Since sulfur plays a major role in the circulation system of high temperature hydrothermal systems, its multiple stable isotopes are used as a tool to gain knowledge about their subsurface processes.

Multiple sulfur isotopes were measured in sulfides and fluid samples from active high temperature chimneys in the four different vent fields Seven Sisters, Soria Moria, Fåvne and Loki's Castle. This thesis explored how variations in the geological settings (magmatic input, sedimentary input, host rocks, fluid temperature, and depth) of the vent fields were reflected in the sulfur isotope ratios, to increase our understanding of hydrothermal sulfur cycling along the AMOR. The framework for interpreting the isotopic composition in sulfides were the combination of the anhydrite buffer model and the two-component mixing model, to distinguish between the different reactions in the circulation system that affected the isotopic composition of sulfides.

The combined $\delta^{34}S$ and $\Delta^{33}S$ data from high-temperature hydrothermal fluids and sulfide minerals in the four vent fields on the AMOR demonstrates that variations in their geological setting are reflected in the multiple sulfur isotope ratios. Multiple sulfur isotope data reveal variation in reaction zone temperatures (250°C, 270°C, 350°C, 450°C) for the four investigated vent fields, that appears to be correlated to vent field depth. Their difference in reaction zone temperature appears to affect them to have varying contribution of sweater sulfate of 0%, 10%, 30% and 50% to the isotopic composition of sulfides, though this is also affected by rock type that fluids interact with. The multiple sulfur isotope data also indicate that isotope exchange between anhydrite- or barite-derived sulfate and sulfide does not reach equilibrium at the AMOR vent fields, despite the wide range of subsurface temperatures (250°C-450°C).

Acknowledgments

First and foremost, I would like to give a great thanks to my supervisor Desiree Lisette Roerdink for guiding me through this project. I am very grateful for all the help, positivity, and support. Thank you for always being available for discussions and answering my questions.

I would also like to thank my co-supervisors John W. Jamieson from Memorial University of Newfoundland and Eoghan P. Reeves for answering questions and shearing their knowledge and data. I would also like to thank Harald Strauss at Westfälishe Wilhelms-Universität Münster for conduction the multiple isotope analyses. Thank you to Apolline Maria Samin, Irene Heggstad and Leif-Erik Rydland Pedersen for helping me with lab-work and SEM-analyses.

Furthermore, thank you to the ROV crew and ship's crew of the R/V G.O. Sars for the 2017, 2018 and 2019 cruises which provided the samples for this project.

Thank you to Karen Elisabeth Moltubakk, Halfdan Arstein and Sanna Blakkestad for proofreading, cheering me up, and supporting me throughout this project. Also thank you to my family for supporting me and motivating me during this project.

Bergen, 09.05.2022

Lotte Hammer Johannessen

TABLE OF CONTENTS

CHAPTER 1: INTRODUCTION

Seafloor hydrothermal systems have a significant impact on the global biogeochemical cycles as they circulate the entire ocean every millions of years through the oceanic crust (Ono et al., 2007). They are also the creators of the largest and most valuable ore deposits on Earth and occur where there is a heat source, a permeable medium, and fluids saturating the crust (Hannington et al., 2005, Tivey, 2007). Originally hydrothermal activity was thought to only occur along fast spreading ridges, where spreading occurs in thin crust that is accompanied by frequent magmatic activity and a magma chamber present below the ridge axis where the rift valley is shallow and narrow (LaFemina, 2015, Hannington et al., 2005). However, this changed in 1985 when the Trans-Atlantic Geotraverse hydrothermal field was discovered at the slow-spreading Mid-Atlantic Ridge (Rona et al., 1986). Slow spreading ridges are characterized by less magmatic activity, a thicker crust and periods with tectonic extension and intrusive activity (Hannington et al., 2005). More recently, hydrothermal activity has also been found at the ultraslow spreading ridges Southwest Indian Ridge and the Arctic Mid Ocean Ridges (AMOR) (Edmonds et al., 2003, Baker et al., 2004, Pedersen et al., 2010a, Pedersen et al., 2010b, Tao et al., 2012). In contrast to fast spreading ridges, ultra-slow spreading ridges are characterized by intermittent volcanism and a wide axial rift valleys where spreading is accommodated by large detachment faults that can expose ultramafic mantle material (Dick et al., 2003, LaFemina, 2015). Since the discovery of abundant hydrothermal activity at the AMOR, and especially the 2010 discovery of the high temperature Loki's Castle vent field, it has risen a large interest in increasing the knowledge about the high temperature hydrothermal systems along these ultra-slow spreading ridges (Pedersen et al., 2010b, Pedersen et al., 2010a, Pedersen and Bjerkgård, 2016).

There is relatively scarce knowledge on subsurface processes in ultra-slow spreading related hydrothermal systems. Sulfur plays a major role in the circulation system of high temperature hydrothermal systems. Since the subsurface of active hydrothermal systems are hard to access directly, a useful tool to gain information about subsurface processes occurring in the circulation system is sulfur isotope signatures in fluids and mineral deposits (McDermott et al., 2015). Sulfur is affected by dissolution and precipitation reactions occurring in the recharge, reaction, and discharge zone of seafloor hydrothermal systems (Figure 1.1). In the recharge zone where cold seawater penetrates the crust, moves downward and is heated up, anhydrite

($CaSO_4$) precipitates when fluid temperatures reach 150°C due to reversible solubility of calcium sulfate (Tivey, 2007, Peters et al., 2010, Ono et al., 2007). At temperatures above 250°C, any remaining seawater sulfate can be reduced thermochemically to H_2S by Fe^{2+}-bearing minerals (olivine, pyroxene, pyrrhotite) present in the mafic or ultramafic ocean floor (Tivey, 2007, Ono et al., 2007, Seal et al., 2006). Fluids may interact with sediments which can lead to leaching of sulfide of biogenic origin into the fluids (Seal et al., 2006, McDermott et al., 2015). In the high temperature reaction zone (typically above 400°C), fluid-rock interactions result in the dissolution of sulfide from host rocks, and additional H_2S can be added by disproportionation of SO_2 in hydrothermal systems with silicic oxidizing magma bodies as a heat source (Tivey, 2007, Peters et al., 2010, McDermott et al., 2015). When the buoyant fluid flows back up to the seafloor in the discharge zone, dissolved sulfide can react or re-equilibrate with anhydrite if the flow rate is sufficiently slow (Tivey, 2007, Ono et al., 2007). At the seafloor, the drastic decrease in ambient temperatures lowers the solubility of metal sulfides, and dissolved sulfide will precipitate together with Fe, Cu and Zn in hydrothermal chimney structures (Tivey, 2007).

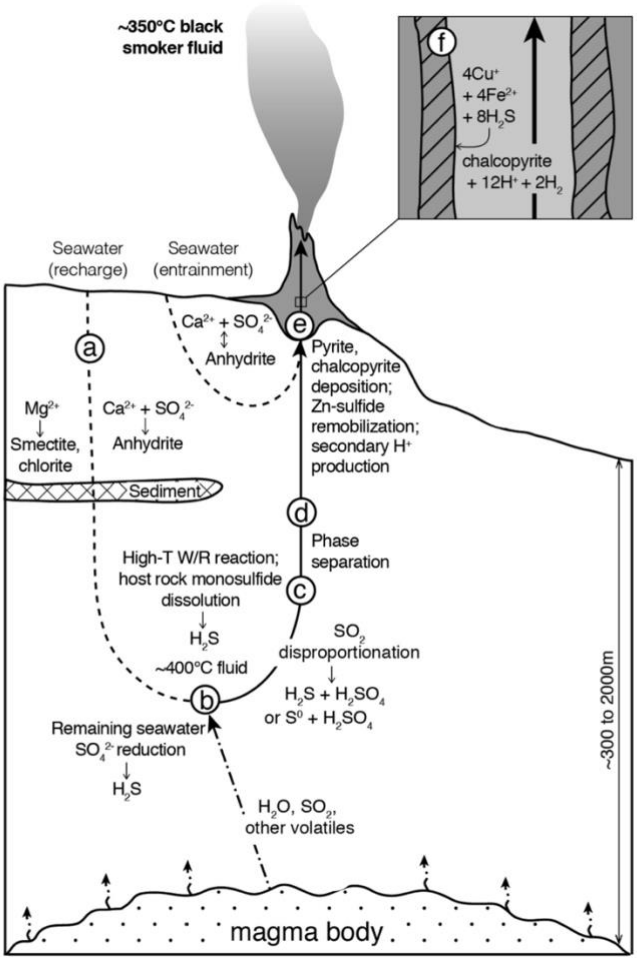

Figure 1.1: Modified from McDermott et al., (2015) showing the main processes than can affect sulfur in the cycle through a high temperature hydrothermal system.

The geochemical processes outlined above will leave an imprint on the ratios of multiple sulfur isotopes of fluids and minerals related to the vent system (Peters et al., 2010). Multiple sulfur isotopes have therefore been used to study the sulfur cycle at active seafloor hydrothermal systems related to fast and slow spreading ridges and back-arc spreading centers (Ono et al., 2007, McDermott et al., 2015, Peters et al., 2010) However the multiple sulfur isotope tool has not yet been applied to high temperature systems at ultra-slow spreading ridges.

This thesis is the first to investigate the variations in multiple sulfur isotope ratios in active high temperature chimneys along the ultra-slow spreading Arctic Mid Ocean Ridges. The study locations are the four different vent fields Seven Sisters, Soria Moria, Fåvne and Loki's Castle. This thesis focuses on multiple sulfur isotopes in sulfides and fluid samples from active high temperature chimneys. The data is interpreted using the anhydrite buffer model and the two-component mixing model following Ono et al. (2007), in order to distinguish between the different reactions in the circulation system that have affected the isotopic composition of sulfides. The results are compared with previous multiple sulfur isotope studies from different high temperature chimneys related to fast, slow and back-arc spreading systems. Through this, this thesis aims to explore how variations in the geological settings (magmatic input, sedimentary input, host rocks, fluid temperature, depth) of the vent fields are reflected in the sulfur isotope ratios, and increase our understanding of hydrothermal sulfur cycling along the Arctic Mid Ocean Ridges.

CHAPTER 2: THEORETICAL BACKGROUND

2.1 Sulfur Isotope geochemistry

Sulfur is the 14th most abundant element in the Earth's crust and is found in a large variety of redox states, from the reduced form of sulfide (S^{2-}) to the most oxidized form of sulfate (SO_4^{2-}) (Rickard, 2012). The element has 4 naturally occurring stable isotopes, of which ^{32}S is the most abundant (95%), followed by ^{34}S (4,22%), ^{33}S (0,76%) and ^{36}S (0,014%) (Sharp, 2017). Variations in the ratios of stable sulfur isotopes are typically expressed using the delta-notation, where measured isotope ratios are normalized against the isotopic composition of the Vienna Canyon Diablo Troilite (VCDT) following Seal (2006):

$$\delta^{34}S = \left(\frac{\left(\frac{^{34}S}{^{32}S}\right)_{sample} - \left(\frac{^{34}S}{^{32}S}\right)_{VCDT}}{\left(\frac{^{34}S}{^{32}S}\right)_{VCDT}} \right) \cdot 1000 \qquad (2.1)$$

2.2 Fractionation of sulfur stable isotopes

The number of neutrons in the nucleus characterizes the sulfur stable isotopes, and their difference in mass causes them to behave slightly differently in chemical and physical processes (Sharp, 2017). This is called isotope fractionation (Hoefs, 2018), and results from the isotopes forming bonds with different bond strengths to other elements. This causes a change in ratios of the stable isotopes when coexisting phases go through physical or chemical reactions (Sharp, 2017).

Equilibrium isotope fractionation happens when isotopes fractionate because of a reversable chemical or physical reaction (Seal, 2006). The amount of fractionation between two compounds that are in equilibrium is quantified by the equilibrium fractionation factor, which is temperature dependent (Seal, 2006). The degree of isotope exchange in an equilibrium-controlled process is dependent on the degree of chemical equilibrium between the species, because the isotopic equilibrium fractionation factors are the same as the equilibrium constants for the reactions (Barnes, 1997). An example of this is the redox reaction between sulfate and sulfide from Barnes (1997):

$$^{32}SO_4^{2-} + H_2^{34}S \leftrightarrow H_2^{32}S + {}^{34}SO_4^{2-} \quad (2.2)$$

Isotopes will exchange to reach equilibrium, and the exchange has a faster rate at higher temperatures (Barnes, 1997). When sulfate and sulfide are in chemical equilibrium, there will be a complete isotope exchange and the sulfur isotopic composition of the sulfur and sulfide will agree with the equilibrium fractionation factors between them (Barnes, 1997). When two coexisting sulfur species are in equilibrium, the heavy isotope (^{34}S) will be enriched in the more oxidized sulfur species, so that $\delta^{34}S\ SO_4$ (sulfate) > $\delta^{34}S\ \ H_2S$ (sulfide) (Seal, 2006). This is reflected in the geological record by sulfate minerals typically having higher $\delta^{34}S$ values compared to sulfide minerals (Seal, 2006).

Kinetic isotope fractionation happens when the rate of the forward reaction is much faster than that of the backwards reaction, therefore making it a unidirectional reaction (Barnes, 1997). Examples are the physical process of evaporation and the chemical process of bacterial sulfate reduction to H_2S. This will cause enrichment of lighter isotopes in the product of the process as they have weaker bonds that break faster resulting in a faster reaction rate (Barnes, 1997). This is seen in bacterial sulfate reduction, where the SO_4^{2-} molecules containing the lighter ^{32}S isotope will react faster than the molecules containing the heavier ^{34}S isotope and the product H_2S will therefore be enriched in ^{32}S relative to the initial isotopic composition of the sulfate (Barnes, 1997).

Isotopic variations can also be caused by mixing of ratios between compounds (Seal, 2006). This can be described by a mass balance equation from (Seal, 2006):

$$\delta_{\text{mixture}} = f_A\delta_A + f_B\delta_B \quad (2.3)$$

Where f is mole fraction and δ is isotopic ratio. The δ_{mixture} will then be the result of the mole fraction of compound A and B and the isotopic ratio of A and B (Seal, 2006).

Mass dependent fractionation and Δ-values

Mass-dependent fractionation refers to processes that produce systematic and predictable correlations based on the masses of the different stable sulfur isotopes, and are the most common type of fractionation happening in geochemical systems (Hulston and Thode, 1965, Seal, 2006). Mass dependent fractionation processes produce isotopic compositions that fall on the mass dependent fractionation line, the slope of the line corresponds to the relative mass difference between two ratios (Seal 2006). On a plot of $\delta^{33}S$ vs $\delta^{34}S$ (Figure 2.1) that represents

the average of all terrestrial mass dependent fractionation processes, the mass dependent fractionation line has a slope of 0,515. For $\delta^{36}S$ vs. $\delta^{34}S$, the slope will be 1,9 (Farquhar and Wing, 2003, Seal, 2006), as predicted from mass differences between the isotopes Since the mass dependent fractionation lines are defined by the slopes above, individual mass-dependent processes that follow slightly different mass-relations will produce isotopic compositions that can deviate by a few percent from this line (Farquhar and Wing, 2003). The capital delta notation $\Delta^{33}S$ and $\Delta^{36}S$ are used to express deviations from the mass-dependent fractionation line (Ono et al., 2007, Hulston and Thode, 1965). $\Delta^{33}S$ and $\Delta^{36}S$ can be calculated linearly by equations 2.4 and 2.5 (Ono et al., 2007).

$$\Delta^{33}S = \delta^{33}S - 0{,}515 \cdot \delta^{34}S \quad (2.4)$$

$$\Delta^{36}S = \delta^{36}S - 1{,}9 \cdot \delta^{34}S \quad (2.5)$$

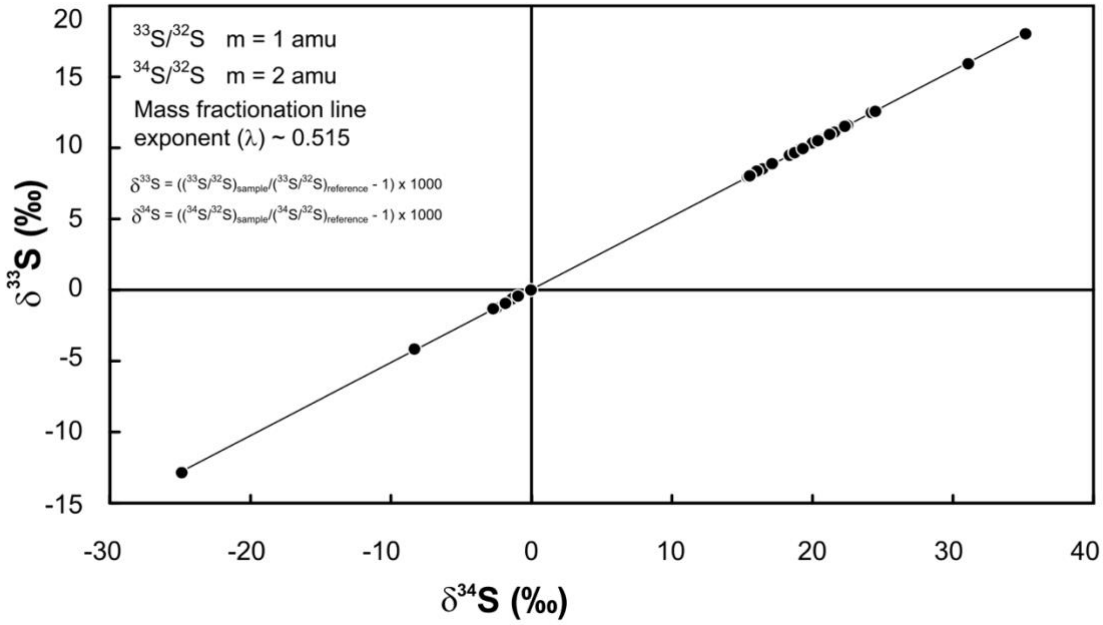

Figure 2.1 from Farquhar and Wing (2003).Plot of $\delta^{33}S$ vs. $\delta^{34}S$ for terrestrial sulfide and sulfate with the fractionation line where the exponent is 0,515. The fractionation line reflects all the mass-dependent fractionation processes that have been fractionating stable sulfur isotopes on earth for 2 billion years (after great oxidation event) (Farquhar and Wing, 2003)

Mass dependent fractionation of sulfur isotopes will generate close to zero values for $\Delta^{33}S$ and $\Delta^{36}S$, but there will be small variations depending on the individual process (Farquhar and Wing, 2003). Equilibrium isotopic exchange typically have a slope of about 0,515, while kinetic processes tend to have a slope closer to 0,5 (Farquhar and Wing, 2003). For example, sulfate

reduction by bacteria *Archaeglobus fulgidus* follows a mass dependent fractionation line with a slope of 0,5117 (Figure 2.2) (Farquhar and Wing, 2003). This means that variations in $\Delta^{33}S$ values can be a helpful tool to distinguish between different mass-dependent processes (Farquhar and Wing, 2003), including high-temperature reaction happening in seafloor hydrothermal systems.

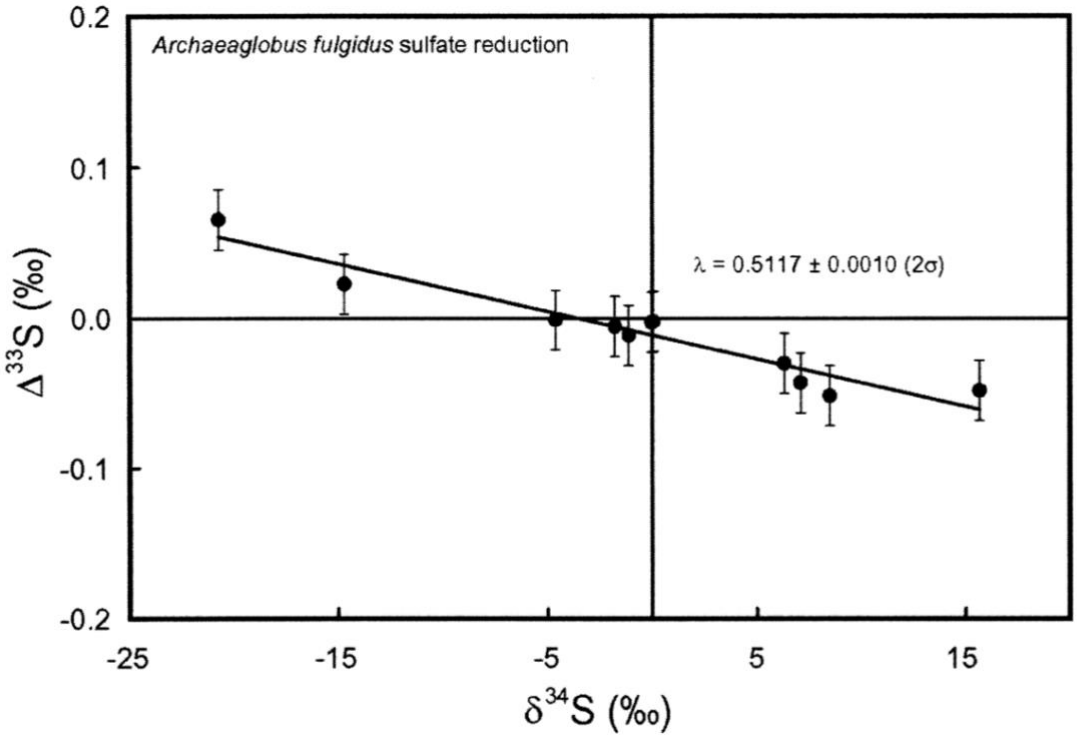

Figure 2.2 from Farquhar and Wing (2003). $\Delta^{33}S$ vs $\delta^{34}S$ for sulfate reducing bacteria. The horizontal line represents the mass-dependent terrestrial fractionation line with slope exponent of 0,515. The sulfate reducing bacteria fractionate the sulfur stable isotopes mass-dependently, but with a smaller slope exponent of 0,5117.

Sulfur isotopes in high temperature hydrothermal systems

The main geochemical processes affecting sulfur in high temperature hydrothermal systems are outlined in the introduction. The table below summarizes the expected isotope effects in sulfides and hydrothermal fluids related to the vent system.

Table 2.1: Shows the main geochemical processes that leave an imprint on the ratios of multiple sulfur isotopes of fluids and minerals related to the vent system. The main effect they have on the isotopic composition of sulfides in fluids and minerals are outlined in the right column (Ohmoto et al., 1983, Shanks et al., 1981, Herzig et al., 1998, McDermott et al., 2015, Ono et al., 2007, Peters et al., 2010). The effect on $\Delta^{36}S$ values is not included since it is typically not used because the measured precision is not sufficient to distinguish between different processes.

Process	**Effect on multiple sulfur isotopes in sulfides**
Anhydrite precipitation	No fractionation
Thermochemical sulfate reduction	Sulfide with a sulfur isotope composition that is the same as seawater (positive $\delta^{34}S$ and close to zero $\Delta^{33}S$ values)
Interaction with sediments (leaching of biogenic sulfides produced from microbial sulfate reduction)	Sulfides with isotopic composition that is the same as biogenic sulfides (typically, highly negative $\delta^{34}S$ values and highly positive $\Delta^{33}S$ values)
Leaching of sulfide minerals in the host rock (for mid ocean ridges this will typically be basalt)	Sulfides with an isotopic composition that is the same as basalt (close to zero $\delta^{34}S$ and $\Delta^{33}S$ values)
SO_2 disproportionation	Fractionation happens producing sulfides with negative $\delta^{34}S$ values and non-zero $\Delta^{33}S$ values
Isotopic exchange between sulfate and sulfide (equilibration between sulfate from anhydrite and sulfide in fluids)	Fractionation happens and values of $\delta^{34}S$ and $\Delta^{33}S$ are dependent on temperature (typically, positive $\delta^{34}S$ and $\Delta^{33}S$ values)

CHAPTER 3: GEOLOGICAL BACKGROUND

3.1 The Arctic Mid Ocean Ridges

The mid ocean ridges north of the Arctic circle at 66 ºN extends through the Norwegian-Greenland Sea and is called the Arctic Mid Ocean Ridges (AMOR). It is a 4000 km long ultra-slow ridge system that starts on the northern shelf of Iceland and ends on the Siberian Shelf in the Laptev Sea (Pedersen et al., 2010b). AMOR comprises six segments: The Kolbeinsey ridge, The Mohns ridge, The Knipovich ridge, The Molloy Ridge, the Lena Trough, and the Gakkel Ridge. Three distinct fracture zones intersect AMOR: the West Jan Mayen fracture zone at 71 ºN, the Spitzbergen and Molloy fracture zone at 79 ºN. AMOR changes orientation at 74 ºN and 83 ºN. This makes bends in the ridge, separating the Mohns Ridge from the Knipovich Ridge and the Lena Trough from the Gakkel Ridge (Pedersen et al., 2010b). The spreading rate is faster furthest south, where the Kolbeinsey Ridge has a spreading rate of about 20 mm/year, than furthest north at the Gakkel Ridge, where the spreading rate is only 6 mm/year. There is a gradual decrease in the spreading rate northward because the southern part is influenced by the Islandic hotspot. Therefore, the southern parts have a robust magma supply, higher spreading rates, and thicker crust compared to the northern parts furthest away from the hotspot. Here, the ridges have a limited magma supply resulting in thinner crust and the ridges being on deeper water depths. (Pedersen et al., 2010b).

Hydrothermal activity is abundant at the AMOR (Figure 3.1). Both extinct and active vent fields have been found. They are influenced by various geological settings occurring along the ridges as the segments have varying crust thickness and water depths (Pedersen et al., 2010b). Also, segments with a more robust magma supply typically have basalt-hosted vent fields, and the more magmatically starved vents fields could be hosted in exposed ultramafic mantle rocks. Most of the vent fields occurring along the AMOR are associated with axial volcanic ridges with a focused magma supply and a deep, well-developed rift valley. Causing active detachment faults, which could be the main mechanism behind the abundant hydrothermal activity occurring along the ridges (Pedersen et al., 2010b).

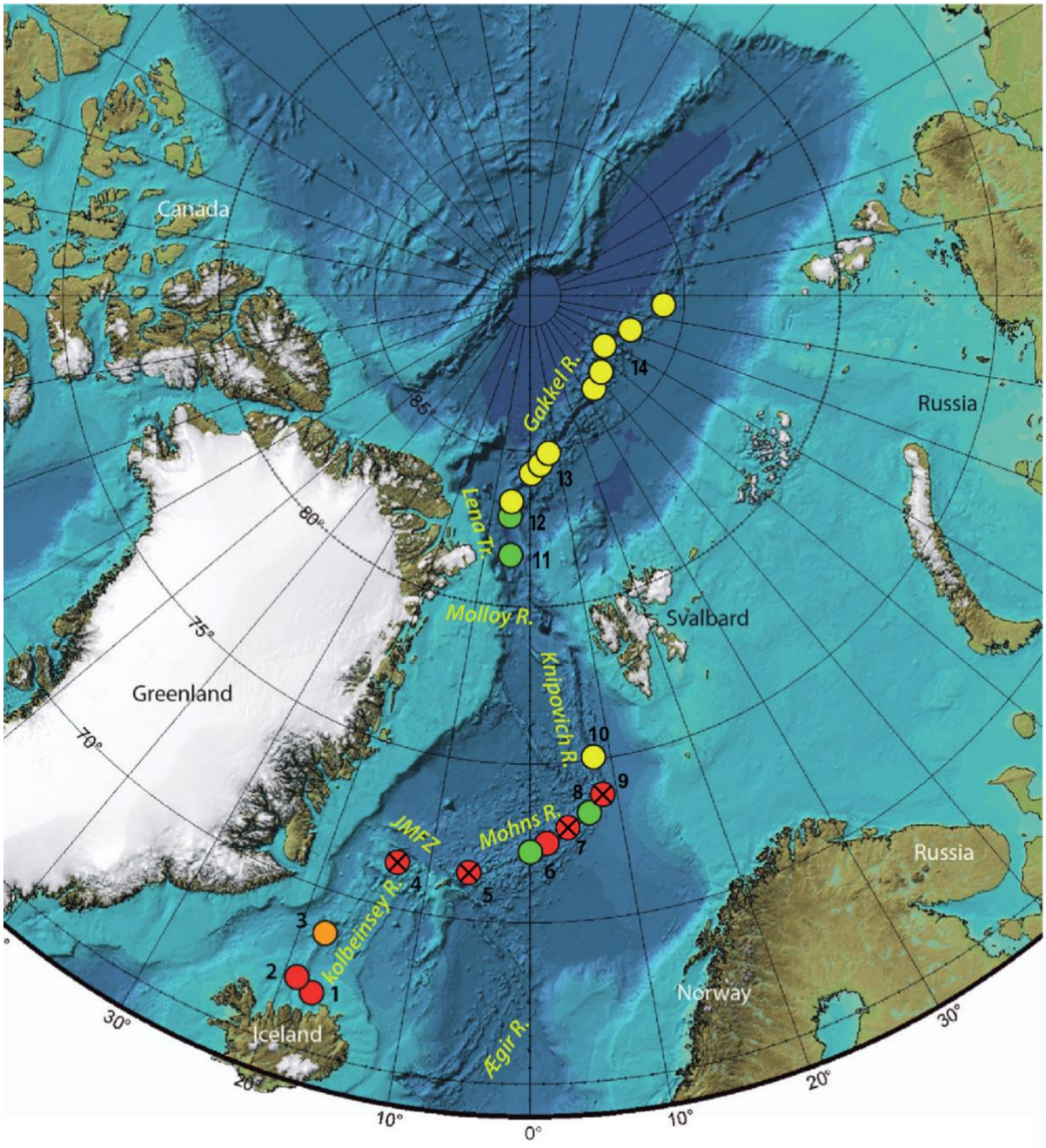

Figure 3.1: Map of AMOR showing hydrothermal related geologies where red circles are active vent fields, orange circles are extinct vent fields, green circles are sulfide deposits and yellow circles are hydrothermal plumes. Red circles marked with X are active vent fields in focus for this study. 1) Grimsey, 2) Kolbeinsey, 3) Squid Forest, 4) Seven Sisters, 5) Jan Mayen vent fields, 6) Copper Hill, Ægirs Kilde, 7) Fåvne, 8), Mohns Treasure, 9) Loki's Castle, 10) hydrothermal plume, 11) sulfide deposit, 12) sulfide deposit and hot waters, 13) and 14) hydrothermal plumes (taken from Pedersen and Bjerkgård (2016) and modified from Boonnawa et al. (in prep)).

This project will be investigating hydrothermal systems located on the Kolbeinsey ridge and the Mohns ridge. Therefore, these two ridge segments and vent fields will be discussed further below.

3.2 Kolbeinsey Ridge

The ridge segment closest to Iceland on the southern end of AMOR is the Kolbeinsey ridge. The Icelandic hotspot strongly influences this ridge segment due to its near Iceland placement (Pedersen et al., 2010b). The Kolbeinsey ridge has an orthogonal spreading, and the middle has a crustal thickness of 9 km, making it have the thickest crust out of the six segments. The crust thickness affects the water depth, which is on average 1000 m deep, making it the shallowest segment out of the six (Pedersen et al., 2010b). There is orthogonal spreading with a full spreading rate of 20 mm/year. Although it has ultra-slow spreading, the influence of the Icelandic hotspot affects this segment to have a morphology similar to fast-spreading ridges where the neovolcanic zone here occurs in a small rift valley about 1000 m deep. The Kolbeinsey ridge is divided into three segments, south, central, and north, which are divided by non-transform offsets (Marques et al., 2020). The Northern Kolbeinsey Ridge (NKR) hosts the active Seven Sisters vent field. The Northern Kolbeinsey ridge has high magmatic activity that is volatile-rich and multiple episodes of explosive volcanism has deposited volcaniclastics here (Marques et al., 2020).

3.2 Seven Sisters

Geological setting

The Seven Sisters vent field is located on the NKR on the eastern side of the rift valley. It was discovered in 2013 by UiB, located on a flat-top volcano that is part of a chain of flat-top volcanoes (Figure 3.2a). These flat-top volcanoes occur on a shallow area related to the NKR called the Eggvin bank (Marques et al., 2020). The Eggvin bank span over the axial zone of the NKR in between the West Jan Mayen Fracture Zone (northern margin) and a small offset on the Kolbeinsey Ridge (southern margin) and has a crustal thickness of up to 13 km (Tan et al., 2017). It has numerous submarine volcanic peaks, and the shallowest part of the Eggvin bank is defined by a large volcanic edifice that is located on less than 30 m water depth, which is 20 km north of the Seven Sisters vent field, where the water depth is 130 m (Yeo et al., 2016, Marques et al., 2020). North of the summit caldera, there are large recent lava flows filling the rift valley. (Marques et al., 2020). The Eggvin bank's crust has a mafic composition, and the flat-topped volcano hosting the seven sisters vent field is dominated by mafic volcaniclastic

lithologies (Tan et al., 2017, Marques et al., 2020). Not far from the area with hydrothermal mounds, there are fractures filled with dark volcaniclastic material, indicating that there has been recent explosive volcanic activity in the area (Marques et al., 2020). There is extensive vulcanism in the area where the Seven Sisters vent field is located and it is related to the Eggvin bank and define the vent field to be a magmatic hydrothermal system affected by degassing of volatiles in magma (Marques et al., 2020).

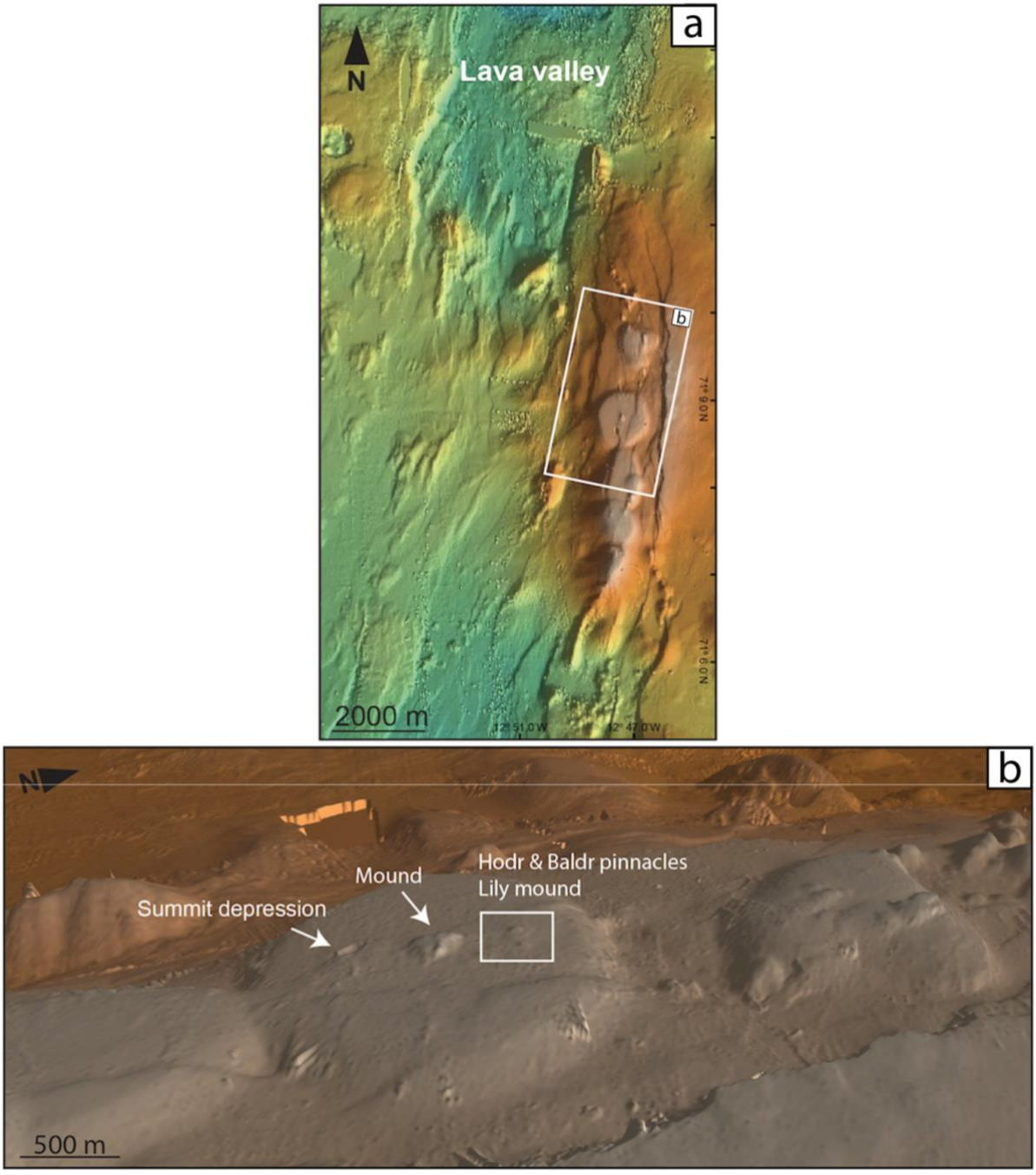

Figure 3.2: **(a)** high-resolution bathymetry of the NKR where the chain of flat-top volcanoes are located at the eastern margin of the rift valley (from Marques et al., 2020). **(b)** high-resolution bathymetry of the flat-top volcano

hosting the Seven sisters vent field showing a summit depression, a mound, and the venting area with Lily mound, Hodr and Baldr pinnacles (modified from Marques et al. (2020).

Vent structures and fluids

The seven sisters vent field has widespread diffuse venting, but the hydrothermal activity can be divided into three distinct areas where the venting emits from different geological morphologies. One area with diffuse venting related to fractures in exposed volcaniclastic crust in a summit depression, bacterial mats are found here. Another area with venting from a ca. 100 m wide central mound. An area with focused venting from clusters of larger rounded mound structures where some have partially collapsed, which may be due to anhydrite dissolution, and smaller mound structures about 5 m wide (Figure 3.2b). This area also contains smoking craters and pinnacle-like structures (Marques et al., 2020).

In this thesis, one of the venting smaller mounds called Lily mound, and one of the pinnacles called Hodr has been sampled. Marques et al. (2020) studied the Seven Sisters vent field and found that Lily mound has clear vent fluids, which are phase separating, and a measured temperature of 199 ºC. They also found Hodr in the same area with clear venting fluids and measured temperatures up to 181 ºC. Hodr does not have a well-defined venting area and consist of mainly barite, silica, and pyrite (Marques et al., 2020) Lily mound is also mainly made up of barite, and both vent structures (Lily and Hodr) contain only small amounts of sulfides (less than 5 wt.%). The main sulfate making up the pinnacles and mounds in the area is barite, and anhydrite is less common. Anhydrite is present mainly in the volcaniclastic deposits (Marques et al., 2020). Barites from the top of Lily mound have $\delta^{34}S$ values of 22,2‰ and 20,1‰ which is lower and higher than seawater sulfate ($\delta^{34}S$ = 21,5‰). Barites from Hodr have $\delta^{34}S$ values of 24‰, which is higher than seawater sulfate (Marques et al., 2020).

Based on vent fluid geochemistry and stable isotope data (C, S) the fluids at Hodr pinnacle and Lily mound have experienced limited mixing with seawater and are mostly derived from a basalt source. High CO_2 concentration indicate input of carbon from degassing magma. Also, low CH_4 and H_2 concentrations suggests that the Seven Sisters vent field is not influenced by sediments Marques et al. (2020).

3.3 Mohns Ridge

The 550 km long ridge segment that extends from the Jan Mayen fracture zone (JMFZ) in the south at 71 ºN to the bend at 74 ºN in the north is called the Mohns Ridge. Here the spreading is oblique and has a full spreading rate of 15 mm/year, which s is slower than at the Kolbeinsey

Ridge. Also, the crust thickness is on average thinner, and the ridge occurs at deeper water depths than the Kolbeinsey Ridge. Though in the southern part, the Mohns Ridge has similarities with the Kolbeinsey Ridge as the Jan Mayen hotspot influences it and therefore has a higher magma supply than further north (Pedersen et al., 2010b). The further north away from the Jan Mayen hotspot, there is lower magma supply, and the segments have the characteristics of an ultra-slow spreading ridge. It has a more well-developed rift valley that is up to 3500 m deep, bounded by over 1000 m high fault walls. In some areas, there are core complexes present suggesting amagmatic accretion processes (Pedersen et al., 2010b, LaFemina, 2015).

3.4 Jan Mayen vent fields

Geological setting

The Jan Mayen vent fields refer to an active hydrothermal area containing three vent fields The Troll wall, Soria Moria, and Perle & Bruise (Pedersen and Bjerkgård, 2016). They are basalt hosted and located along the southern segment of the Mohns ridge on a volcanic plateau close to the JMFZ (Figure 3.3a) (Pedersen et al., 2010b, Johannessen et al., 2017, Stensland et al., 2019). Soria Moria and The Troll Wall vent fields were discovered in 2005 by Pedersen et al. (2005), and later in 2013, The Perle & Bruise vent field was discovered by UiB (Pedersen and Bjerkgård, 2016). The Jan Mayen Vent fields are a part of the AMOR system that is influenced by both the Icelandic and the Jan Mayen hotspot. Thus, it has anomalously high magmatic activity, thick crust, and shallow water depths (Johannessen et al., 2017). The cause for the crust to be an anomalous 10 km thick here is interpreted as a result of the Jan Mayen hotspot being fueled by a magmatic anomaly (Stensland et al., 2019). The spreading along this part of Mohnsridge is orthogonal and differs from the oblique spreading along the rest of the ridge (Pedersen et al., 2010b).

The Soria Moria vent field is located about 700 m water depth on top of a volcanic ridge which is a part of a young volcanic field on top of an older lava field (Figure 3.3b). This older lava field plausibly had fissure eruptions followed by massive lava outflow as it consists of large lava flows and lava tubes (Pedersen et al., 2010b). There are two venting areas with a couple of hundred meters separating them. One of them has venting that could be linked to a small fault basin, and the other has an unknown structural control (Pedersen et al., 2010b). Two sampled chimneys are found here Lilleput and Soria Moria (Pedersen and Baumberger, 2011).

The Troll wall vent field is located about 5 km north of the Soria Moria vent field (Pedersen and Bjerkgård, 2016). It occurs at 550-600 m depth at the bottom of a 100 m high footwall of a rift bounding normal fault (Figure 3.3b) (Johannessen et al., 2017, Stensland et al., 2019).

The later discovered Perle & Bruise vent field is located 2 km east of the Troll at the flank of a central volcano undergoing rifting (Figure 3.3c) (Pedersen and Bjerkgård, 2016). The venting occurs at 580 m water depth along rift-parallel faults (Stensland et al., 2019, Pedersen and Bjerkgård, 2016).

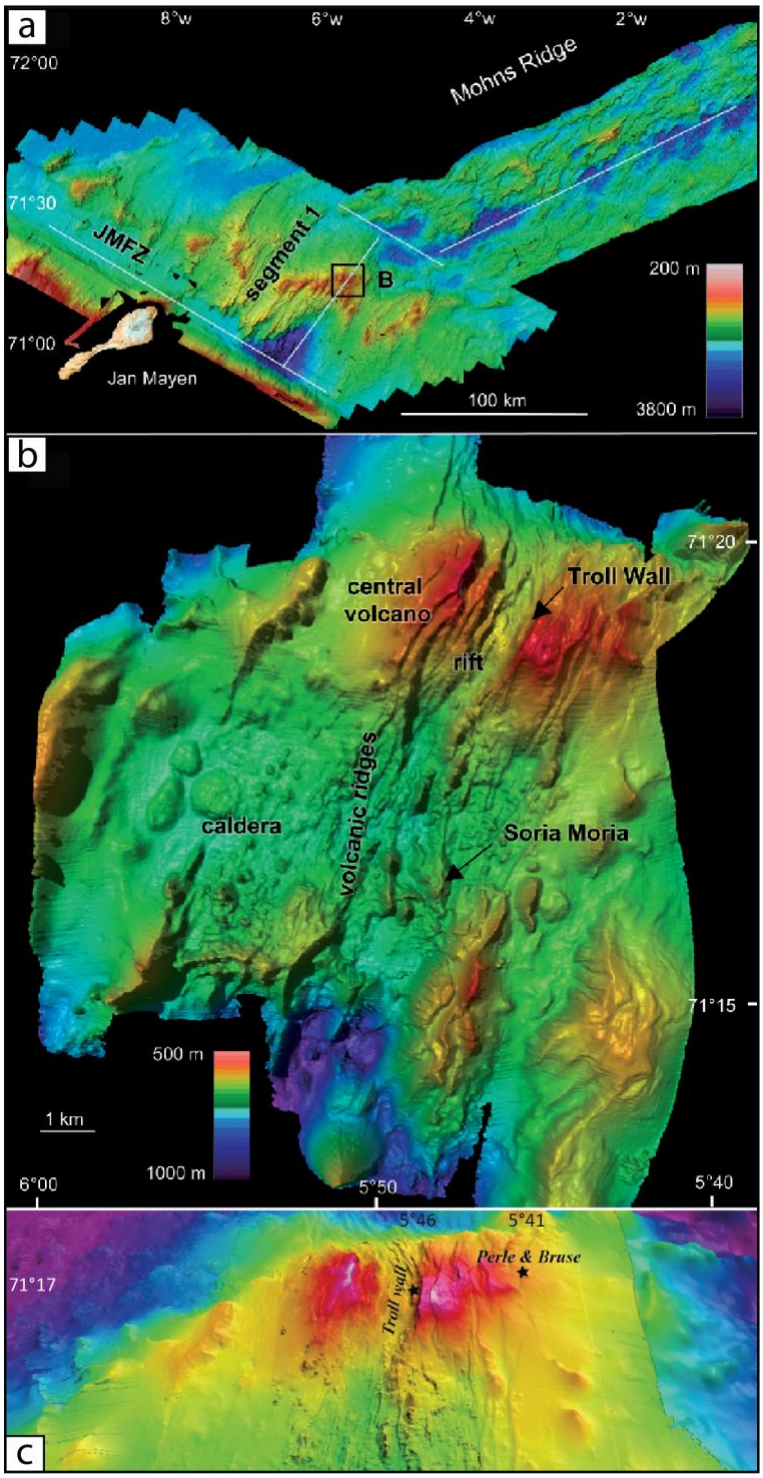

Figure 3.3: (a) Bathymetric map of the southern end of the Mohns Ridge and part of the Jan Mayen fracture zone showing with a black square where the Jan Mayen vent fields are located (from Pedersen et al. (2010b)). **(b)** Bathymetric map of the Jan Mayen vent fields showing the volcanic ridge hosting the Soria Moria vent field and the central volcano at the shallowest part of the segment with a rift hosting the Troll wall vent field (from Pedersen and Bjerkgård (2016)). **(c)** Bathymetric map showing the location of the Perle & Bruise vent field on the central volcano (from Stensland et al. (2019)).

Vent structures and fluids

The Soria Moria vent field has high-temperature hydrothermal fluids, approximately 270 ºC white smoker fluids from numerous 8-9 m tall sulfide chimneys where sphalerite is the main sulfide phase (Pedersen et al., 2010b, Pedersen and Bjerkgård, 2016). In contrast, low-temperature clear hydrothermal fluids also escape from irregular constructions consisting of small amounts of sulfides and mostly barite and silica (Pedersen et al., 2010b).

Like the Soria Moria field, the high-temperature vents at the Troll wall vent field are white smokers emitting about 270 ºC fluids. They are mainly composed of anhydrite, barite, pyrite, and sphalerite (Johannessen et al., 2017). 500 m west from this active high-temperature area with white smoker vents, there are extinct silica-dominated mounds and diffuse low-temperature fluids emitting along the central rift floor from ridge-parallel faults and fissures. Here there are volumes of silicious Fe-deposits on top of hyaloclastite and basaltic debris (Johannessen et al., 2017).

The later discovered Perle & Bruise vent field has two distinct hydrothermal mounds venting about 200 ºC fluids (Stensland et al., 2019).

All three vent fields have vent fluid temperatures and compositions that are comparable (Pedersen and Bjerkgård, 2016, Pedersen et al., 2010b, Stensland et al., 2019). The magmatic anomaly affects the hydrothermal fluids from the Jan Mayen vent fields to be enriched in degassed CO_2 and high flux of ^3He (Stensland et al., 2019).

3.5 Fåvne

Geological setting

Fåvne is not a well-studied hydrothermal field as it has only recently been sampled. It is located at a 3000 m water depth northeast of the central part of the Mohn Ridge (Boonnawa et al., in prep). This is 10 km west of an axial volcanic ridge and close to the termination of a detachment fault plane (Figure 3.4) (Boonnawa et al., in prep). Only basaltic rocks have been sampled surrounding the hydrothermal vents (Brekke et al., 2021) with minimal sediment cover, yet vent fluids there have chemical characteristics indicating possible ultramafic influence via the detachment fault, with minimal influence of sedimants (Boonnawa et al., in prep).

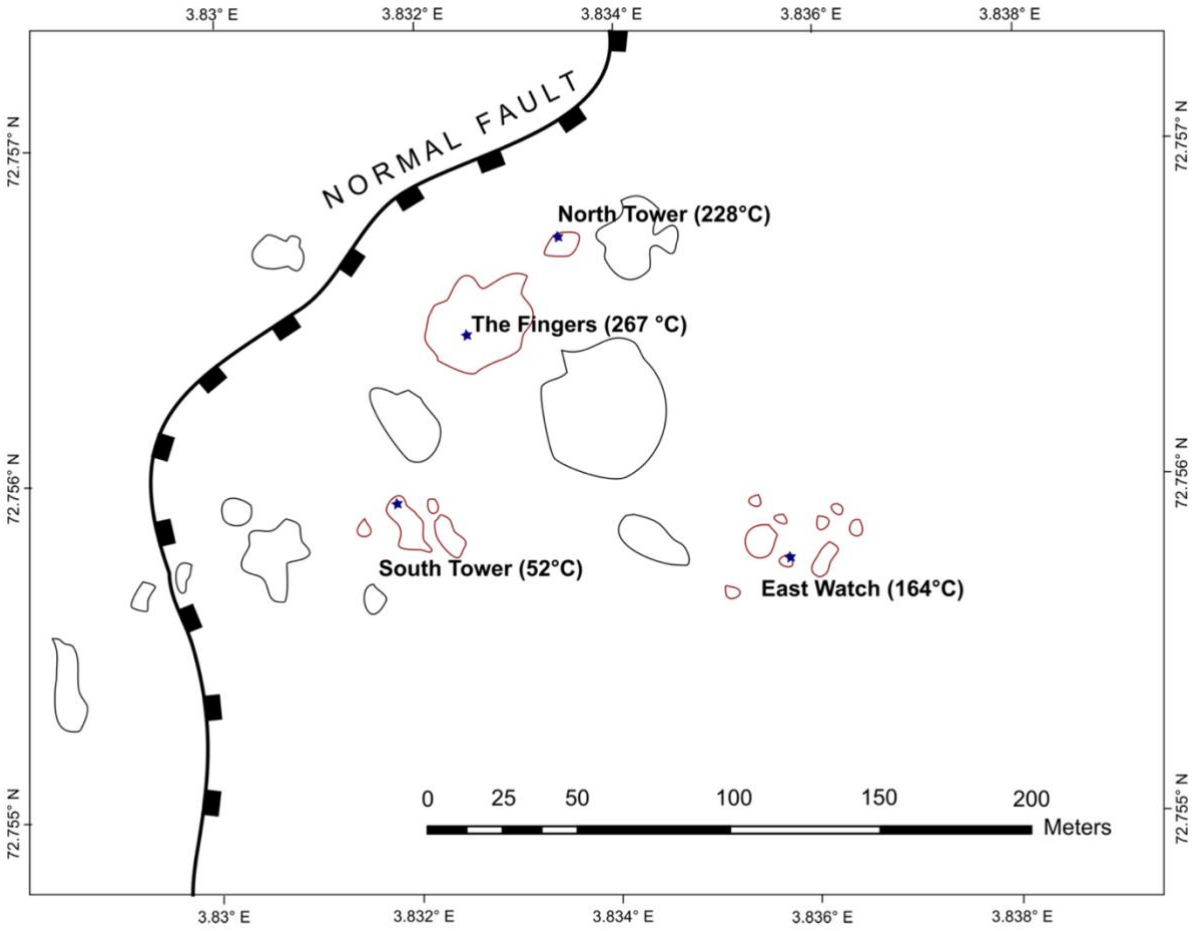

Figure 3.4: Simplified map of the Fåvne vent field taken from Boonnawa et al. (in prep) showing the locations of four of the active vents (red lines) and the base of the detachment fault. The stars represent orifices on the active mounds that hydrothermal fluids were collected and studied by. The black lines represent topographic highs or hydrothermal mounds.

Vent structures and fluids

The Fåvne vent field contains both active vent sites with varying activity of the vents and inactive vent sites (Boonnawa et al., in prep). In the Boonnawa et al. (in prep) sampling of the Fåvne vent field, active and vigorously venting constructions were the focus of this study. Boonnawa et al. (in prep) sampled four chimney complexes located 50-150 m apart, The Fingers, East Watch, North Tower, and South Tower, with a gray-black color where highly pours causing fluids to escape through chimney walls. Sulfide minerals appear to be the primary chimney wall material. Three of the four vents, The Fingers, East Watch, and North Tower, were measured as high-temperature chimneys, emitting acidic fluids with measured max temperatures of 267 ºC, 164 ºC, and 228 ºC, respectively. Dissimilarly, fluids emitting from South tower have low temperatures (52 ºC; Boonnawa et al. (in prep))

3.6 Loki's Castle

Geological setting

Loki's castle vent field was discovered in 2008 at 73º 30' N and 8º E on the northern end of the Mohns Ridge on the sharp bend where it transitions into the Knipovich ridge (Pedersen et al., 2010a, Pedersen et al., 2010b). It is located on a 30 km long axial volcanic ridge (AVR), on the northwestern margin of a rift, related to a tectonic lineament, along the crest of the ridge (Figure 3.5a). Loki's castle is a basalt-hosted system located on a young volcanic field containing young pillow flows on top of older flows (Pedersen et al., 2010b). Loki's Castle is 5 km away from the distal parts of the Bear Island sediment fan. Hence its sediments cover the eastern flank of the axial volcanic ridge and have spilled into the rift valley. Tough the basalt flows underlying Loki's Castle only have a thin layer of sediment covering them (Pedersen et al., 2010b, Baumberger et al., 2016b). On the other hand, the western flank of the axial volcanic ridge has dome-shaped core complexes (Baumberger et al., 2016b).

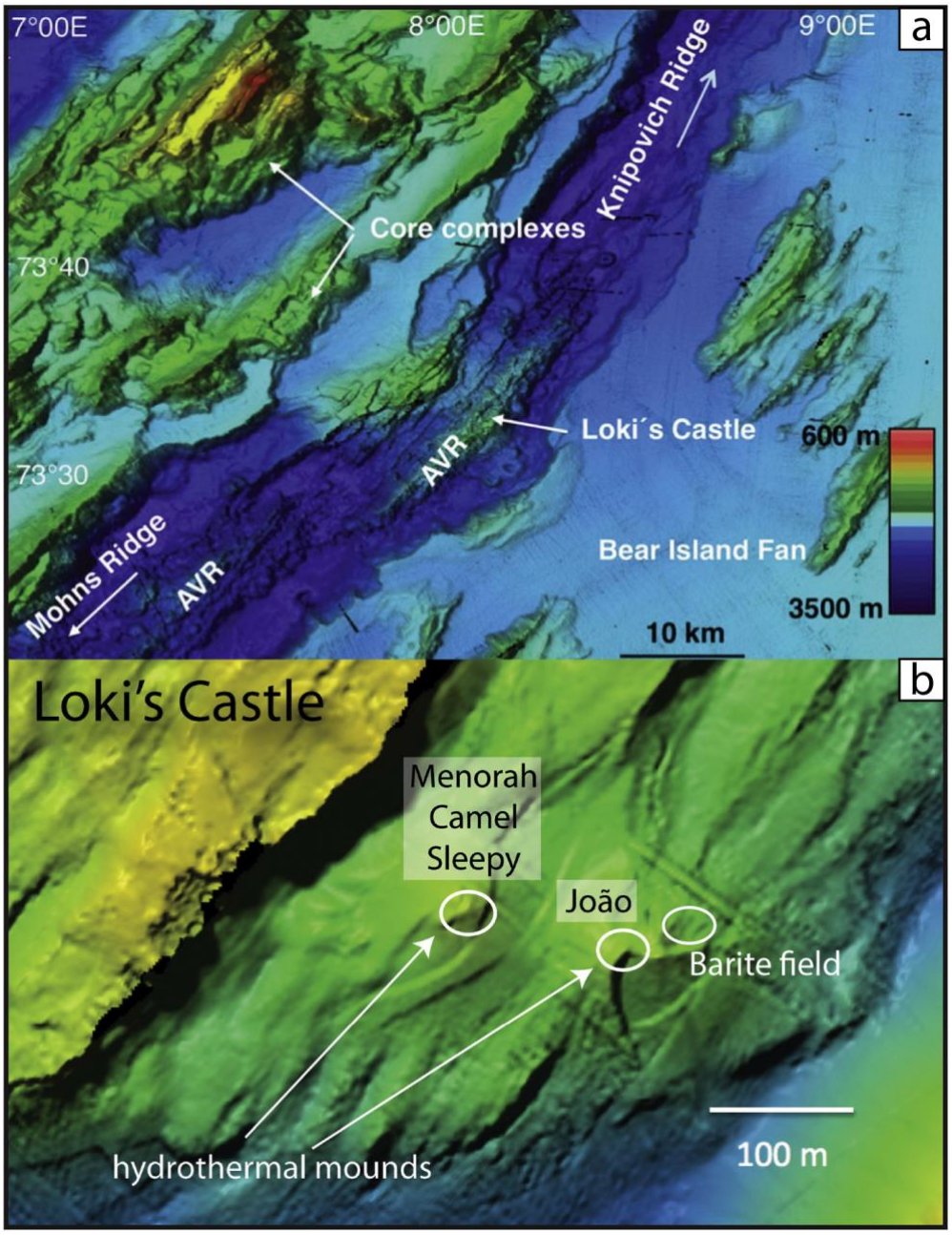

Figure 3.5: (a) Bathymetric map of the bend where the Mohns Ridge transitions into the Knipovich Ridge. Showing the axial volcanic ridge hosting Loki's Castle, Bare Island fan sediments covering the eastern flank of the ridge and core complexes on the western flank where lower crust and mantle lithologies are exposed by normal faults (modified from Pedersen et al. (2010b)). **(b)** Bathymetric map of the Loki's Castle vent field showing the two sulfide mounds and where the black smoker chimneys Menorah, Camel, Sleepy and, Joao are located and where the low temperature barite field is located (modified from Eickmann et al. (2020)).

Vent structures and fluids

Loki's Castle consists of four black smokers, Joao, Menorah, Camel, and Sleepy, which vents high-temperature fluids with a measured max temperature of 317ºC (Baumberger et al., 2016a). They are located at 2400 m water depth on top of two 20-30 m high and 150-200 m wide sulfide mounds about 150 m apart. Menorah, Camel, and Sleepy are situated on the western mound.

Joao is situated on the eastern, close to an area with low temperature venting barite chimneys (Figure 3.5b) (Baumberger et al., 2016a, Pedersen et al., 2010b, Baumberger et al., 2016b).

Based on fluid geochemistry and isotope data (B, Sr) the Loki's Castle vent fluids are not interacting with the core complexes on the western flank of the volcanic ridge which have brought lower crust and mantle lithologies to the surface, but they have interacted with sediments (Pedersen et al., 2010b, Baumberger et al., 2016a, Baumberger et al., 2016b). The AVR hosting Loki's Castle could be on top of a thick sediment sequence if it developed after the Bear Island Fan sediments fell into the rift valley (Pedersen et al., 2010b). These sediments are plausibly interacting with hydrothermal fluids in Loki's Castle vent field, making it a sediment influenced system (Pedersen et al., 2010b, Baumberger et al., 2016a, Baumberger et al., 2016b).

The low temperature (about 20 ºC) venting barite chimneys called barite field are located on the northeastern flank of the eastern sulfide mound hosting Joao (Figure 3.5b) (Eickmann et al., 2020). The barite field consists of many small up to 1m tall chimneys with diffuse venting covered in microbial mats. The seafloor here is also covered in microbial mats, and there are Siboglinid tubeworms present (Eickmann et al., 2020). Eickmann et al. (2014) have identified microbial sulfate reduction to be a contributing process to the sulfur isotope values of the barite chimneys. The $\delta^{34}S$ values (+22,2 to +36,1‰) are higher and the $\Delta^{33}S$ (-0,031 to -0,159‰) values are lower than surrounding seawater sulfate ($\delta^{34}S$ =21,3 and $\Delta^{33}S$ =-0,040‰).

CHAPTER 4: METHODS

4.1 Sample collection and storage

Hydrothermal rock and fluid samples

The hydrothermal rock and fluid samples used in this project were collected on three different cruises in 2017, 2018, and 2019 to the Arctic Mid Ocean Ridges with R/V G.O. Sars.

The hydrothermal rock samples displayed in Table 4.1 were collected from actively venting hydrothermal chimneys using the robotic arm on the remotely operated vehicle (ROV) Ægir 6000. The samples were then cleaned aboard the ship with tap water and dried under a 1500W heater infrared lamp before they were stored in sealed bags filled with nitrogen gas and transported to the University of Bergen.

Table 4.1: All collected hydrothermal rock samples with their sample ID, the vent field and chimney they are from, coordinates, depth, temperature, and fluid pairs. The temperature measurements were done by Eoghan Reeves. The fluid pairs represent hydrothermal fluids sampled from the same chimney during the same cruise.

Sample ID	Metadata						
	Ventfield	Chimney	Latitude	Longitude	Depth(m)	Temperature (°C)	Fluid pairs
GS17-ROV17-R01	Loki's Castle	Joao	73°33.984'N	08°09.600'E	2311	306	ROV17-IGT2, IGT3
GS19-ROV20-R01	Loki's Castle	Joao	73°33.984'N	08°09.624'E	2302	306	
GS17-ROV19-R02	Loki's Castle	Sleepy	73°34.020'N	08°09.384'E	2314	299	ROV19-IGT2, IGT3
GS17-ROV19-R03	Loki's Castle	Menorah	73°34.008'N	08°09.390'E	2314	316	ROV19-IGT4, ROV21-IGT4
GS18-ROV22-R02	Loki's Castle	Camel	73°34.002'N	08°09.402'E	2310	316	
GS18-ROV08-R01	Seven Sisters	Lily	71°08.844'N	12°47.496'W	124	190	
GS18-ROV08-R05	Seven Sisters	Hodr	71°08.994'N	12°47.340'W	122	126	
GS18-ROV14-R01	Jan Mayen	Soria Moria	71°15.690'N	05°48.822'W	657	279	ROV14-IGT1, IGT2
GS18-ROV14-R03	Jan Mayen	Lilleput	71°15.582'N	05°48.864'W	719	255	ROV14-IGT3, IGT4
GS19-ROV16-R01	Fåvne	South Tower	72°45.354'N	03°49.878'E	3040	50	
GS19-ROV16-R02	Fåvne	North Tower	72°45.408'N	03°50.016'E	3026	265	ROV16-IGT1, IGT2

Hydrothermal fluid samples displayed in Table 4.2, were collected using ca. 160 ml isobaric gas-tight (IGT) titanium fluid samplers deployed from the ROV Ægir 6000. IGT samplers prevent the fluids from degassing and keep samples at seafloor pressure during transport to the surface (Seewald et al., 2002). They also provide real-time temperature measurement with thermocouple temperature sensors (Seewald et al., 2002). The fluid samples were removed from the IGT sampler and divided into aliquots on the ship. Using the method after Reeves et al. (2011), aliquots of known volume were sparged with Nitrogen gas and put into a 5 wt.% Silver nitrate ($AgNO_3$) solution to preserve H_2S. The result was silver sulfide (Ag_2S) precipitate, which was collected on filters.

Table 4.2: All collected hydrothermal fluid samples with their sample ID, the vent field and chimney they are from, coordinates, depth, temperature, and fluid pairs. The temperature measurements were done by Eoghan Reeves. The solid pairs represent hydrothermal rock sampled from the same chimney during the same cruise.

Sample ID	Metadata						
	Vent field	Chimney	Latitude	Longitude	Depth(m)	Temperature (°C)	Solid pairs
GS17-ROV17-IGT3	Loki´s Castle	Joao	73°33.984'N	08°09.600'E	2311	306	GS17-ROV17-R01
GS17-ROV17-IGT2	Loki´s Castle	Joao	73°33.984'N	08°09.600'E	2311	306	GS17-ROV17-R01
GS17-ROV19-IGT2	Loki´s Castle	Sleepy	73°34.020'N	08°09.384'E	2314	299	GS17-ROV19-R02
GS17-ROV19-IGT3	Loki´s Castle	Sleepy	73°34.020'N	08°09.384'E	2314	299	GS17-ROV19-R02
GS17-ROV19-IGT4+ROV21-IGT4	Loki´s Castle	Menorah	73°34.008'N	08°09.390'E	2314	316	GS17-ROV19-R03
GS18-ROV14-IGT1+IGT2	Jan Mayen	Soria Moria	71°15.690'N	05°48.822'W	657	279	GS18-ROV14-R01
GS18-ROV14-IGT3+IGT4	Jan Mayen	Lilleput	71°15.582'N	05°48.864'W	719	255	GS18-ROV14-R03
GS19-ROV16-IGT1+IGT2	Fåvne	North Tower	72°45.408'N	03°50.016'E	3026	265	GS19-ROV16-R02

4.2 Sample preparation

Hydrothermal fluid samples

Ag_2S was scraped from filters at the University of Bergene, placed in glass vials, and sent to the Stable Isotope Laboratory at Westfälische Wilhelms-Universität Münster.

Hydrothermal rock samples

The hydrothermal rock samples were ground at the University of Bergen using an Agate Mortar, making them powdered samples.

Stereo microscope (Leica Lupe)

The ground hydrothermal rock samples contained variable amounts of sulfide minerals which were hand-picked and identified to get more valuable data from the samples. On the Leica Lupe in the Raman laboratory at the University of Bergen, hand-picking was performed by spreading each sample out on Petri dishes. Then Sulfides were recognized by their submetallic- to metallic luster and picked out using tweezers and a magnet. After sulfides were separated from the non-sulfides in the individual samples, they were further separated into glass vials by their physical properties visible in the Leica Lupe. Their physical properties were together with the mineral description of sulfides by Johnson (2004), the primary tool used to distinguish them from each other and identify them. The main properties in focus were the mineral shape, color, and magnetism (Table 5.1). In addition to identification by physical properties, a Scanning Electron Microscope (SEM) was used to help identify sulfides and confirm observations made by the stereo microscope.

Scanning Electron Microscope

A Zeiss Supra 55VP Scanning Electron Microscope located at ELMI-lab at the University of Bergen was used to take pictures and examine the shape of the hand-picked sulfides and to perform chemical analyses. Sulfide grains were chosen from each hand-picked sample and

mounted using carbon adhesive tabs on aluminum mount stubs. After, they were coated with carbon using Agar Turbo Carbon Coater. Pictures were taken with a type II secondary electron signal (SE2), a 3,2-3,6 mm working distance, an acceleration voltage of 5,0kv, and an aperture diameter of 30 μm. Chemical analyses and pictures were performed with an SE2 signal, a working distance of 8,1-8,6 mm, an acceleration voltage of 15,0kv, and an aperture diameter of 60 μm. The element analyses were done using energy dispersive x-ray spectrometry (EDS), an in situ semi-quantitative analysis, and Thermo Fisher Scientific's software, Pathfinder. For the detected elements, an approximate order of abundance was made based on EDS peak intensities. The order of abundance is only an estimation as the EDS does not give a quantitative measurement.

Chromium Reduction

The bulk and hand-picked hydrothermal rock samples were converted into silver sulfide (Ag_2S) by the chromium reduction method at the University of Bergen to obtain high-precision multiple sulfur isotope data from sulfide minerals. The chromium reduction technique uses a boiling acidified chromium (II) chloride solution to extract sulfide from the samples as Acid Volatile Sulfur (AVS) and Chromium Reducible Sulfur (CRS) (Canfield et al., 1986, Fossing and Jørgensen, 1989). The method is specific for sulfide and does not dissolve sulfate (barite, anhydrite) and therefore ensures that sulfur isotope data is representative of the reduced sulfur in the sample.

The first step in performing the chromium reduction technique on the samples was to prepare the necessary reagents: 2M analytical grade HCl, 1M $CrCl_3$ in 0,5 analytical grade HCl (chromium solution), 6M analytical grade HCl, ultrapure water, 3 ml 0,3 M $AgNO_3$ + 2 ml 1,5 M double-distilled HNO_3 + 10 ml ultrapure water ($AgNO_3$ trap).

The second step involved producing acidified chromium (II) chloride solution, which was done in a reaction flask (Figure 4.1). The reaction flask was first filled with zinc pellets before 2M analytical grade HCl solution was added, and the flask was purged with N_2 gas for 20 min to clean and activate the zinc pellets' surface. The 2M analytical grade HCl solution was then extracted before chromium solution was added, and the reaction flask was purged with N_2 gas for 45 min. The reduction of the solution from chromic (III) to chromous (II) chloride solution resulted in a color change from dark green to clear bright blue. When the solution had been reduced, syringes with syringe valves were used to extract and store the reduced chromium

solution in a refrigerator at 4˚C. The chromium solution's color was always checked before use to ensure it was still reduced. If it had oxidized, it would turn back to dark green and had to be discarded.

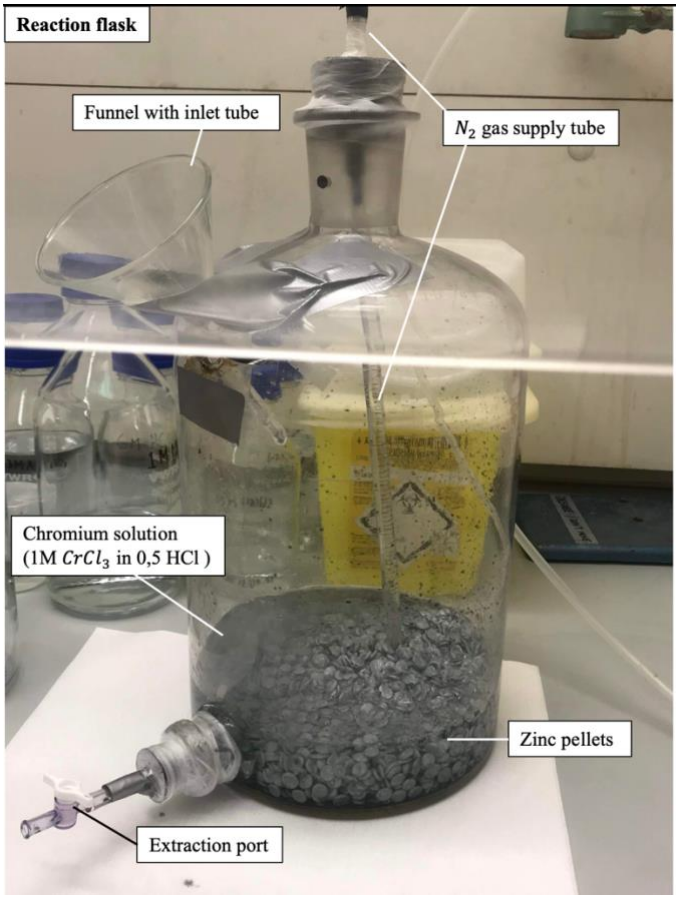

Figure 4.1: Reaction flask setup containing an inlet tube connected to a funnel at the top for adding reagents and a port at the bottom for extracting solutions. It is filled with zinc pellets and chromium solution and is connected by tubes to N_2 gas supply. Picture taken by Karen Elisabeth Moltubakk.

The third step was to perform chromium distillation on the samples to produce Ag_2S. For this, an extraction line setup was used (Figure 4.2). First, the $AgNO_3$ trap was made in a test tube. The trap's volume was 15 ml, and its capacity would be to trap 15-20 mg Ag_2S. Therefore, 15-20 mg of sample was used for all the individual samples to ensure that the generated H_2S did not exceed the trap capacity. After this, the sample was weighed into a round bottom flask ca. 5ml ultrapure water was added to keep the sample in place, and boiling stones were added to avoid flash boiling. The system was then flushed with N_2 gas for 5 minutes at a 2-3 bubbles per second rate to check for any leaks and ensure a reducing environment (low O_2). Under continuous N_2 flow, 40 ml of reduced chromium solution and 20 ml 6M HCl were quickly added to the round bottom flask with syringes, to ensure minimal oxygen getting into the

system. Then the heating mantles were turned on, and the solution was boiled for two hours. In the three-neck round bottom flask, $H_2S_{(g)}$ was produced through the reactions:

$$FeS_{(s)} + 2H^+_{(aq)} = H_2S_{(g)} + Fe^+_{2\,(aq)} \quad (4.1)$$

$$FeS_{2\,(s)} + 4H^+_{(aq)} + 2Cr^+_{2\,(aq)} = 2H_2S_{(g)} + Fe2^+_{(aq)} + 2Cr3^+_{(aq)} \quad (4.2)$$

In the traps, the $H_2S_{(g)}$ reacted with the acidic silver nitrate solution ($AgNO_3$) and generated insoluble silver sulfide through the reaction:

$$H_2S_{(g)} + 2Ag^+_{(aq)} = Ag_2S_{(s)} + 2H^+_{(aq)} \quad (4.3)$$

Most of the Ag_2S was produced during the firs 45 minutes of the reaction, so the sample was discarded if a leak occurred during this time.

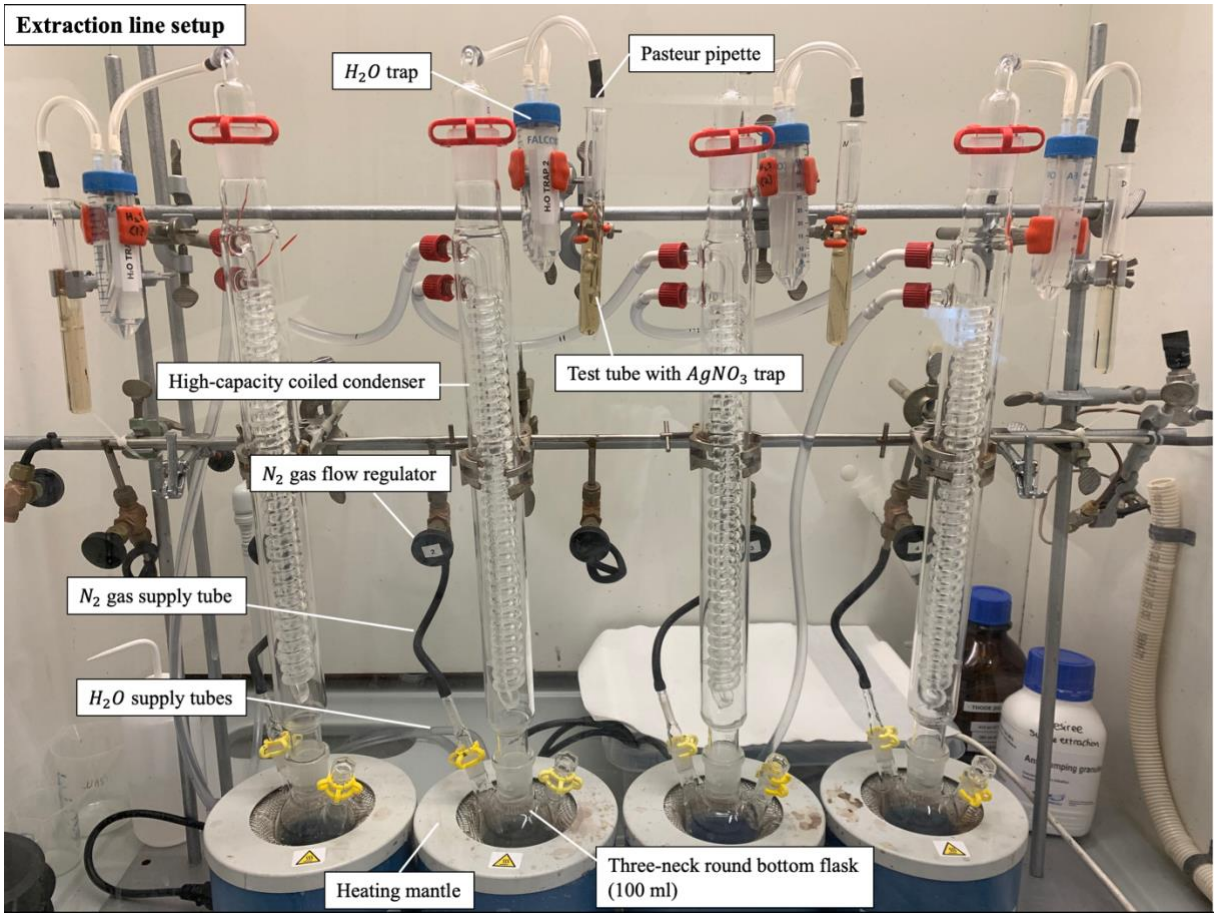

Figure 4.2: Extraction line setup containing N_2 gas regulator connected to four $AgNO_3$ traps, four water traps, and four three-neck 100ml round bottom flasks through gas inlet tubes. Four high-capacity coiled condensers with tubing to and from the water supply, also connected to their respective $AgNO_3$ trap, water trap, and three-neck 100ml round bottom flask sitting in a heating mantle.

The fourth step was vacuum filtration and drying the Ag_2S precipitate. For each sample, a 47mm diameter 0,45 um cellulose-acetate filter was weighed and then placed on a vacuum filtration apparatus. The silver nitrate traps containing the Ag_2S were poured on the filter, taking care to remove all precipitate by flushing the traps and Pasteur pipettes with ultrapure water. After flushing, the filter was rinsed with 1M NH_4OH to dissolve any AgCl that may have formed and then filtrated again. Next, the filter was placed in a plastic weighing cup for air drying and weighed again when dry to determine distillation yield. Ag_2S was then scraped from the dry filters, placed in glass vials, and sent to Munster, Germany.

4.3 Isotope analysis

The $Ag_2S_{(s)}$ was sent to the Stable Isotope Laboratory at Westfälische Wilhelms-Universität Münster for multiple sulfur isotope analyses. The $Ag_2S_{(s)}$ from both the hydrothermal rock and fluid samples were converted to SF_6 by reacting with F_2 in Ni reaction vessels as described by

Ono et al. (2006). The SF_6 was then purified after Farquhar et al. (2007) by chromatographic and cryogenic methods. A dual-inlet system Thermo Scientific MAT 353 mass spectrometer was used to simultaneously measure 32S, 33S, and 36S (Eickman et al., 2014). For high precision measurements of the sulfur isotopes ratios $\delta^{33}S$, $\delta^{34}S$, $\delta^{36}S$. All values are reported relative to V-CDT and calculated using the IAEA-S1 standard, defined following Ono et al. (2007) with δ34S = -0,300‰, δ33S = -0,055‰, and δ36S = -1,37‰. The $Ag_2S_{(s)}$ from the hydrothermal rock samples and the hydrothermal fluid samples were analyzed separately over two different time periods.

CHAPTER 5: RESULTS

5.1 Sample descriptions

Table 5.1 shows the physical properties in focus for identifying the hand-picked sulfides, observed in the stereo microscope and SEM. It also includes the most abundant elements detected in the SEM in an approximate order of abundance based on EDS peaks. The elements included in the table are only those of highest abundance (highest EDS peaks) necessary for sulfide identification. Observations of hand-picked sulfides in the SEM with much greater magnification than stereo microscope revealed that different sulfides had grown on other sulfides surface (Figure 5.1, 5.2 and 5.3). However, the sulfides growing on surfaces make out a significantly smaller part of the sample and will therefore have minimal contribution to the isotopic signature compared to the major sulfide. An exception is sample GS19-ROV20-R01-N1 has both pyrrhotite and sphalerite as significant sulfides. A more detailed investigation of the sample in the SEM revealed that this sample contained both a significant amount of pyrrhotites and sphalerites. The sphalerites were missed in the stereo microscope because of their similar color to the pyrrhotites and their slightly magnetic behavior plausibly due to them being surrounded by numerous small sheets of pyrrhotite. In general, the hand-picked chimney samples could contain other sulfides than those found by hand-picking in stereo microscope if the sulfides are too small to be recognized.

The Seven Sisters chimney sample from Lily mound (GS18-ROV08-R01) did not contain any sulfides visible in the stereo microscope and no sulfides were picked from that sample, but he Hodr chimney sample (GS18-ROV08-R05) was found to be the only chimney sample containing Marcasite (FeS_2), (Figure 5.2e) identified by its characteristic arrowhead shape and light-brass color.

The Soria Moria (Jan Mayen) chimney sample from Soria Moria chimney were found to contain sphalerites ((Zn,Fe)S)) mainly identified by high zinc content, (Figure 5.2f). Lilleputt chimney were found to contain pyrrhotites, mainly identified by their characteristic magnetic property (FeS), (Figure 5.3a and b).

The Fåvne vent field North Tower chimney samples were found to contain sphalerites and pyrrhotites (Figure 5.3c, d, e and f). The sample from South Tower (GS19-ROV16-R01) did not contain any visible sulfides in the stereo microscope and could not be hand-picked.

The Loki's Castle chimney samples contain the highest variety of sulfides. The Joao chimney sample (GS17-ROV17-R01) were found to contain three different sulfides by hand-picking sphalerite, (Figure 5.1a), chalcopyrite ($CuFeS_2$), (Figure 5.1b) and pyrrhotite. This is the only sample found to contain a significant amount of copper sulfides. The copper sulfides were identified to be chalcopyrite, they could potentially be bornite (Cu_5FeS_4), but their iridescent tarnish and copper EDS peaks being lower than iron and sulfur EDS peaks fits better with chalcopyrite's characteristics. The Joao chimney sample (GS19-ROV20-R01) was found to only contain significant amounts of sphalerite (Figure 5.1c) and pyrrhotite (Figure 5.1d).

Table 5.1: physical properties handpicked sulfides observed in stereo microscope and SEM, most abundant elements detected in SEM in approximate descending order, identified sulfide The identified minerals in the column furthest right are the mineral that make out most of that specific sample.

Sample ID	Vent field	Chimney	Color	Lustre	External shape	Magnetism	Elemnts (~descending order of abundance)	Mineral
GS17-ROV17-R01-A1	Loki's Castle	Joao	dark, brown-black	metallic	hexagonal sheets and irregular sheets	magnetic	Fe, S	pyrrhotite
GS17-ROV17-R01-A2	Loki's Castle	Joao	dark brown-black	sub-metallic to metallic	tetrahedra clustres	no	Zn, S, Fe	sphalerite
GS17-ROV17-R01-A3	Loki's Castle	Joao	brass, iridescent tarnish	metallic	irregular	no	Fe, S, Cu	chalcopyrite
GS19-ROV20-R01-N1	Loki's Castle	Joao	dark, brown-black	metallic	hexagonal sheets and tetrahedron clustres	slightly magnetic	Fe, S + Zn, S, Fe	pyrrhotite + sphalerite
GS17-ROV19-R02-C1	Loki's Castle	Sleepy	dark, brown-black	metallic	irregular sheets	magnetic	Fe, S	pyrrhotite
GS17-ROV19-R03-D1	Loki's Castle	Menorah	dark, brown-black	metallic	irregular sheets	magnetic	Fe, S	pyrrhotite
GS18-ROV22-R02-K1	Loki's Castle	Camel	dark, brown-black	metallic	irregular sheets	magnetic	Fe, S	pyrrhotite
GS18-ROV08-R05-F1	Seven Sisters	Hodr	light brass	metallic	elongated triangle (arrowhead)	no	Fe, S	marcasite
GS18-ROV14-R01-G1	Jan Mayen	Soria Moria	golden yellow	sub-metallic	irregular	no	Zn, S (Fe)	sphalerite
GS18-ROV14-R03-H1	Jan Mayen	Lilleputt	golden yellow	sub-metallic	Irregular, some tetrahedron	no	Zn, S	sphalerite
GS19-ROV16-R02-M1	Fåvne	North Tower	dark brown-black	metallic	Irregular, some heaxagonal sheets	magnetic	Fe, S	pyrrhotite
GS19-ROV16-R02-M2	Fåvne	North Tower	golden yellow	sub-metallic	Irregular and tetrahedron clustres	no	Zn, S, Fe	sphalerite

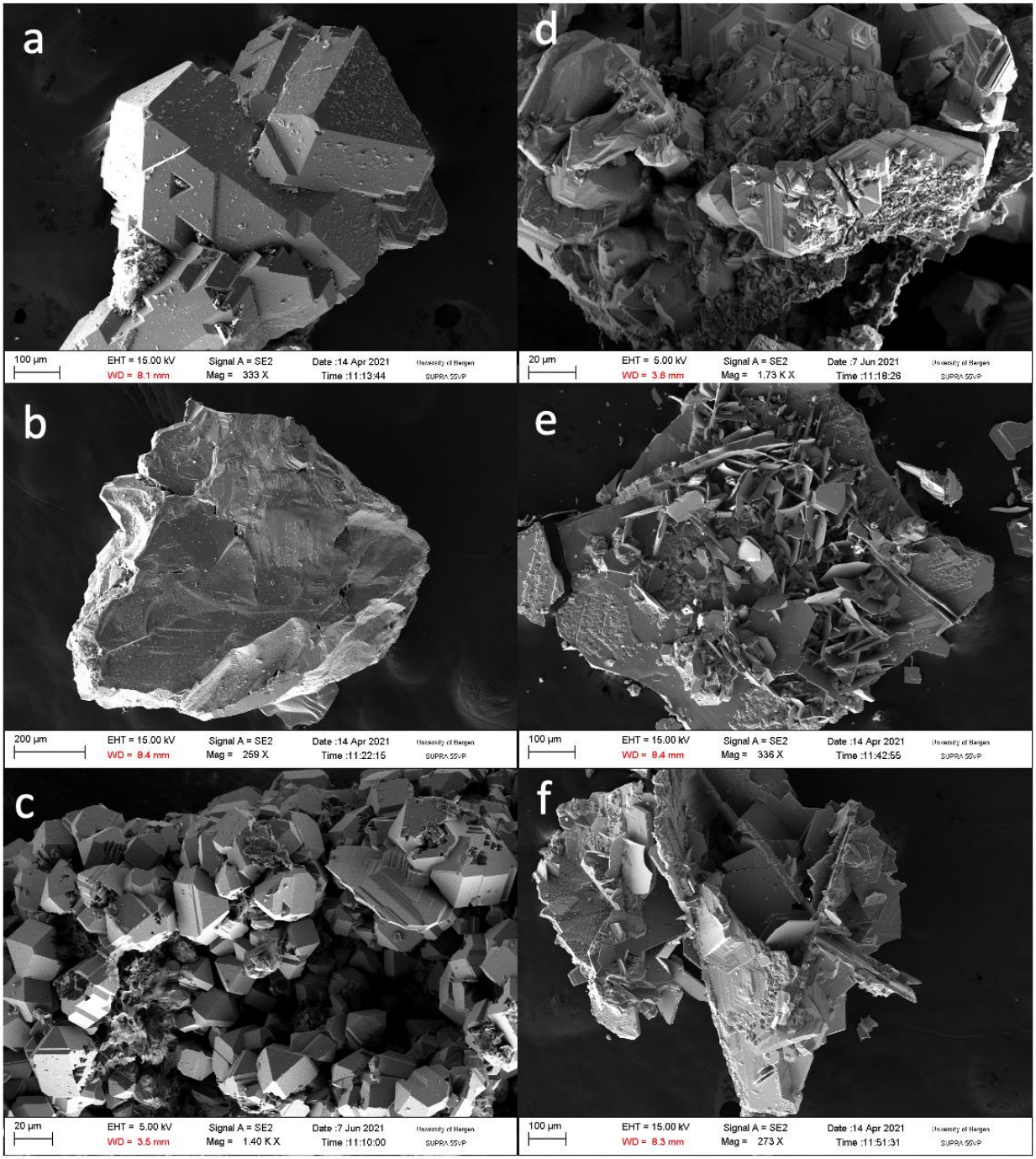

Figure 5.1: (a) GS17-ROV17-R01-A2, Loki's Castle, Joao chimney, sphalerite. **(b)** GS17- ROV17-R01-A3, Loki's Castle, Joao chimney, chalcopyrite. **(c)** GS19-ROV20-R01-N1, Loki's Castle, Joao chimney, sphalerite with some pyrrhotite. **(d)** GS19-ROV20-R01-N1 Loki's Castle, Joao chimney, mostly pyrrhotite with another sulfide growing on surface. **(e)** GS17-ROV19-R02-C1, Loki's Castle, Sleepy chimney pyrrhotite. **(f)** GS17-ROV19-R02-C1, Loki's Castle, Sleepy chimney, pyrrhotite.

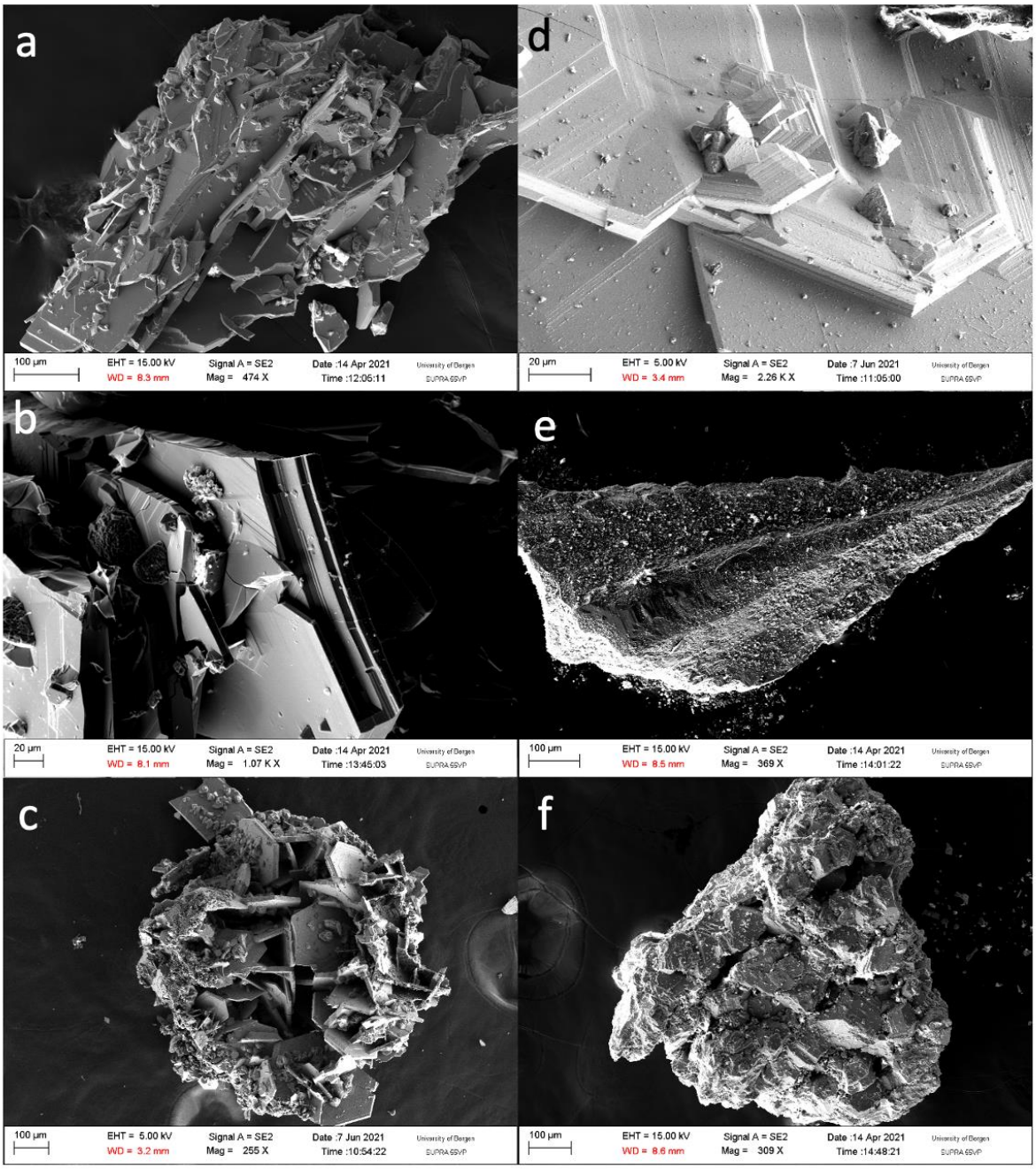

Figure 5.2: (a) GS17-ROV19-R03-D1, Loki's Castle, Menorah chimney, pyrrhotite with other sulfide growing on surface. **(b)** GS17-ROV19-R03-D1, Loki's Castle, Menorah chimney, pyrrhotite with other sulfide growing on surface. **(c)** GS18-ROV22-R02-K1, Loki's Castle, Camel chimney, pyrrhotite with other sulfides growing on surface. **(d)** GS18-ROV22-R02-K1, Loki's Castle, Camel chimney, pyrrhotite with other sulfides growing on surface. **(e)** GS18-ROV08-R05-F1, Seven Sisters, Hodr chimney, marcasite. **(f)** GS18-ROV14-R01-G1, Soria Moria (Jan Mayen), Soria Moria chimney, sphalerite

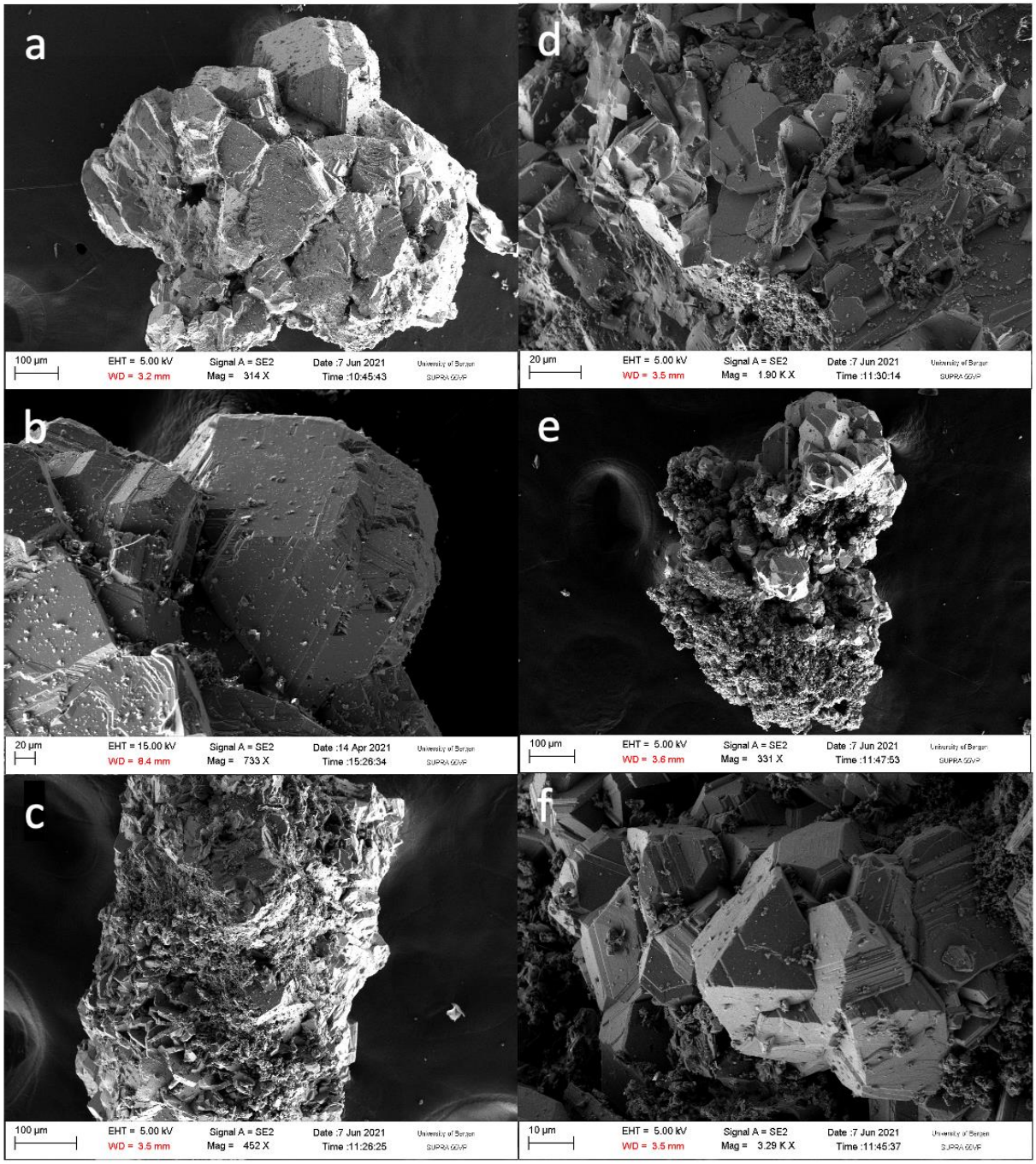

Figure 5.3: (a) GS18-ROV14-R03-H1, Soria Moria (Jan Mayen), Lilleputt chimney, sphalerite. **(b)** GS18-ROV14-R03-H1, Soria Moria (Jan Mayen), Lilleputt chimney, sphalerite. **(c)** GS19-ROV16-R02-M1, Fåvne, North Tower chimney, pyrrhotite. **(d)** GS19-ROV16-R02-M1, Fåvne, North Tower chimney, pyrrhotite. **(e)** GS19-ROV16-R02-M2, Fåvne, North Tower chimney, sphalerite. **(f)** GS19-ROV16-R02-M2, Fåvne, North Tower chimney, sphalerite.

5.2 Multiple sulfur isotopes

All hydrothermal fluid, chimney bulk and hand-picked samples were converted to Ag_2S and analyzed. All values are given in respect to V-CDT and calculated using the IAEA-S1 standard, defined following Ono et al. (2007) with $\delta^{34}S$ = -0,300‰, $\delta^{33}S$ = -0,055‰, and $\delta^{36}S$ = -1,37 ‰. The Ag_2S from the hydrothermal rock samples and the hydrothermal fluid samples were analyzed separately over two different time periods and therefore have different precisions. The external precision (2σ) for the hydrothermal rock samples was taken from IAEA-S1 (n = 9) measurements and are 0,09‰ for $\delta^{34}S$, 0,017‰ for $\Delta^{33}S$, and 0,331‰ Δ36S. The external precision (2σ) for the hydrothermal fluid samples was taken from IAEA-S1 (n = 4) measurements and are 0,017‰ for $\delta^{34}S$, 0,007‰ for $\Delta^{33}S$, and 0,355‰ $\Delta^{36}S$. $\Delta^{33}S$ and $\Delta^{36}S$ in this study are defined following Ono et al. (2007), where the capital delta notation is calculated linearly:

$$\Delta^{33}S = \delta^{33}S - 0{,}515 \cdot \delta^{34}S \quad (5.1)$$

$$\Delta^{36}S = \delta^{36}S - 1{,}9 \cdot \delta^{34}S \quad (5.2)$$

The $\Delta^{36}S$ measurements have significantly lower precision than $\Delta^{33}S$ and therefore will not provide any additional information and will not be discussed further (see Appendix 2 and 3).

Table 5.2 displays $\delta^{34}S$ values and $\Delta^{33}S$ for all chimney samples, both bulk and hand-picked. Sample GS19-ROV-16-R01 from Fåvne South Tower chimney (Table 4.2) is not included as it did not contain enough sulfide to be analyzed (produced less than 3 mg Ag_2S). The $\delta^{34}S$ values of all chimney samples have a range of -1,62‰ to 10,39‰ +- 0,09‰ (2σ, n=9) and the majority have values in the range between sulfide derived from MORB ($\delta^{34}S = -0{,}91 \pm 0{,}50$‰ from Labidi et al. (2012)), and sulfide derived from seawater ($\delta^{34}S \approx 21{,}5$‰ from Ono et al. (2007)) value. While $\Delta^{33}S$ values range from -0,0175‰ to 0,0171‰ +- 0,02‰ (2σ, n=9) which is both below and above MORB derived sulfide ($\Delta^{33}S \approx 0$ from Labidi et al. (2012)) and seawater derived sulfide ($\Delta^{33}S \approx$ -0,008 from Ono et al. (2007)).

Table 5.3 displays $\delta^{34}S$ values and $\Delta^{33}S$ values for all hydrothermal fluid samples. Fluids GS19-ROV16-IGT1+IGT2 from Fåvne, North Tower chimney could not be analyzed (less than 3mg Ag2S could be retrieved from filters). The $\delta^{34}S$ values of all hydrothermal fluid samples have a range of 2,36‰ to 4,79‰ +- 0,02‰ (2σ, n=4) and fall between sulfide derived from MORB ($\delta^{34}S = -0{,}91 \pm 0{,}50$‰ from Labidi et al. (2012)) and sulfide derived from seawater ($\delta^{34}S \approx 21{,}5$‰ from Ono et al. (2007)) value. However, $\Delta^{33}S$ values range from -0,032‰ to -0,013‰ +- 0,007‰ (2σ, n=4) which is lower than values between MORB ($\Delta^{33} \approx 0$ from Labidi et al. (2012)) and seawater ($\Delta^{33}S \approx$ -0,008 from Ono et al. (2007)).

Table 5.2: Sulfur isotopes results for all bulk and hand-picked chimney samples, $\delta^{34}S$ values and linear $\Delta^{33}S$ all values are given with respect to the V-CDT standard. Mineral abbreviations follows Whitney and Evans (2010). The column "Material" displays the major sulfide making out samples and bulk samples.

Sample ID	Vent field	Chimney	Material	δ34S [‰]	± 2σ [‰]	Δ33S [‰]	± 2σ [‰]
GS17-ROV17-R01-A0	Loki's Castle	Joao	Bulk	3,52	0,09	-0,0073	0,02
GS17-ROV17-R01-A1	Loki's Castle	Joao	Po	2,96	0,09	-0,0097	0,02
GS17-ROV17-R01-A2	Loki's Castle	Joao	Sp	3,66	0,09	-0,0175	0,02
GS17-ROV17-R01-A3	Loki's Castle	Joao	Ccp	3,51	0,09	0,0068	0,02
GS19-ROV20-R01-N0	Loki's Castle	Joao	Bulk	3,13	0,09	-0,0088	0,02
GS19-ROV20-R01-N1	Loki's Castle	Joao	Po + Sp	3,30	0,09	-0,0070	0,02
GS17-ROV19-R02-C0	Loki's Castle	Sleepy	Bulk	3,29	0,09	-0,0038	0,02
GS17-ROV19-R02-C1	Loki's Castle	Sleepy	Po	3,24	0,09	-0,0006	0,02
GS17-ROV19-R03-D0	Loki's Castle	Menorah	Bulk	3,01	0,09	0,0005	0,02
GS17-ROV19-R03-D1	Loki's Castle	Menorah	Po	2,76	0,09	-0,0071	0,02
GS18-ROV22-R02-K0	Loki's Castle	Camel	Bulk	3,23	0,09	-0,0128	0,02
GS18-ROV22-R02-K1	Loki's Castle	Camel	Po	2,91	0,09	-0,0105	0,02
GS18-ROV08-R01-E0	Seven sisters	Lily	Bulk	-1,01	0,09	-0,0013	0,02
GS18-ROV08-R05-F0	Seven sisters	Hodr	Bulk	-1,62	0,09	0,0171	0,02
GS18-ROV08-R05-F1	Seven sisters	Hodr	Mrc	-1,56	0,09	0,0127	0,02
GS18-ROV14-R01-G0	Jan Mayen	Soria Moria	Bulk	0,96	0,09	0,0099	0,02
GS18-ROV14-R01-G1	Jan Mayen	Soria Moria	Sp	1,22	0,09	-0,0030	0,02
GS18-ROV14-R03-H0	Jan Mayen	Lilleputt	Bulk	0,71	0,09	-0,0042	0,02
GS18-ROV14-R03-H1	Jan Mayen	Lilleputt	Po	1,04	0,09	0,0023	0,02
GS19-ROV16-R02-M0	Fåvne	North Tower	Bulk	10,07	0,09	0,0023	0,02
GS19-ROV16-R02-M1	Fåvne	North Tower	Po	9,93	0,09	0,0054	0,02
GS19-ROV16-R02-M2	Fåvne	North Tower	Sp	10,39	0,09	0,0024	0,02

Table 5.3: Sulfur isotopes results for all fluid samples, $\delta^{34}S$ values and linear $\Delta^{33}S$, all values are are given with respect to the V-CDT standard.

Sample ID	Vent field	Chimney	δ34S [‰]	± 2σ [‰]	Δ33S [‰]	± 2σ [‰]
GS17-ROV17-IGT3	Loki's Castle	Joao	4,15	0,02	-0,0206	0,007
GS17-ROV17-IGT2	Loki's Castle	Joao	4,33	0,02	-0,0254	0,007
GS17-ROV19-IGT2	Loki's Castle	Sleepy	4,79	0,02	-0,0320	0,007
GS17-ROV19-IGT3	Loki's Castle	Sleepy	4,45	0,02	-0,0192	0,007
GS17-ROV19-IGT4+ROV21-IGT4	Loki's Castle	Menorah	4,16	0,02	-0,0278	0,007
GS18-ROV14-IGT1+IGT2	Jan Mayen	Soria Moria	2,36	0,02	-0,0232	0,007
GS18-ROV14-IGT3+IGT4	Jan Mayen	Lilleputt	3,72	0,02	-0,0131	0,007

Seven sisters

Samples from Seven sisters have the lowest $\delta^{34}S$ values and are depleted in ^{34}S compared to the other vent fields (Figure 5.4). Also, $\delta^{34}S$ values of Seven Sisters chimney samples do not fall between MORB and seawater derived sulfide values, but rather the sample from Lily chimney (GS18-ROV08-R01-E0) have a $\delta^{34}S$ value of -1.01‰ $\pm$ 0.09‰ (2σ, n=9) which fall on the MORB derived sulfide value and the $\delta^{34}S$ values of the Hodr samples -1.62‰, -1.56‰ $\pm$ 0.09‰ (2σ, n=9) are sligtly below the MORB derived sulfide value. The data points for the the Seven Sisters samples have a strong linear relationship with a near perfect negative correlation (R^2=0,979) (Figure 5.5). Figure 5.6a shows that Hodr chimney is depleted in 34S compared to Lily chimney and that the $\Delta^{33}S$ values are above zero for Hodr ($\Delta^{33}S = 0{,}0171,\ 0.0127\ 0{,}02‰\ (2\sigma,\ n = 9)$) and below zero for Lily ($\Delta^{33}S = -0{,}013 \pm 0{,}02‰\ (2\sigma,\ n = 9)$). Figure 5.6a also shows that the sulfur isotopic composition of bulk and Mrc from Hodr chimney are very similar indicating the analysis of isotopes only includes the sulfides. Therefore, analysis of the Lily bulk sample is assumed to be an accurate representation of multiple isotope composition in sulfides with no contribution from other sulfur species.

Soria Moria (Jan Mayen)

$\delta^{34}S$ values in Soria Moria (Jan Mayen) samples are higher than in Seven Sisters samples, all samples fall between 0,5‰ and 2,5‰ one sample has a value above 3,5‰. This is the Lilleputt fluid sample (GS18-ROV14-IGT3+IGT4), Figure 5.4a. This is also the only sample with a $\delta^{34}S$ value that falls in the range of $\delta^{34}S$ values of Loki's Castle samples. Figure 5.4b (red dotted line) shows the linear relationship of all the Soria Moria (Jan Mayen) data points with negative correlation of R^2= 0,467 including sample GS18-ROV14-IGT3+IGT4 that falls

within the Loki's Castle samples range. Whereas Figure 5.4b (black dotted line) shows a stronger linear relationship with negative correlation of R^2= 0,712 for the Soria Moria (Jan Mayen) samples when the sample GS18-ROV14-IGT3+IGT4 is excluded. Sample GS18-ROV14-IGT3+IGT4 stands out as different from the others and could potentially be an outlier that has been affected by error while sampling. Though this cannot be determined with certainty and is why both linear correlations is are shown in Figure 5.4b. Soria Moria (Jan Mayen) fluid-solid pairs are displayed in Figure 5.5b including the Lilleputt fluid sample (GS18-ROV14-IGT3+IGT4). There is a significant enrichment of ^{34}S and a slight depletion in ^{33}S in the fluids seen in Figure 5.5b as a left- and downward shift from the solids to the fluids. The vertical error bars representing precision in $\Delta^{33}S$ values slightly overlap indicating not lower values within the 95% confidence interval. However it is more likely that there is a shift of lower measured $\Delta^{33}S$ values in the fluids compared to the chimney samples. Figure 5.6b, shows the sulfur isotopic composition of sulfides from the Soria Moria and Lilleput chimney are similar. It also displays the minimal variation between hand-picked sulfides and bulk samples. This indicates a successful analysis where only sulfides are analyzed, and no error source of other sulfur species are contributing to the multiple sulfur isotopic composition of the bulk samples.

Fåvne

The North Tower chimney samples from Fåvne have significantly higher $\delta^{34}S$ values and are the most ^{34}S enriched of the four vent fields, The North Tower samples have positive $\Delta^{33}S$ values slightly higher than $\Delta^{33}S$ values of MORB and seawater derived sulfides (Figure 5.4a). Like the two other vent fields the data points for Fåvne samples have a negative linear relationship. The linear regression line (red dotted line) has the weakest correlation of R^2= 0,533 due to two data point plotting next to each other. Therefore, an alternative regression line (red dotted line) is plotted to better fit the data with a correlation of R^2=1, (Figure 5.4b). Figure 5.6d shows that similarly to the two other vent fields there is minimal variation in the multiple isotopic composition of hand-picked sulfides and bulk samples. Again, indicating no error source of other sulfur species contributing to the isotopic composition of bulk samples.

Loki's Castle

Figure 5.4 shows that samples from Loki's Castle have $\delta^{34}S$ values of 2,76‰ to 4,79‰, which is higher than the Seven Sisters and the Soria Moria (Jan Mayen) vent field values and the Loki's Castle samples have the widest range in $\Delta^{33}S$ values from -0,032 $\pm$ 0,007‰ (2σ, n = 4) to 0,0068 ‰ $\pm$ 0,02‰ (2σ, n = 9), with majority of values below MORB and seawater derived sulfides. The data points of the Loki's Castle samples have a similar linear relationship

to the three previously mentioned vent fields, displayed in Figure 5.4b, with a negative correlation of R^2= 0,596. Loki's Castle fluid-solid pairs are displayed in Figure 5.5a, like the Soria Moria (Jan Mayen) fluid-solid pairs there is a significant enrichment of ^{34}S and a slight depletion of ^{33}S in the fluids compared to the solids and they have a similar left- and downward shift from the solids to the fluids for the measured values (Figure 5.6a). Also, the Loki's Castle fluid Δ^{33} values are lower than chimney values within the 95% confidence interval. Figure 5.6c shows analogous to the other three vent field there is minimal variation between the multiple sulfur isotopic composition of hand-picked and bulk samples. A good indication for a successful analysis of only sulfide sulfur, and no other sulfur spices have contributed to the isotopic composition.

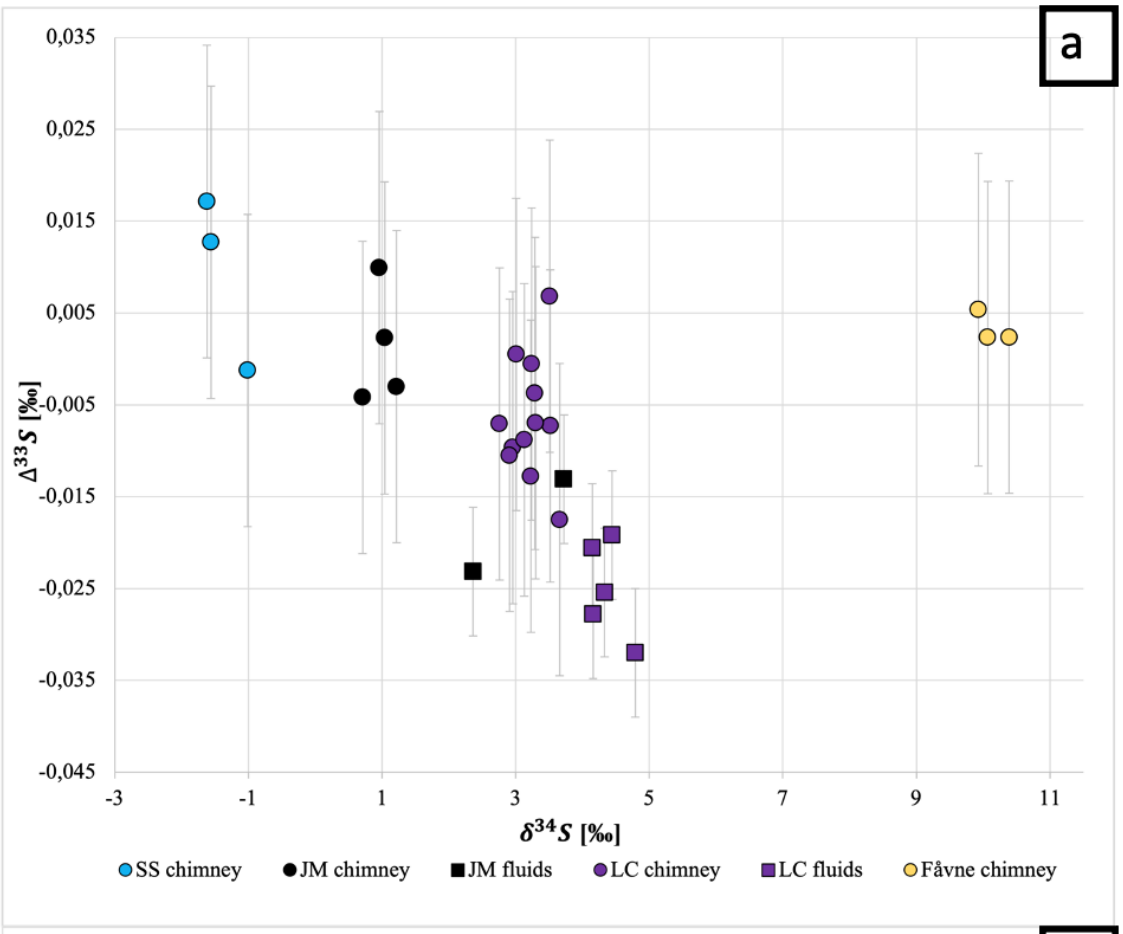
a
0,035
0,025
0,015
0,005
-0,005
-0,015
-0,025
-0,035
-0,045
-3
-1
1
3
5
7
9
11
$\Delta^{33}S$ [‰]
$\delta^{34}S$ [‰]
SS chimney
JM chimney
JM fluids
LC chimney
LC fluids
Fåvne chimney

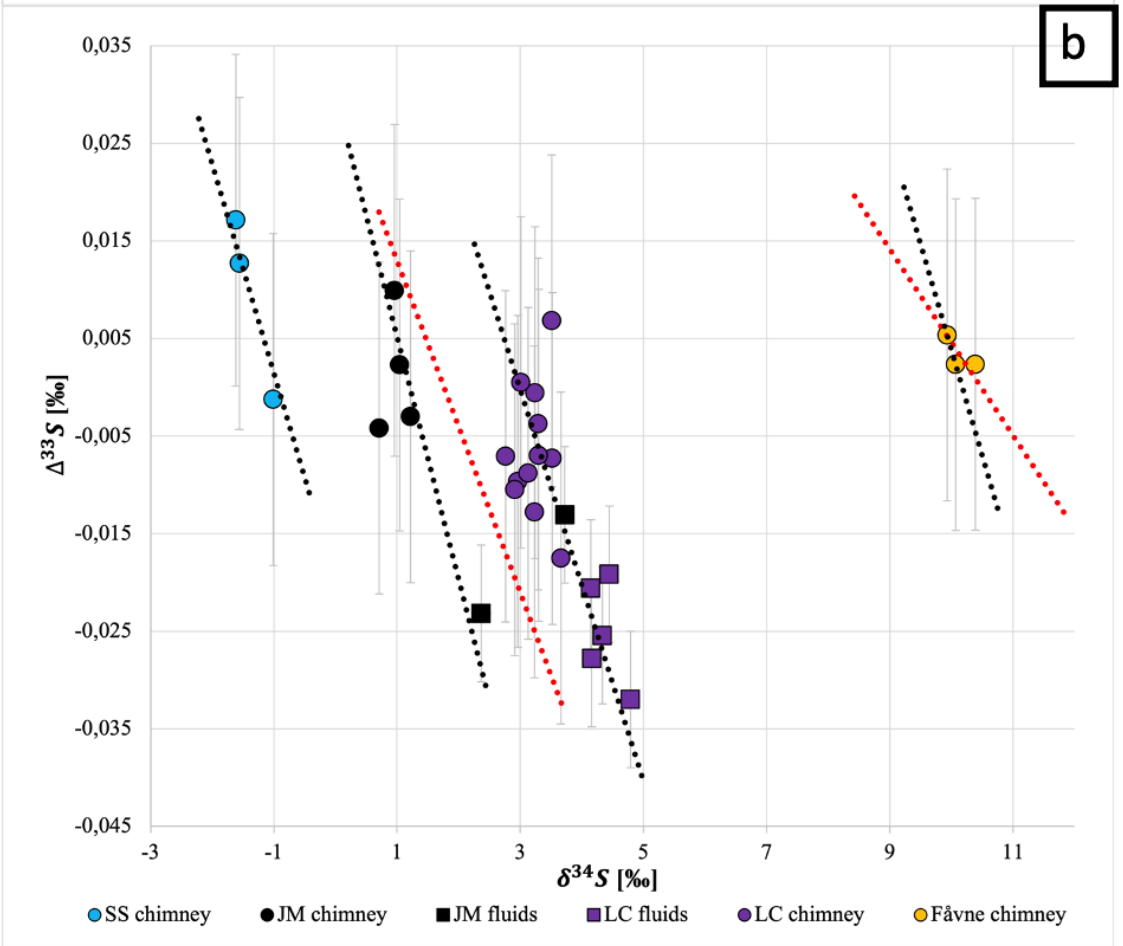
b
0,035
0,025
0,015
0,005
-0,005
-0,015
-0,025
-0,035
-0,045
-3
-1
1
3
5
7
9
11
$\Delta^{33}S$ [‰]
$\delta^{34}S$ [‰]
SS chimney
JM chimney
JM fluids
LC fluids
LC chimney
Fåvne chimney

Figure 5.4: (a) Plot of $\delta^{34}S$ vs $\Delta^{33}S$ showing all hydrothermal chimney and fluid samples. Error bars represents 2σ. Fluid sample errors for $\delta^{34}S$ ($\pm$ 0,02‰) and chimney sample errors $\delta^{34}S$ ($\pm$ 0,09‰) are approximately equivalent to the size of the symbols. **(b)** Plot of $\delta^{34}S$ vs $\Delta^{33}S$ showing the linear correlation of the data points for each vent field. The black dotted lines: Seven Sisters (R^2= 0,979), Jan Mayen (Soria Moria) (R^2= 0,712), Loki's Castle (R^2=0,596), Fåvne (R^2=1). Red dotted lines**:** Soria Moria (Jan Mayen) (R^2=0,467), Fåvne (R^2=0,533). SS = Seven Sisters vent field, JM = the Jan Mayen vent field Soria Moria, LC = Loki's Castle vent field.

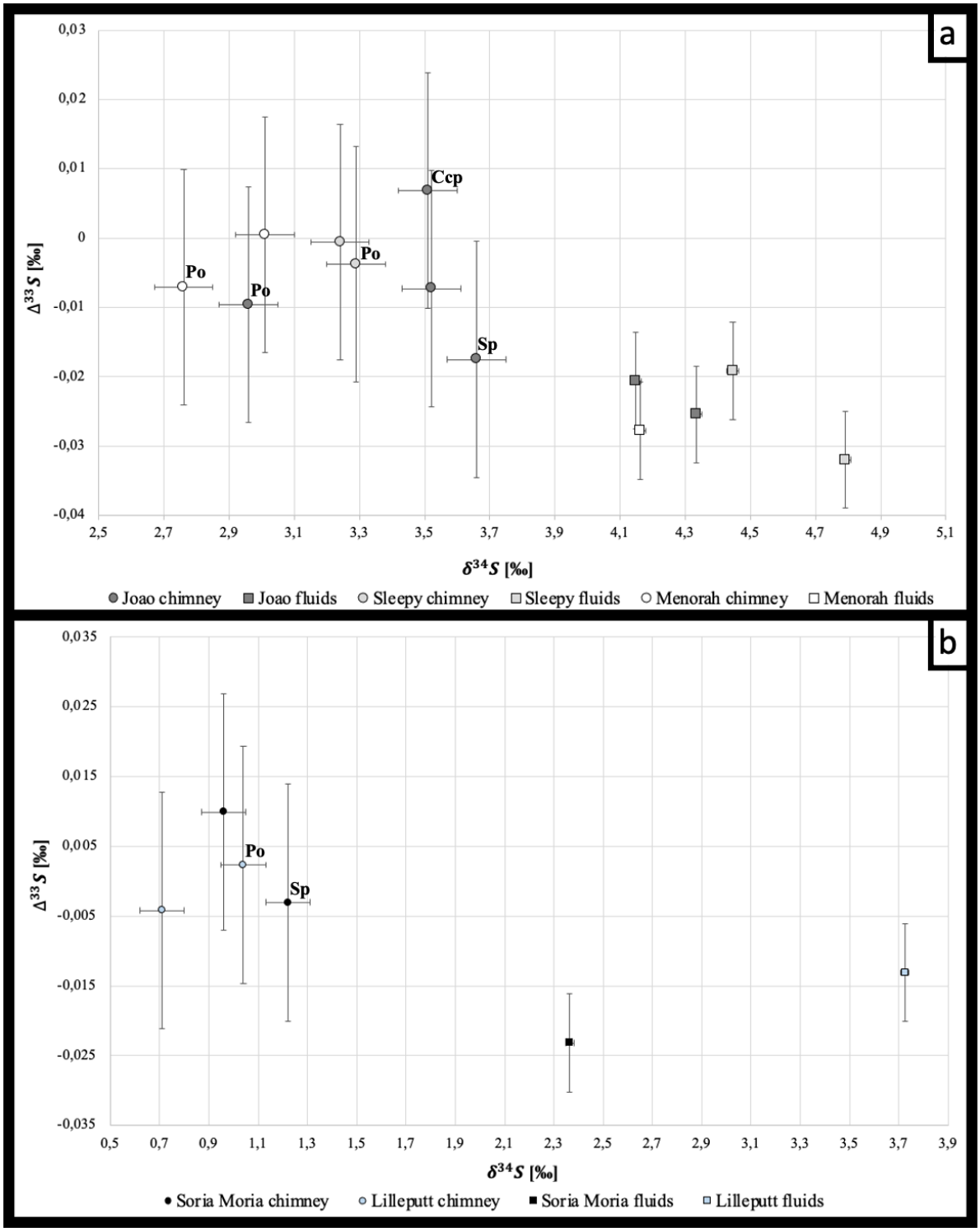

Figure 5.5: (a) $\delta^{34}S$ vs $\Delta^{33}S$ showing fluid-solid pairs of Lokis Castle samples including hand-picked sulfides. **(b)** $\delta^{34}S$ vs $\Delta^{33}S$ showing fluid-solid pairs of Soria Moria (Jan Mayen) samples including hand-picked sulfides. Chimney samples without mineral abbreviations represents bulk samples. Error bars represents 2σ. Fluid samples errors for $\delta^{34}S$ ($2\sigma = \pm 0{,}02‰$) are approximately equivalent to the size of the symbols.

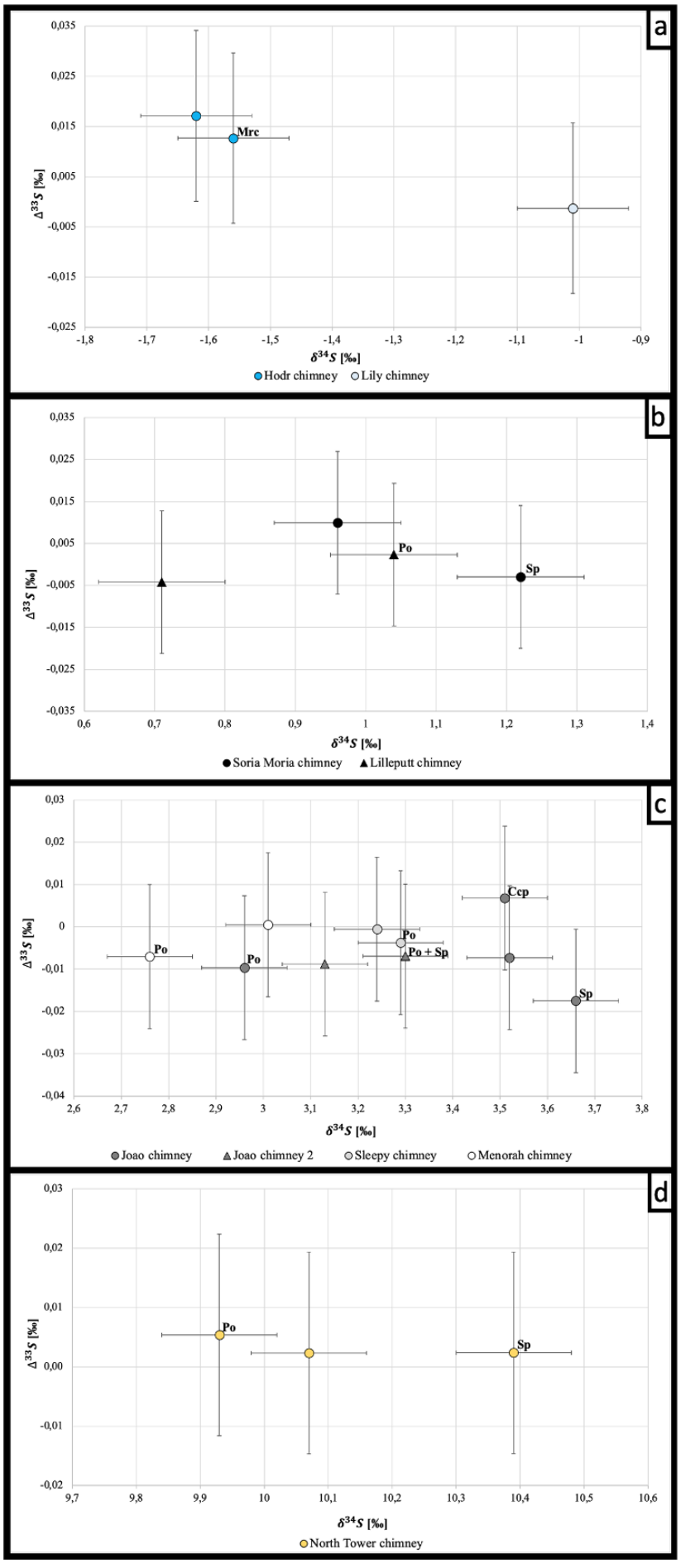
a
0,035
0,025
0,015
0,005
-0,005
-0,015
-0,025
-1,8
-1,7
-1,6
-1,5
-1,4
-1,3
-1,2
-1,1
-1
-0,9
Mrc
$\Delta^{33}S$ [‰]
$\delta^{34}S$ [‰]
Hodr chimney
Lily chimney
b
0,035
0,025
0,015
0,005
-0,005
-0,015
-0,025
-0,035
0,6
0,7
0,8
0,9
1
1,1
1,2
1,3
1,4
Po
Sp
$\Delta^{33}S$ [‰]
$\delta^{34}S$ [‰]
Soria Moria chimney
Lilleputt chimney
c
0,03
0,02
0,01
0
-0,01
-0,02
-0,03
-0,04
2,6
2,7
2,8
2,9
3
3,1
3,2
3,3
3,4
3,5
3,6
3,7
3,8
Ccp
Po
Po
Po
Po + Sp
Sp
$\Delta^{33}S$ [‰]
$\delta^{34}S$ [‰]
Joao chimney
Joao chimney 2
Sleepy chimney
Menorah chimney
d
0,03
0,02
0,01
0,00
-0,01
-0,02
9,7
9,8
9,9
10
10,1
10,2
10,3
10,4
10,5
10,6
Po
Sp
$\Delta^{33}S$ [‰]
$\delta^{34}S$ [‰]
North Tower chimney

Figure 5.6: Plots of $\delta^{34}S$ vs $\Delta^{33}S$ showing hand-picked and bulk sulfide samples from all the four vent fields. Error bars represents 2σ. Chimney samples without mineral abbreviations represents bulk samples. **(a)** Seven Sisters. **(b)** Soria Moria (Jan Mayen). **(c)** Loki's Castle (Joao chimney = GS17-ROV17-R01-A0, A1, A2, A3, Joao chimney 2 = GS19-ROV20-R01-N0, -N1). **(d)** Fåvne.

CHAPTER 6: DISCUSSION

The aim of this discussion is to investigate variations in sulfur cycling at active high temperature seafloor hydrothermal systems the Arctic Mid Ocean Ridges. This is done through a two stage model developed by Ono et al. (2007) that uses multiple sulfur isotopes to put constraints on input from thermochemical sulfate reduction, basalt leaching and anhydrite dissolution.

6.1 Sulfur isotope constraints on sulfide sources

High temperature water-rock interactions in mid ocean ridge hydrothermal vents causes leaching of basaltic sulfide and reduction of seawater sulfate, which produces sulfide with a mixed sulfur isotopic ratio from those two sources. The two component mixing model shown in Figure 6.1 is based on the mass balance equation between the isotopic composition of the two endmembers MORB-derived sulfide and seawater derived sulfide (Ono et al., 2007). The endmember isotopic compositions for the basalt-derived sulfur are defined here to have a $\delta^{34}S$ value of -0,91‰ and the $\Delta^{33}S$ value is defined to be $\Delta^{33}S = 0$‰ after Ono et al., 2007 and Labidi et al., 2012. The seawater sulfate endmember is characterized by a $\delta^{34}S$ value of 21,5‰ and a $\Delta^{33}S$ value of -0,008‰, defined according to the linear definition of $\Delta^{33}S$ by Ono et al. (2007), see Results. The sulfur isotopic composition of sulfide can also be affected by isotopic exchange between dissolved sulfate and sulfide. This can occur when hydrothermal fluids flow up through the anhydrite bearing zone and equilibrate with sulfate dissolved from anhydrite (Ohmoto et al., 1983). This anhydrite buffer model is also shown in Figure 6.1 and it is based on the temperature-dependent equilibrium fractionation factor of sulfate (SO_4) and sulfide (H_2S) and an isotopic composition of anhydrite that is the same as seawater. The temperatures represent at what temperatures isotopic exchange between sulfate and sulfide happened. These isotopic exchange processes will control the $\delta^{34}S$ and Δ33S values of sulfide through the upflow anhydrite bearing zone as it brings the multiple isotope composition of H_2S towards the anhydrite buffer curve. When equilibrium is established, the isotopic composition of H_2S will fall on the curve of the anhydrite buffer model on the temperature at which equilibrium was established (Ono et al., 2007).

Based on the multiple sulfur isotopic composition measured in hydrothermal sulfide, Figure 6.1 can be used to identify the extent to which sulfide has been generated by sulfate reduction (two-component mixing model) and equilibrated with anhydrite derived sulfate (anhydrite buffer model). Samples that plot onto the two component mixing line originate from mixing of sulfide

from basalt leaching and sulfate reduction. On the other hand, samples that plot onto the anhydrite buffer curve reflect complete isotopic exchange between sulfate and sulfide. Any samples that plot in between the two models is a product of both mixing and subsequent isotope exchange during upflow (Ono et al., 2007). The temperature at which this isotopic exchange occurred can be derived from the intersection of a linear regression line through the data points and the curve representing the anhydrite buffer model. Similarly, the intersection of this regression line with the two-component mixing line defines the contribution of sulfate from thermochemical sulfate reduction and the isotopic composition of H_2S in the reaction zone.

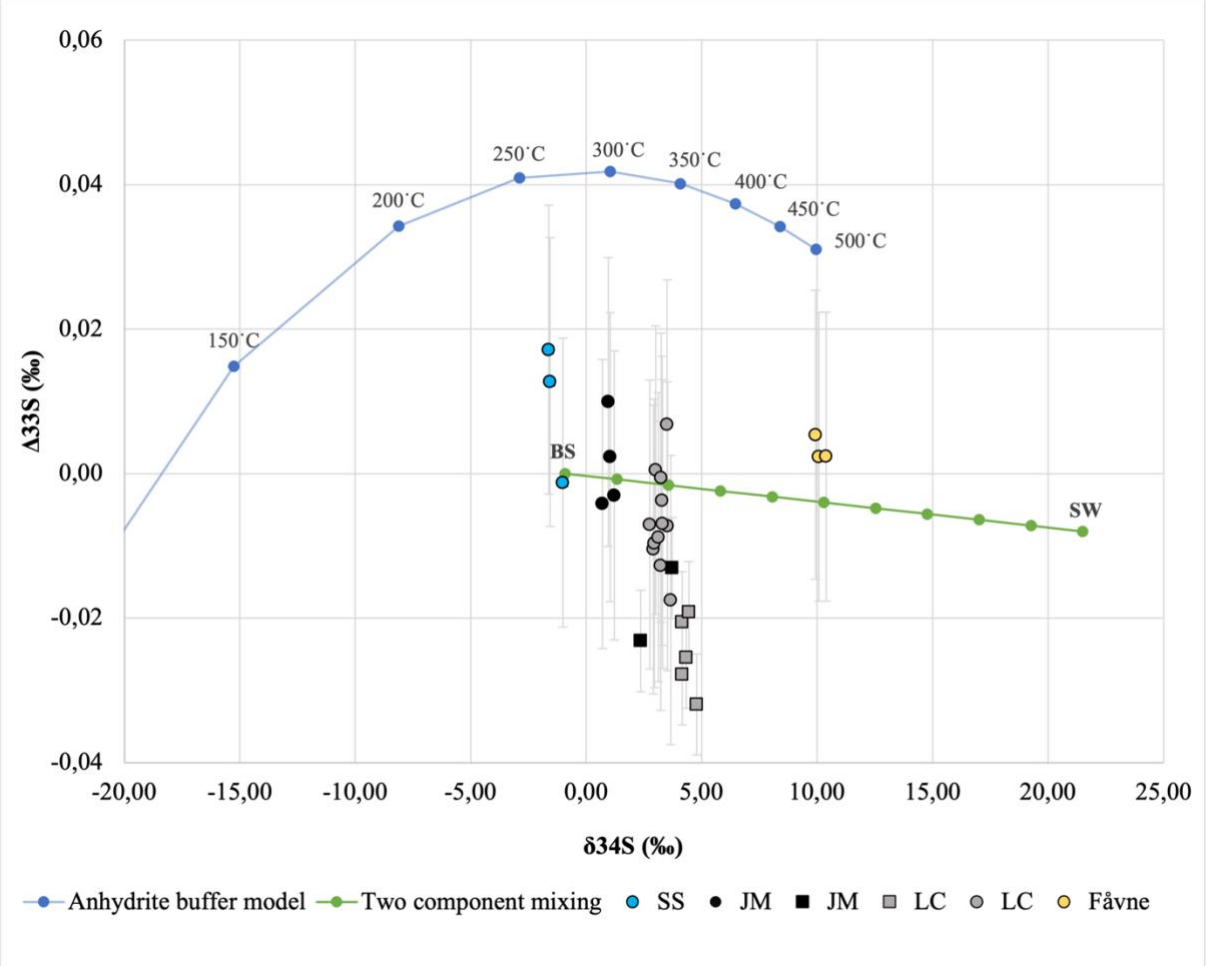

Figure 6.1: Plot of $\delta^{34}S$ vs $\Delta^{33}S$ showing all hydrothermal chimney and fluid samples in the two stage model. Error bars represents 2σ, errors for $\delta^{34}S$ are approximately equivalent to the size of the symbols. Round symbols represent chimney sulfides, square symbols represent H_2S in venting fluids. Temperatures on the anhydrite buffer model represent isotope equilibrium temperatures and the curve represent expected isotopic composition of H_2S that has fully equilibrated with seawater SO_4. The two component mixing model line represent expected isotopic composition of H_2S from mixing between basalt (BS) and seawater derived sulfide (SW). Points on the two component mixing model represents mixing ratios in one-tenth increments (Ono et al., 2007). SS = Seven Sisters, JM = Jan Mayen vent field (Soria Moria), LC = Loki's Caslte.

The next section will use the model outlined above to discuss the origin of sulfide in four vent fields at the Arctic Mid Ocean Ridges, based on multiple sulfur isotope ratios measured in sulfide from chimney and high temperature fluid samples.

6.2 Seven Sisters vent field

The Seven Sisters vent field is not hosted in basalt but rather in mafic volcaniclastic lithologies (Marques et al., 2020). Since these two rock types are of mafic type and therefore have a similar chemical composition, the assumption is made that the sulfide leaching from the host rocks at Seven Sisters will have the same sulfur isotopic composition as sulfide that is leached from MORB.

Isotopic exchange

Sulfides from the Hodr pinnacle (126°C) have slightly positive $\Delta^{33}S$ values that plot in between the anhydrite buffer curve and the two component mixing line (Figure 6.2). This suggest that isotopic exchange between SO_4 and H_2S was incomplete, and the distance from the anhydrite buffer model curve indicates isotopic exchange far away from reaching equilibrium. Similarly, the sulfur isotope data for sulfides from the Lily mound (190°C) display slightly negative values of $\Delta^{33}S$ and plots far away from the equilibration line and within analytical error ($2\sigma = 0{,}02‰$) on the two component mixing line. This suggests that isotopic composition of sulfides from the Lily mound only represent mixing between basalt-sulfide and seawater sulfide, and that no isotopic equilibration occurred.

The regression line of Seven Sisters sulfides intersects the anhydrite buffer model slightly above 250 °C (Figure 6.2). This is a significantly higher temperature than the measured temperature of Hodr pinnacle of 126°C, indicating that the incomplete isotopic exchange is happening subseafloor. The Seven Sisters vent field is situated in very shallow water depths of about 130 m (Marques et al., 2020), which is much shallower than most higher temperature vent fields along mid ocean ridges that typically occur at 2000-3000m depth (Hannington et al., 2005). The shallow depth will limit the temperatures of the vent fluids because the pressure in the reaction and up flow zone will be lower than in hydrothermal systems located at deeper depths. This is caused by the temperature-pressure relationship on the two phase curve of seawater (Hannington et al., 2005). Based on the sulfur isotope data, the incomplete isotopic exchange between SO_4 and H_2S at Hodr happened at about 250°C, indicating a depth of 400 m below sea level (Hannington et al., 2005). The distance from the anhydrite buffer model curve indicates isotopic exchange far away from reaching equilibrium. Experimental work shows that at

temperatures of 250 °C and a pH between 4 and 7, it would take about 4,4 years for SO_4 and H_2S to reach 90% exchange for a total sulfur concentration of 10^{-2} m (Ohmoto and Lasaga, 1982). As the sulfides have not even reached the halfway point of equilibrium, it indicates a much shorter residence time for the fluids in the anhydrite-bearing up flow zone.

Thermochemical sulfate reduction

The regression line intersects the two component mixing line at the basalt endmember, indicating that the isotopic composition of H_2S in the deep reaction zone is 100% sulfide derived from mid ocean ridge basalt and 0% sulfide from thermochemical reduction of seawater sulfate (Figure 6.2). As outlined above, the depth of Seven Sisters vent field limits the fluid temperatures, which limits the rate of thermochemical sulfate reduction (Shanks et al., 1981, Hannington et al., 2005) The Seven Sisters vent field is hosted in mafic volcaniclastic lithologies which have a similar composition to basalt (Marques et al., 2020). The most important reducing agent with the highest reducing capacity in basalt is fayalite, and there is a sufficient amount of fayalite in basalt for sulfate reduction to happen (Shanks et al., 1981). An experimental study shows that thermochemical sulfate reduction by fayalite does produce detectable amounts of H_2S in fluids after 15 days at 250°C in acidic solution, but it is significantly slower than thermochemical sulfate reduction at higher temperatures i.e. sulfide was produced in less than 3 days at 350°C (Shanks et al., 1981). An alternative explanation for the absence of sulfide from thermochemical sulfate reduction could be the lack of sulfate in the reaction zone, although previous work has suggested that there is typically a small amount (> 1mmol/kg) of sulfate in the hydrothermal fluids in the reaction zone (Ono et al., 2007). This suggests that either the residences time in the reaction zone of the Seven Sisters vent field is too short compared to the time required for sulfate reduction to occur at ~250°C, or the sulfate content in the fluids is too low to have a significant impact on the isotopic composition of sulfide.

An important difference between slow and fast spreading ridges is the more variable and lower magma supply at slower spreading ridges. This can cause long periods where amagmatic tectonic extension is the dominating process of spreading, resulting in a wider active faulting zone that can be up to 50 km wide (LaFemina, 2015, Hannington et al., 2005). Sulfides with lower $\delta^{34}S$ values have been found in the high temperature deep (~3000m depth) Snake Pit and The Broken Spur hydrothermal fields at 23°22'N and 29°10'N on the slow-spreading Mid Atlantic Ridge (Snake Pit sulfides $\delta^{34}S$ values of 1,2 – 2,8‰ The Broken Spur $\delta^{34}S$ values of -0,2 – 2,4‰) (Kase et al., 1990, Duckworth et al., 1995). The low values have been suggested

to be caused by a smaller contribution of seawater sulfate, resulting from tectonic structures that can restrict the path of the fluids through the crust. Consequently, there will be fewer fluid-rock interactions which prevent seawater sulfate to contribute to the isotopic composition of sulfides (Duckworth et al., 1995, Kase et al., 1990). The Seven Sisters vent filed is located in close proximity to fractures in the crust (Marques et al., 2020). It is possible that the very low contribution of seawater sulfate to the isotopic composition of deep H_2S is a result of hydrothermal fluids that are restricted by tectonic structures similar to that of Snake Pit and the Broken Spur. In addition, crust that is undergoing rifting caused by the tectonic extension can have increased permeability due to deep faults and fractures (Pedersen et al. 2010b). It is possible that the tectonic structures (faults) lead to a shorter residence time of the fluids as they can help them flow readily through the crust both on their way down to the reaction zone and on their way up to the surface.

Input of magmatic sulfur

Another explanation for the minimal contribution of seawater sulfate to the composition of deep H_2S is the contribution of sulfide with low $\delta^{34}S$ values from an additional source of sulfur. There is extensive volcanism in the area where Seven Sisters is located, and the vent field is related to the Eggvin bank (Marques et al., 2020). This suggests a high magma supply, consistent with the composition of hydrothermal fluids that suggests degassing of volatiles from magmas (Marques et al., 2020). The main sulfur species that are released from silicate melts are H_2S and SO_2, and in a mid ocean ridge setting they have approximately the same isotopic composition as MORB (Herzig et al., 1998). This means that the input of magmatic volatiles could contribute to lower values $\delta^{34}S$ and potentially dilute any higher $\delta^{34}S$ values that could have resulted from seawater sulfate reduction.

Assessing the contribution of magmatic sulfur species to hydrothermal sulfide is difficult due to their similar isotopic composition to basalt-sulfide. However, if SO_2 is released from a magma and cools down to below 300-400°C, disproportionation will happen and cause a kinetic isotope effect that is possible to detect in the isotopic composition of sulfides (Herzig et al., 1998) (McDermott et al., 2015). Previously studied hydrothermal systems with negative $\delta^{34}S$ values affected by SO_2 disproportionation are located in back arc- spreading centers: the Hine Hina field at the Lau back-arc basin and Satanic Mills at PACMANUS back arc vent and SuSu Knolls at Eastern Manus basin (Herzig et al., 1998, McDermott et al., 2015). Based on its geological setting, alteration mineralogy and some fluid geochemistry, the Seven Sisters vent field is suggested to have some similarities with back arc hydrothermal systems (Marques et

al., 2020). Therefore, incorporation of sulfide from disproportionation of SO_2 has previously been suggested by Marques et al. (2020) to explain the isotopic composition of sulfides from the Seven Sisters chimneys. Measured sulfide $\delta^{34}S$ values for Hodr pinnacle are slightly lower than the $\delta^{34}S$ range of previously measured values for sediment-free hydrothermal systems of -0,8 to 6,38‰ (Herzig et al., 1998). The possibility of the more negative values being a result from SO_2 disproportionation altering the sulfur isotopic composition is therefore investigated using a model by McDermott et al. (2015) (Figure 6.3). The meshed fields in Figure 6.3 are the temperature dependent equilibrium multiple sulfur isotopic composition of H_2S and SO_4 during disproportionation of SO_2 (Figure 6.3). Sulfides that plot on or close to these meshed fields are interpreted to have an isotopic composition that has been significantly influenced by disproportionation of magmatic SO_2 (McDermott et al., 2015). However, the sulfides from Seven Sisters do not plot in the meshed fields suggesting that the slightly more negative $\delta^{34}S$ sulfide values from Hodr pinnacle are due to incomplete isotopic exchange between seawater SO_4 and H_2S, and do not result from SO_2 disproportionation (Figure 6.3). Magmas in basalt-hosted mid ocean ridge systems are less silicic and oxidizing compared to those influencing back-arc hydrothermal systems, leading to less SO_2 degassing into the hydrothermal system (McDermott et al., 2015). This could explain the lack of SO_2 disproportionation affecting the sulfur isotopic composition of chimney sulfides from the Seven Sisters vent field.

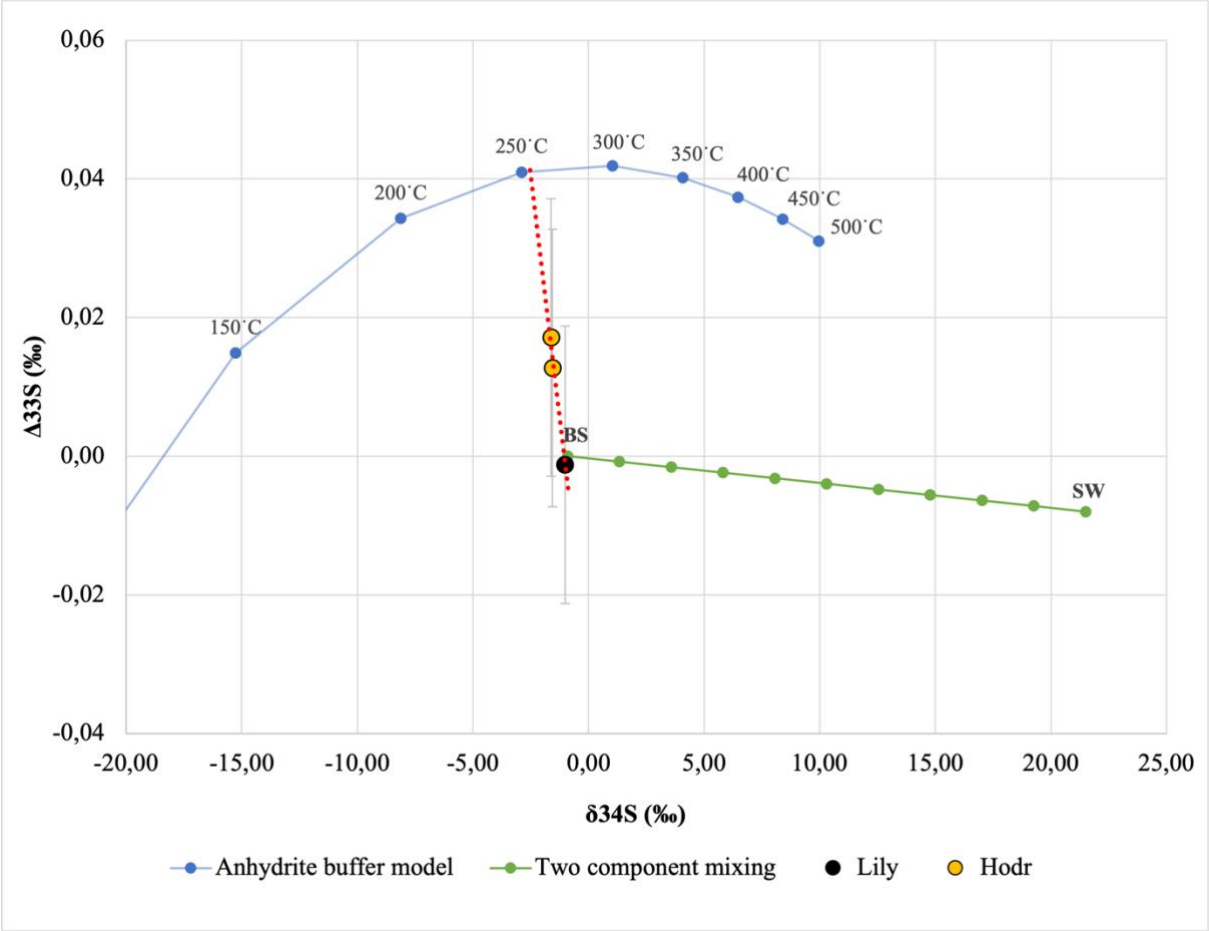

Figure 6.2: Plot of $\delta^{34}S$ vs $\Delta^{33}S$ of Seven Sisters chimney sulfides in two staged model. Dotted red line is linear regression line for the data points.

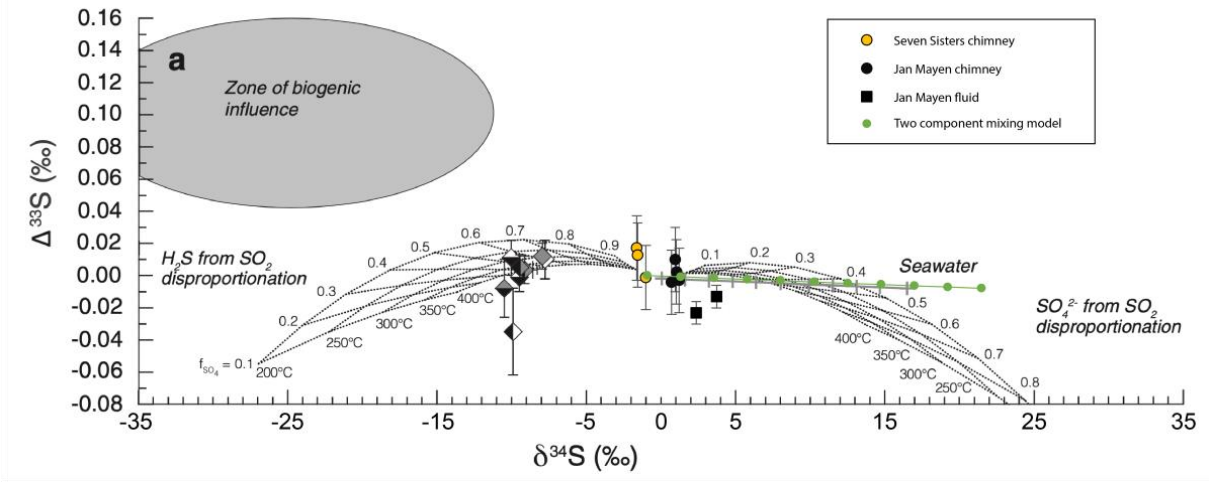

Figure 6.3: Modified from McDermott et al. (2015) showing plot of $\delta^{34}S$ vs $\Delta^{33}S$ for Seven Sister and Soria Moria (Jan Mayen) sulfides. Meshed fields represent the expected equilibrium sulfur isotope composition of H_2S and SO_4 from disproportionated SO_2 (McDermott et al., 2015). The Meshed fields are moved laterally relative to McDermott et al., 2015 due the difference in host rock isotopic composition where island arc volcanic rocks have 5‰ higher $\delta^{34}S$ values compared to mid ocean ridge basalt. The diamond shaped symbols should be ignored. Green line is the two component mixing model.

6.3 Soria Moria vent field (Jan Mayen vent fields)

Figure 6.4 shows that most of the sulfide samples from the Soria Moria (279°C) and Lilleputt (255°C) chimneys at the Soria Moria vent field plot within analytical error on the two-component mixing model line. However, the fluid sulfide data were measured with a smaller analytical uncertainty ($2\sigma = 0{,}007‰$), and plot well below the two component mixing line.

Isotopic exchange

The isotopic composition of chimney sulfides is interpreted using the two staged model. A linear regression line defined by the $\delta^{34}S$ and $\Delta^{33}S$ data intersects the anhydrite buffer model at about 270°C (Figure 6.4). The measured temperatures for the Lilleputt chimney and Soria Moria chimney are 255°C and 279°C, respectively. The temperature for exchange therefore agrees with the measured temperatures and suggests that isotopic exchange is happening slightly below or within the chimneys. Similarly, to the Seven Sisters sulfides, the Soria Moria sulfides plot a great distance away from the anhydrite buffer model, indicating that isotopic exchange between SO_4 and H_2S did not reach equilibrium. This suggests a short residence time of the fluids in the anhydrite bearing up flow zone. The Soria Moria vent field is related to a small fault basin suggested to control the venting (Pedersen et al., 2010b). It is possible that this fault has the effect of letting the fluids readily flow through the crust, causing them to have a short residence time.

Thermochemical sulfate reduction

The intersection of the regression line through the Soria Moria data points with the two component mixing line indicates a contribution of 10% seawater derived sulfur to the isotopic composition of H_2S in the deep reaction zone. This is a lower contribution of seawater sulfur than for deep basalt hosted systems along the fast-spreading East Pacific Rise (12-22%), Southern East Pacific Rise (17-27%) and the slow-spreading Mid Atlantic Ridge (25-33%) (Ono et al., 2007, McDermott et al., 2015, Peters et al., 2010). The Soria Moria vent field is located at about 700 m water depth which is significantly deeper than the 130 m deep Seven Sisters vent field, but still shallow compared to the typical 2000-3000m depth of higher temperature vent fields along mid ocean ridges (Hannington et al., 2005, Pedersen et al., 2010b). This suggests that depth is an important constraint on the contribution of seawater sulfate to the isotopic composition of deep H_2S, as the contribution of seawater sulfate is relatively low compared to other deep hydrothermal systems, but higher than the significantly shallower Seven Sisters vent field with a contribution of seawater sulfate of 0%. However, the Jan Mayen Vent fields are a part of the AMOR that has anomalously high magmatic activity due to its close

proximity of the Icelandic and the Jan Mayen hotspot (Johannessen et al., 2017), and the venting fluids from the Jan Mayen vent fields do indicate an influence of magmatic volatiles (Stensland et al., 2019). This suggests that, analogous to the Seven Sisters vent field, it is possible that input of the magmatic volatiles H_2S and SO_2 provides an additional contribution of low $\delta^{34}S$ sulfide that can dilute the contribution of seawater sulfate. However, following the same multiple-sulfur isotope approach as used for the Seven Sisters vent field (Figure 6.3), neither the chimney nor the fluid sulfides plot in the meshed field, indicating that disproportionation of SO_2 does not provide a significant contribution to the sulfur isotopic composition of sulfides from the Soria Moria Vent field. Magmatic SO_2 disproportionation does thus not provide a feasible explanation for the low $\Delta^{33}S$ values in fluids compared to the solid sulfides.

An alternative explanation for the low contribution of seawater sulfate reduction is related to the shallow depth of the Soria Moria vent fields, which limits the temperature in the subsurface and causes relatively sluggish kinetics of seawater sulfate reduction (Shanks et al., 1981, Hannington et al., 2005). In addition, the Soria Moria vent field is suggested to be controlled by a fault (Pedersen et al., 2010b) and tectonic structures have been suggested to cause a smaller contribution of seawater sulfate due to these restricting the path of the fluids through the crust (Duckworth et al., 1995). This may also result in a short residence time of the fluids as the faults would help the fluids flow readily through the crust. This suggestion also agrees with the implication made by Pedersen et al. (2010b) that that the south-western part of the Mohns Ridge, where the Soria Moria vent field is situated, is influenced by a fluctuating magma supply. When there is low magma supply this part of the ridge segment will be at a stage of rifting which can provide increased permeability by new deep faults and fractures (Pedersen et al. 2010b).

Minor S isotopes in fluids

There are limited studies of sulfur isotopes in high temperature hydrothermal systems that include the minor ^{33}S isotope. Therefore, existing knowledge about processes causing variations of this isotope is not sufficient to explain the significantly lower $\Delta^{33}S$ in fluids compared to what is predicted by the two component mixing model, as well as the downward shift in the fluid sulfides compared to the mineral sulfides. A similar downward shift in the fluid sulfides has been measured in the high temperature Comfortless Cove at SMAR hydrothermal fields by Peters et al. (2010) and is attributed to either partial isotopic equilibration between dissolved sulfate and sulfide, or to only some of the reduced seawater sulfate in the reaction zone exchanging isotopes with sulfate when the fluids flow through the anhydrite bearing zone.

This would result in different $\Delta^{33}S$ values as there would be a variation of H_2S affected by isotopic exchange and isotope mixing (Peters et al., 2010). However, the dissolved sulfides measured by Peters et al. (2010) did plot between the anhydrite buffer model and the two-component mixing line and this does therefore not provide an explanation for the Soria Moria and Lilleputt dissolved sulfides plotting significantly below the two component mixing line (taking analytical certainty into account).

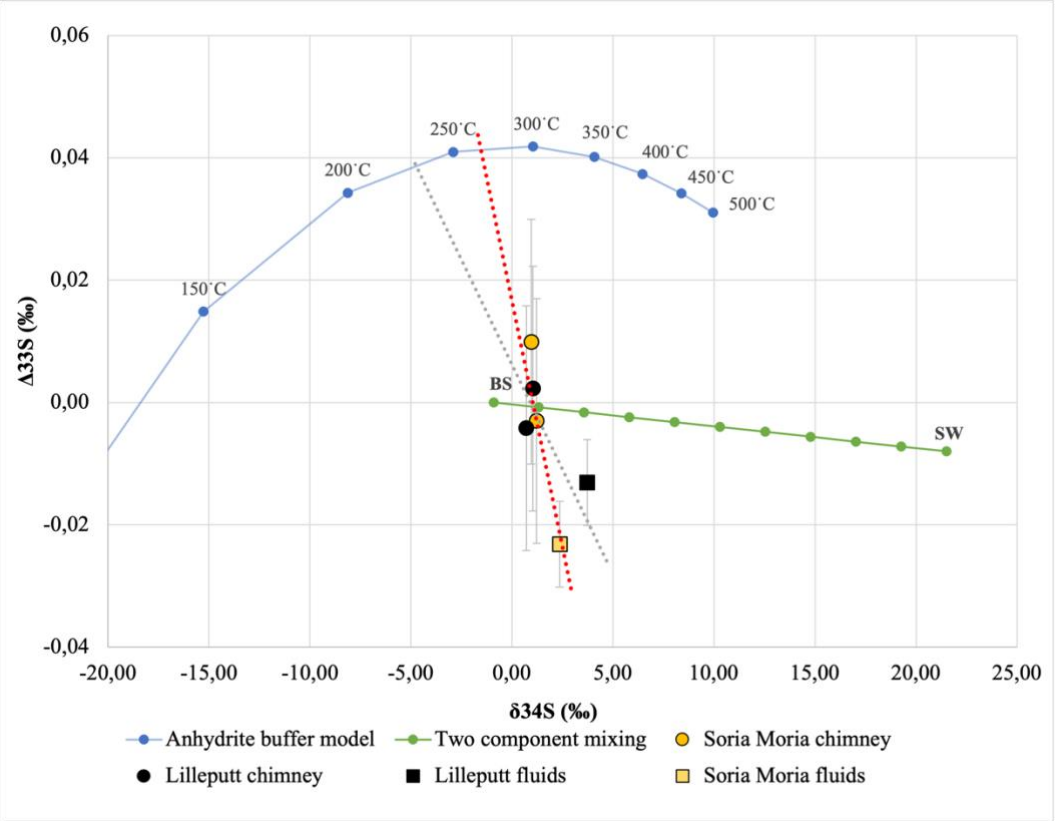

Figure 6.4: Plot of $\delta^{34}S$ vs $\Delta^{33}S$ of chimney and vent H_2S from Soria Moria vent field in two staged model. Dotted red line is modified regression line to better fit majority of sulfide samples, used for interpretations. Dotted grey line is the regression line when all data points are included, not used for interpretations.

6.4 Fåvne vent field

The two staged model of Fåvne vent is limited to the North Tower chimney (265°C) because the South Tower chimney contained insufficient sulfide for analysis.

Isotopic exchange

The two staged model of the North Tower chimney sulfides suggest incomplete isotopic exchange between SO_4 and H_2S at very high temperatures of 450°C (Figure 6.5). This is

significantly higher than the measured temperature of 265°C. For the fluids to reach such high temperatures it implies that the isotope exchange is happening at great depths in the crust due to the two phase boundary for seawater putting constraints on temperatures (Hannington et al., 2005). Also, Fåvne is located along the central Mohns Ridge where there is low magma supply, which will typically mean the heat sources would be deep (Pedersen et al., 2010b, Hannington et al., 2005). The central Mohns Ridge has a morphology typical for that of an ultra-slow spreading ridge, with a well-developed rift valley bounded by steep faults that can allow the hydrothermal circulation to penetrate to great depths from 5-8 km into the crust. (Pedersen et al., 2010b, Hannington et al., 2005). This provides a potential explanation for the high temperature and inferred from this the high depth of the reaction zone at Fåvne. Interestingly, the high temperature inferred from the anhydrite buffer model agrees with previous temperature estimates at Fåvne vent field by (Boonnawa et al., in prep), where the empirical Fe/Mn geothermometer was used to predict a temperature of the Fåvne reaction zone in the vicinity of ~470°C.

The North Tower sulfides plot in between the anhydrite buffer model and the two-component mixing model, but closer to the mixing model (Figure 6.5). This suggests that equilibration between dissolved sulfate and sulfide in the upflow zone was far away from reaching equilibrium. Experimental work indicates that at temperatures of 400°C and a pH between 3 and 4, it would take about 14-70 hours for SO_4 and H_2S to reach 90% exchange for a total sulfur concentration of 10 mm/kg (Ohmoto and Lasaga, 1982). Since the temperatures for isotope exchange in the Fåvne fluids is higher than 400°C, even faster exchange rates could be expected. The fact that the Fåvne sulfides do not even plot on the halfway point of reaching equilibrium implies a very short residence time for the fluids, that is significantly less than 70 hours. The Fåvne vent field is located near a major detachment fault and like the Soria Moria vent field is suggested to be fault controlled (Brekke et al., 2021, Boonnawa et al., in prep) and deep faults can lead to an increased permeability of the crust (Pedersen et al., 2010b). This further supports the suggestion of the tectonic structures allowing for fluids to readily flow through the crust, leading to a short residence time preventing isotope exchange between dissolved sulfate and sulfide in the anhydrite bearing zone to reach equilibrium.

Thermochemical sulfate reduction

The sulfides from Fåvne vent field stand out from the three other AMOR vent fields due to the significantly higher $\delta^{34}S$ values of 9,93-10,07 ± 0,09‰ (2σ, n=9) (Figure 6.1). The regression line of the North Tower chimney sulfides intersects the middle point of the two-component

mixing model. This implies that the high $\delta^{34}S$ values are a result of a high contribution of 50% seawater sulfate to the isotopic composition of H_2S in the deep reaction zone (Figure 6.5). This is much higher than what has been found in previous multiple isotope studies of basalt hosted systems, where the contribution of seawater sulfate along the fast spreading East Pacific Rise is 12-22% and Southern East Pacific Rise is 17-27% and the slow spreading Mid-Atlantic Ridge is 25-33% (Ono et al., 2007, McDermott et al., 2015, Peters et al., 2010).

The high 50% contribution of seawater sulfate could potentially be a result of the slow spreading Mohns Ridge having a very deep-seated heat source, which is typical for slow-spreading ridges (Pedersen et al., 2010b, Hannington et al 2005). A deeper-seated heat source in combination with high temperatures in the reaction zone (~450°C) can allow for a higher degree of sulfate reduction, due to an increased pathway of circulating fluids that would allow fluids to have a longer residence time in the oceanic crust. Consequently, more seawater can react at higher temperatures with ferrous bearing minerals and giving it more time to be reduced (Peters et al., 2010). This has been implied through a multiple isotope approach to cause a higher contribution of up to 33% of seawater sulfate to the isotopic composition of sulfide minerals in the basalt hosted SMAR field located along the slow spreading Mid-Atlantic Ridge, leading to $\delta^{34}S$ values with an upper limit of 8,9‰ (Peters et al., 2010). However the two staged model suggests an even higher contribution of seawater sulfate, suggesting that a longer residence time of the fluids in the reaction zone might not fully explain the higher contribution of seawater sulfate at Fåvne. In addition, similar to the Soria Moria and Seven Sisters vent fields, the Fåvne vent field is suggested to be fault controlled (Brekke et al., 2021, Boonnawa et al., in prep). Since tectonic structures controlling vent fluids have previously been found to result in relatively small contribution of seawater sulfate either due to lower fluid rock interactions (Duckworth et al., 1995) or due to allowing fluids to flow readily through the crust an alternative explanation is needed.

An alternative explanation for the origin of high $\delta^{34}S$ values in sulfides at Fåvne involves the nature of the host rocks in the subsurface of this vent field. Boonnawa et al. (in prep) and Brekke et al. (2021) observed rocks of mafic composition (gabbroic rock) on the seafloor surrounding the hydrothermal vents at Fåvne, but geochemical data from the vent fluids at Fåvne clearly indicate an influence from ultramafic rocks at depth (Boonnawa et al., in prep). The ultramafic hosted Logatchev and Rainbow fields located along the Mid Atlantic Ridge have been reported to have sulfides with higher $\delta^{34}S$ values compared to basalt hosted vent fields (Hannington et al., 2005). The $\delta^{34}S$ values of Fåvne fall in the range of $\delta^{34}S$ values reported for these ultramafic

hosted systems (with an upper limit of $\delta^{34}S$ = 13‰ at the Rainbow field and $\delta^{34}S$ = 14‰ at Logatchev field) (Hannington et al., 2005). These high values have been explained previously by a higher contribution of reduced seawater sulfate due to hydrothermal fluids circulating through serpentinizing ultramafic rocks (Hannington et al., 2005). The process of serpentinization generates a large amount of H_2 through the oxidation of ferrous iron in olivine. This causes a very reducing environment which supports a high rate of seawater sulfate reduction to H_2S (Hannington et al., 2005). A high contribution of seawater sulfate reduction also requires sufficient amounts sulfate in the fluids (Shanks et al., 1981). Lein et al. (2001) has implied that constant entrainment of seawater into the hydrothermal circulation of the ultramafic hosted Rainbow field has led to sulfides with a heavy isotopic composition with a mean $\delta^{34}S$ value of 10‰. Since the Fåvne sulfides indicate a 50% contribution of seawater sulfate to the isotopic composition of deep H_2S, there must be a significant amount of sulfate available for reduction. It is plausible that the major detachment fault suggested to control the Fåvne vent field could allow for constant entrainment of seawater in to the deep reaction zone, followed by its precipitation as anhydrite, which can then be reduced. The high temperatures here (~450°C) and very reducing conditions generated by serpentinization allow for fast kinetics of seawater sulfate reduction (Shanks et al., 1981). Together this a plausible explanation for a high contribution of seawater-like sulfate and high $\delta^{34}S$ values in chimney sulfides from the Fåvne vent field.

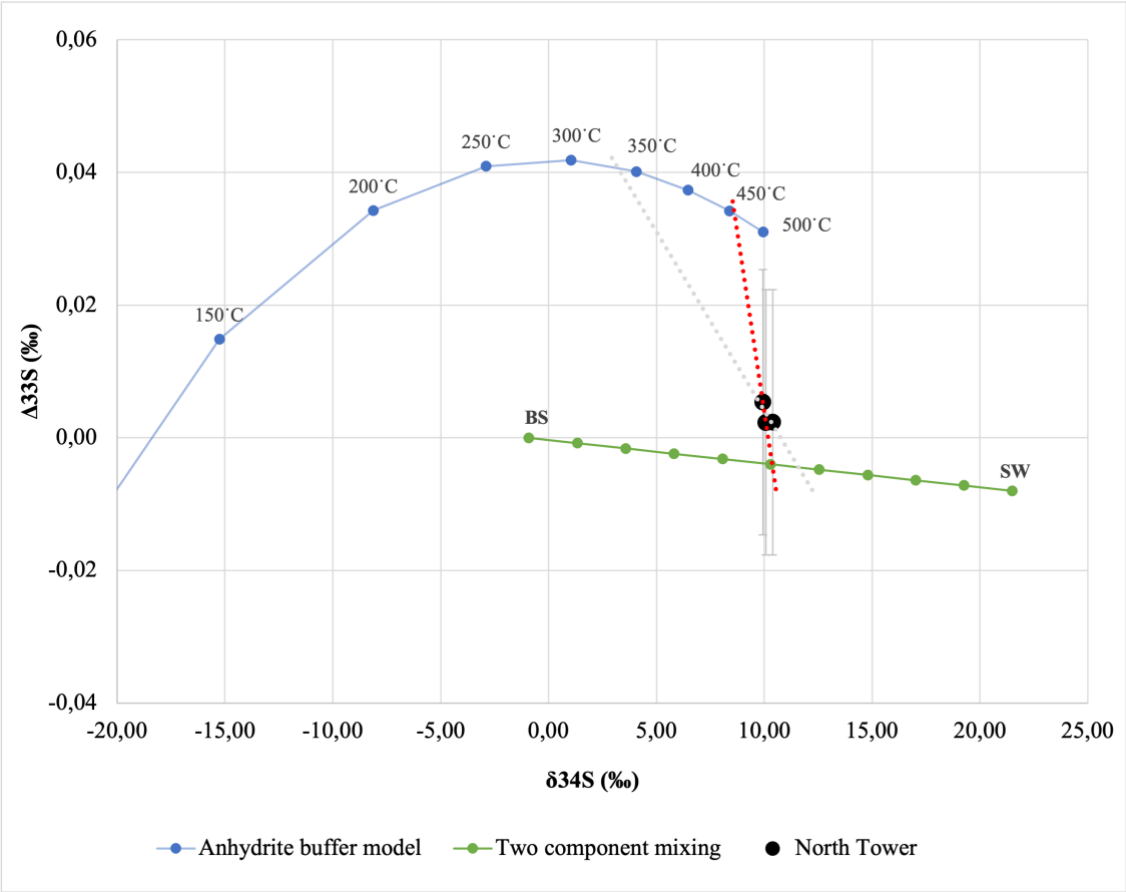

Figure 6.5: Plot of $\delta^{34}S$ vs $\Delta^{33}S$ of chimney sulfides from Fåvne vent field in two staged model. Dotted red line is modified regression line to better represent sulfide samples. Dotted grey line is the linear regression line when all data points are included, not used for interpretation.

6.5 Loki's Castle vent field

The majority of mineral and fluid sulfides from all the four chimneys (Joao, Menorah, Camel, Sleepy) at Loki's Castle does not plot in between the anhydrite buffer model and the two component mixing model, but rather below the two component mixing model (Figure 6.6a). All chimneys show highly similar isotopic composition of sulfides, this is consistent with previous geochemical studies of the high temperature fluids at Loki's Castle indicating a single source fluid (Baumberger et al., 2016b, Viflot, 2019). This implies that one sulfur source with negative $\Delta^{33}S$, lower than seawater and basalt-derived sulfur, has a significant influence on the isotopic composition of sulfides in the Loki's Castle high temperature chimneys. A possible explanation for this low $\Delta^{33}S$ sulfur source can be found in the low-temperature barite field that occurs nearby the sulfide mound hosting the Joao chimney (Baumberger et al., 2016b, Eickmann et al., 2020). Barite from this low temperature field displays higher $\delta^{34}S$ values (+22,2 to +36,1‰) and lower $\Delta^{33}S$ (-0,031 to -0,159‰) values than surrounding seawater sulfate ($\delta^{34}S$ =21,3 and $\Delta^{33}S$ =-0,040‰) (Eickmann et al., 2014). The isotopic composition of these barites

is implied to be a result of barites precipitating from residual sulfate after microbial sulfate reduction (Eickmann et al., 2014). Eickmann et al., 2014 suggests that a zone of microbial sulfate reduction fueled by H_2 and CH_4-rich hydrothermal fluids mixed with cold seawater in the subsurface creates a residual sulfate pool below the low temperature field in the sulfide mound. Interactions between the high-temperature fluids and such a sulfate pool, for example barite with a similar isotopic composition as the barite field chimneys that has been buried over time, may explain the isotopic compositions measured in the chimney sulfides.

Barite buffer model

To test the model above, a modified two staged model is made where the two component mixing line remains and the anhydrite buffer model is exchanged with a "barite buffer model". This barite buffer model is based on similar isotope exchange processes between H_2S and SO_4 as in the anhydrite buffer model, but the isotopic composition of the sulfate is derived from barites with higher $\delta^{34}S$ and lower $\Delta^{33}S$ than seawater sulfate (Figure 6.6b). The mean values of the barites measured by Eickmann et al. (2014) ($\delta^{34}S$ = 28,92‰, $\Delta^{33}S$ = -0,197‰) were used to produce the modified barite buffer model.

The isotopic compositions of fluid and mineral sulfides plot in between the two component mixing line and the barite buffer model curve, and the modified two staged model is therefore used to interpret the isotopic composition in sulfides from the Loki's Castle vent field. This is done in the same manner as the two staged model with anhydrite buffer model. However, it is important to note that the alternative model has some limitations. Firstly, the distance between the sulfides and the barite buffer curve, which is taken as a measure of the degree of equilibration, is dependent on the isotopic composition chosen for the SO_4^{2-} in barites. The assumed isotopic composition is the average of all measured values from Eickmann et al. (2014), however it is not certain that this is an accurate representation for the potential barite deposits precent in the subsurface of Loki's Castle vent field. Secondly, barite may behave differently than anhydrite in the hydrothermal circulation as it is far less soluble than anhydrite (Hanor, 2000). This could mean that barite interacting with hydrothermal fluids does not dissolve in the fluids, which would prevent H_2S from equilibrating with dissolved sulfate derived from barite. However, theoretical calculations by Kritsotakis and Von Platen (1980) suggest that barite could become soluble in temperatures higher than 200°C and at low pH through reaction with reducing agents such as CH_4, H_2, NH_3 (Hanor, 2000, Roerdink et al., 2012). The endmember fluid compositions of Loki´s Castle have been found to have high concentrations of CH_4 and H_2 compared to bare-rock systems, which is caused by Loki's Castle

fluids being influenced by sediments that contain organic matter (Baumberger et al., 2016b). Furthermore, Eickmann et al. (2014) suggested that remobilization of subsurface barite contributes to the sulfur isotopic composition of barites in the low temperature barite field, as well as in the enrichment of fluids in Ba. Based on this, it is therefore assumed that the buried barite dissolves sufficiently to isotopically exchange with the dissolved sulfide.

Isotopic exchange

According to the barite buffer model, the temperature of isotope exchange is 350°C which is higher than the measured temperature of 299-316°C in the chimneys, suggesting that isotopic exchange happens in the subsurface below the chimneys (Figure 6.6b). This relatively high temperature allows for rapid kinetics of isotope exchange (Ohmoto and Lasaga, 1982). Despite this, the sulfide in fluids and minerals plot at a great distance from the barite buffer model, indicating isotopic exchange between dissolved sulfide and sulfate did not reach equilibrium. Similarly, to the other three AMOR vent fields, this suggests a short residence time for the fluids in the upflow zone. A plausible explanation is that the venting at Loki's Castle occurs above two normal faults (Pedersen et al., 2010a) .This could make the crust more permeable and help the fluids flow readily through the crust (Pedersen et al., 2010b).

Furthermore, there is linear trend between $\delta^{34}S$ and $\Delta^{33}S$ in dissolved and mineral sulfides, and a shift towards lower $\Delta^{33}S$ and higher $\delta^{34}S$ in fluid sulfides compared to mineral sulfides. This can potentially be explained by previously mentioned implications by Peters et al. 2010. They suggested this shift to result from either incomplete isotopic exchange between H_2S and SO_4, or that only some of the reduced seawater sulfate in the reaction zone exchange isotopes with sulfate as the fluids flow through the anhydrite (barite) bearing zone. However, further research is on the ^{33}S isotope is needed to reach a conclusion as existing knowledge about processes causing variations of this minor isotope in hydrothermal settings is limited.

The regression line intersects the two staged mixing line at a little less than 20% sulfide derived from seawater sulfate and more than 80% sulfide derived from basalt (Figure 6.6b). This compares to 12-22% and 17-27% contribution of seawater-derived sulfate to sulfides in mid-ocean ridge hydrothermal systems located along the fast spreading East Pacific Rise and Southern East Pacific Rise (Ono et al., 2007, McDermott et al., 2015), and is lower than the 25-33% contribution of seawater-derived sulfate of hydrothermal fields located along the slow spreading Mid-Atlantic Ridge (Ono et al., 2007, Peters et al., 2010).

Since the fluids reach temperatures of at least 350°C, which allows for rapid kinetics of seawater sulfate reduction (Shanks et al., 1981), and the Loki's Castle vent field is located at 2400m water depth, the lower contribution of seawater sulfate compared to slow spreading ridges cannot be explained by lower temperatures and shallower depths, like at the Soria Moria (Jan Mayen) and Seven Sisters vent fields. Instead, this suggests that the Loki's Castle vent fluids have a shorter residence time than that of the hydrothermal systems located along the slow spreading Mid-Atlantic Ridge, where a longer residence time is suggested to be caused by an increased pathway of circulating fluids due to a deeper seated heat source than at fast spreading ridges (Peters et al., 2010). This suggests that despite Loki's Castle being located along the ultra-slow spreading Mohns Ridge, the fluids could have a short pathway comparable to that of hydrothermal systems of fast spreading ridges where the heat source typically causes relatively shallow hydrothermal circulation of 1-2 km into the crust (Pedersen et al., 2010b, Ono et al,. 2007, Hannington et al., 2005). A plausible explanation for this could be that the thickness of the crust at the Mohns Ridge is 2-3 km thinner than average oceanic crust, causing a shallower reaction zone (Pedersen et al., 2010a, Hannington et al., 2005). This agrees with previous suggestions by Pedersen et al. (2010a) that fluid compositions of Loki's Castle indicate that water-rock reactions occur around 2 km below the seafloor. Also, the venting at Loki's Castle occurs above two normal faults (Pedersen et al., 2010a). Similarly, to the Seven Sisters and the Soria Moria vent field, these tectonic structures could cause a lower contribution of seawater sulfate either because of lower fluid rock interaction or shorter residence time of fluids.

Input of sediment sulfur

Finally, the Loki's Castle vent field is suggested to be a sediment-influenced hydrothermal system (Baumberger et al., 2016a, Baumberger et al., 2016b). In sedimented-hosted systems, a potential source of sulfur into the hydrothermal systems is dissolution of biogenic sulfides from marine sediments, which typically have significantly negative $\delta^{34}S$ values and positive $\Delta^{33}S$ values that are higher than that of the anhydrite buffer model (Peters et al., 2010, McDermott et al., 2015). A previous multiple sulfur isotope study of sulfides from the sediment covered Guaymas Basin mid ocean ridge hydrothermal system suggests a small contribution of biogenic sulfides affecting the sulfides to have lower limit of $\delta^{34}S$ values of -1,4‰ (McDermott et al., 2015). The lack of negative $\delta^{34}S$ and positive $\Delta^{33}S$ values of sulfides at Loki's Castle indicates no significant incorporation of biogenic sulfides in the fluids. Instead, the sulfur isotopes are indirectly affected by sediments, as the subsurface sediments produce a fluid composition that fuels microbial sulfate reduction (Eickmann et al., 2014). As demonstrated by the barite buffer

model, the residual sulfate from this microbial sulfate reduction has a significant impact on the isotopic composition of the sulfides at Loki's Castle.

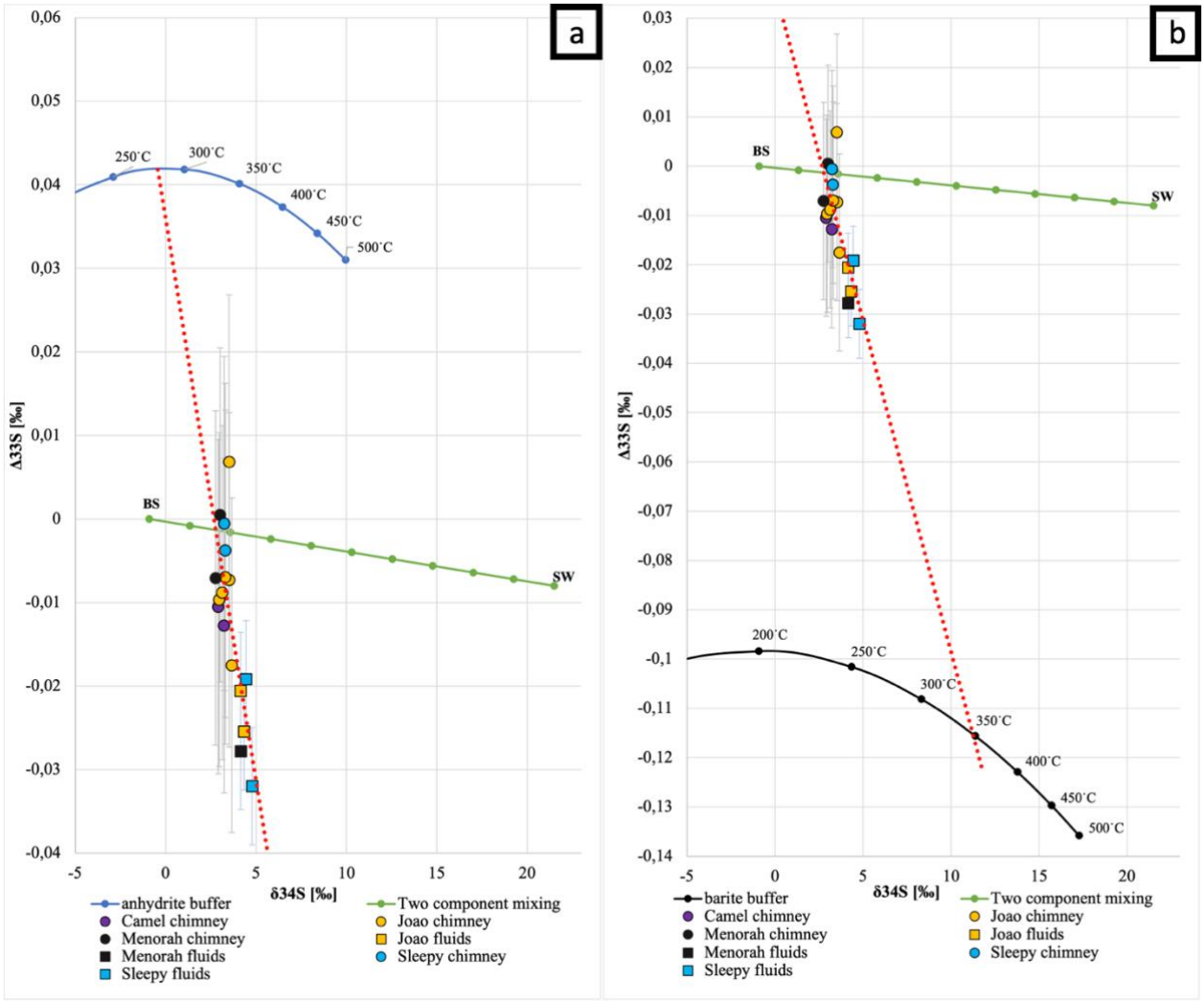

Figure 6.6: Plots of $\delta^{34}S$ vs $\Delta^{33}S$ of chimney sulfide and vent H_2S from Loki's Castle vent field in two staged model. **(a)** Loki's Castle sulfides in two staged model with anhydrite buffer model. **(b)** Loki's Castle sulfides in modified two staged model with barite buffer model.

CHAPTER 7: SUMMARY AND CONCLUSIONS

This thesis demonstrates that variations in the geological setting of four hydrothermal vent fields along the Arctic Mid Ocean Ridge are reflected in the multiple sulfur isotope ratios of high-temperature hydrothermal fluids and sulfide minerals. Below is a summary of the main findings.

- The combined $\delta^{34}S$ and $\Delta^{33}S$ data demonstrate a variation in reaction zone temperatures for the four investigated AMOR vent fields, that appears to be correlated to vent field depth. The lowest temperature for isotopic exchange (250°C) was found at the shallow (130 m water depth) Seven Sisters vent field. A higher temperature of isotopic exchange (270°C) was observed for the Soria Moria vent field (700 m water depth), an even higher temperature (350°C) at the deep Loki's Castle vent field (2400 m water depth) and the highest temperature (450°C) at the deep Fåvne vent field (3000 m water depth).
- It is shown by the combined $\delta^{34}S$ and $\Delta^{33}S$ data that there is a difference in contributions from seawater sulfate to the isotopic composition of sulfide between the four investigated AMOR vent fields. This appears to be related to their difference in reaction zone temperature, because there is an increase in the contribution of sulfate reduction as the temperature in the reaction zone increases. The lowest contribution of seawater sulfate (0%) was found at the Seven Sisters vent, which has the lowest reaction zone temperature (250°C). A higher contribution of seawater sulfate (10%) was observed for the Soria Moria vent field (270°C), and an even higher seawater contribution (20%) at the Loki's Castle vent field (350°C). The highest contribution of seawater sulfate (50%) was found at the Fåvne vent field, corresponding to the highest reaction zone temperature (450°C) of all studied AMOR vent fields.
- The multiple sulfur isotopes in sulfides from the four AMOR vent fields indicate that the rock type that the fluids interact with has a significant influence on subsurface sulfur cycling, as suggested by the significantly higher contribution of seawater sulfate to the isotopic composition of sulfides from the ultramafic influenced Fåvne vent field, compared to the three other vent fields hosted in mafic lithologies.

- The two vent fields along the AMOR that have been argued to be magmatically-influenced are Soria Moria and Seven Sisters, but sulfides from these two vent fields do not have an isotopic composition that reflects disproportionation of magmatic derived SO_2. However, it is possible that input of magmatic volatiles is affecting the isotopic composition in sulfides by diluting the seawater sulfate contribution to a lower percentage
- The only vent field along the AMOR that has been argued to be influenced by sediments is the Loki's Castle vent field. This is indirectly observed in the multiple isotopic sulfur ratios of sulfides by significantly lower $\Delta^{33}S$ values, which are possibly caused by dissolution of barite containing residual sulfate from microbial sulfate reduction.
- The combined Δ^{33}S and δ^{34}S data indicate that isotope exchange between anhydrite- or barite-derived sulfate and sulfide does not reach equilibrium at the AMOR vent fields, despite at a wide range of subsurface temperatures (250-450°C).

The findings of this study suggest that subsurface sulfur cycling in vent fields at ultra-slow spreading ridges is distinct from that on faster spreading ridges or back-arc basins.

The multiple sulfur isotope values from the AMOR vent fields indicate that isotopic exchange between dissolved sulfate and sulfide in the upflow anhydrite bearing zone does not reach equilibrium, even at very high temperatures (450°C) that would allow for fast kinetics of isotope exchange. In addition, the contribution of seawater sulfate to sulfide is generally low (0-20%) compared to vent fields along fast spreading ridges (12-27%) and slow spreading ridges (25-33%), except for Fåvne vent field. This suggests that hydrothermal systems on ultra-slow spreading ridges are characterized by a lower residence time of fluids through the circulation systems, which may be due to tectonic extension being the dominating process behind spreading. This could lead to a more permeable crust by fractures and faults to the deep, which can allow fluids to flow faster through the crust than on spreading ridges dominated by magmatic processes. Furthermore, fluids interacting with ultramafic rocks can lead to higher contributions of sulfate reduction, and this could be typical for hydrothermal systems on ultra-slow spreading ridges, as their amagmatic accretion processes can lead to exposed mantle rocks. Lastly, the two magmatically influenced vent fields do not show input of sulfide from disproportionation of magmatic derived SO_2. This could indicate that it is not typical to find a significant contribution of disproportionated SO_2, to the sulfur cycle in hydrothermal systems related to ultra-slow spreading ridges, even if the hydrothermal systems are related to hotspots.

CHAPTER 8: FUTURE WORK

- The lower $\Delta^{33}S$ values in sulfide in fluids compared to sulfide in minerals in the Soria Moria (Jan Mayen) vent field cannot be explained and further research is needed.
- The lower $\Delta^{33}S$ values in sulfide in fluids compared to sulfide in minerals in the Loki's Castle vent field can potentially be explained by incomplete isotopic exchange or variation of sulfide affected by mixing and fractionation processes. However, more research is needed to reach a conclusion.
- Study of Pb isotope ratios in sulfides can provide additional information on residence time of the hydrothermal fluids in the crust.
- Study of multiple sulfur isotopes in hydrothermal systems related to other ultra-slow spreading ridges, for example the Southwest Indian Ridge to get further insight into similarities and differences in the sulfur cycling.

REFERENCES

BAKER, E. T., EDMONDS, H. N., MICHAEL, P. J., BACH, W., DICK, H. J., SNOW, J. E., WALKER, S. L., BANERJEE, N. R. & LANGMUIR, C. H. 2004. Hydrothermal venting in magma deserts: The ultraslow-spreading Gakkel and Southwest Indian Ridges. *Geochemistry, Geophysics, Geosystems,* 5.

BARNES, H. L. 1997. *Geochemistry of hydrothermal ore deposits,* New York, John Wiley & Sons.

BAUMBERGER, T., FRÜH-GREEN, G. L., DINI, A., BOSCHI, C., VAN ZUILEN, K., THORSETH, I. H. & PEDERSEN, R. B. 2016a. Constraints on the sedimentary input into the Loki's Castle hydrothermal system (AMOR) from B isotope data. *Chemical Geology,* 443**,** 111-120.

BAUMBERGER, T., FRÜH-GREEN, G. L., THORSETH, I. H., LILLEY, M. D., HAMELIN, C., BERNASCONI, S. M., OKLAND, I. E. & PEDERSEN, R. B. 2016b. Fluid composition of the sediment-influenced Loki's Castle vent field at the ultra-slow spreading Arctic Mid-Ocean Ridge. *Geochimica et Cosmochimica Acta,* 187**,** 156-178.

BOONNAWA, C., VIFLOT, T., PEREIRA, S., BARREYRE, T., JAMIESON, J., SCHEFFLER, J., MECKEL, E., ROSNER, M., REEVES, E. P., et al. Diverse styles of hydrothermal activity on the ultraslow Arctic Mohn's Ridge: the Fåvne, Ægir and Loki's Castle vent fields. *In preparation for EPSL*.

BREKKE, H., STENLØKK, J., ERIKSEN, S. H., BJØRNSTAD, A., SANDSTÅ, N. R., SOLVI, K. & SCHIAGER, P. 2021. *Deep Sea Minerals on the Norwegian Continental Shelf–Developments in Exploration* [Online]. Norwegian Petroleum Directorate. Available:https://www.npd.no/globalassets/1-npd/fakta/havbunnsmineraler/presentation-deep-sea-minerals-developments-in-exploration-harald-brekke-with-text.pdf [Accessed 03.05.2022].

CANFIELD, D. E., RAISWELL, R., WESTRICH, J. T., REAVES, C. M. & BERNER, R. A. 1986. The use of chromium reduction in the analysis of reduced inorganic sulfur in sediments and shales. *Chemical geology,* 54**,** 149-155.

DICK, H. J., LIN, J. & SCHOUTEN, H. 2003. An ultraslow-spreading class of ocean ridge. *Nature,* 426**,** 405-412.

DUCKWORTH, R. C., KNOTT, R., FALLICK, A. E., RICKARD, D., MURTON, B. J. & VAN DOVER, C. 1995. Mineralogy and sulphur isotope geochemistry of the Broken Spur sulphides, 29 N, Mid-Atlantic Ridge. *Geological Society, London, Special Publications,* 87**,** 175-189.

EDMONDS, H., MICHAEL, P., BAKER, E., CONNELLY, D., SNOW, J., LANGMUIR, C., DICK, H., MÜHE, R., GERMAN, C. & GRAHAM, D. 2003. Discovery of abundant hydrothermal venting on the ultraslow-spreading Gakkel ridge in the Arctic Ocean. *Nature,* 421**,** 252-256.

EICKMANN, B., BAUMBERGER, T., THORSETH, I. H., STRAUSS, H., FRUEH-GREEN, G. L., PEDERSEN, R. B. & JAESCHKE, A. 2020. Sub-seafloor sulfur cycling in a low-temperature barite field: A multi-proxy study from the Arctic Loki's Castle vent field. *Chemical Geology,* 539**,** 119495.

EICKMANN, B., THORSETH, I., PETERS, M., STRAUSS, H., BRÖCKER, M. & PEDERSEN, R. 2014. Barite in hydrothermal environments as a recorder of subseafloor processes: a multiple-isotope study from the Loki's Castle vent field. *Geobiology,* 12**,** 308-321.

FARQUHAR, J., KIM, S.-T. & MASTERSON, A. 2007. Implications from sulfur isotopes of the Nakhla meteorite for the origin of sulfate on Mars. *Earth and Planetary Science Letters,* 264**,** 1-8.

FARQUHAR, J. & WING, B. A. 2003. Multiple sulfur isotopes and the evolution of the atmosphere. *Earth and Planetary Science Letters,* 213**,** 1-13.

FOSSING, H. & JØRGENSEN, B. B. 1989. Measurement of bacterial sulfate reduction in sediments: evaluation of a single-step chromium reduction method. *Biogeochemistry,* 8**,** 205-222.

HANNINGTON, M. D., DE RONDE, C. E. & PETERSEN, S. 2005. Sea-floor tectonics and submarine hydrothermal systems.

HANOR, J. S. 2000. Barite–celestine geochemistry and environments of formation. *Reviews in Mineralogy and Geochemistry,* 40**,** 193-275.

HERZIG, P., HANNINGTON, M. & ARRIBAS JR, A. 1998. Sulfur isotopic composition of hydrothermal precipitates from the Lau back-arc: implications for magmatic contributions to seafloor hydrothermal systems. *Mineralium Deposita,* 33**,** 226-237.

HOEFS, J. 2018. Stable isotope geochemistry (p. 437). Springer-Verlag.

HULSTON, J. & THODE, H. 1965. Variations in the S33, S34, and S36 contents of meteorites and their relation to chemical and nuclear effects. *Journal of Geophysical Research,* 70**,** 3475-3484.

JOHANNESSEN, K. C., VANDER ROOST, J., DAHLE, H., DUNDAS, S. H., PEDERSEN, R. B. & THORSETH, I. H. 2017. Environmental controls on biomineralization and Fe-mound formation in a low-temperature hydrothermal system at the Jan Mayen Vent Fields. *Geochimica et Cosmochimica Acta,* 202**,** 101-123.

JOHNSON, O. 2004. *Minerals of the World,* New Jersey, Princeton University Press.

KASE, K., YAMAMOTO, M. & SHIBATA, T. 1990. Copper-rich sulfide deposit near 23 N, Mid-Atlantic Ridge: chemical composition, mineral chemistry, and sulfur isotopes.

KRITSOTAKIS, K. & VON PLATEN, H. 1980. Reduktive barytmobilisation.

LABIDI, J., CARTIGNY, P., BIRCK, J., ASSAYAG, N. & BOURRAND, J. 2012. Determination of multiple sulfur isotopes in glasses: A reappraisal of the MORB δ34S. *Chemical Geology,* 334**,** 189-198.

LAFEMINA, P. C. 2015. Plate tectonics and volcanism. *The encyclopedia of volcanoes.* Elsevier.

LEIN, A. Y., ULYANOVA, N., ULYANOV, A., CHERKASHEV, G. & STEPANOVA, T. 2001. Mineralogy and geochemistry of sulfide ores in ocean-floor hydrothermal fields associated with serpentinite protrusions. *Russian Journal of Earth Sciences,* 3.

MARQUES, A. F. A., ROERDINK, D. L., BAUMBERGER, T., DE RONDE, C. E., DITCHBURN, R. G., DENNY, A., THORSETH, I. H., OKLAND, I., LILLEY, M. D. & WHITEHOUSE, M. J. 2020. The seven sisters hydrothermal system: First record of shallow hybrid mineralization hosted in mafic volcaniclasts on the arctic mid-ocean ridge. *Minerals,* 10**,** 439.

MCDERMOTT, J. M., ONO, S., TIVEY, M. K., SEEWALD, J. S., SHANKS III, W. C. & SOLOW, A. R. 2015. Identification of sulfur sources and isotopic equilibria in submarine hot-springs using multiple sulfur isotopes. *Geochimica et Cosmochimica Acta,* 160**,** 169-187.

OHMOTO, H. & LASAGA, A. C. 1982. Kinetics of reactions between aqueous sulfates and sulfides in hydrothermal systems. *Geochimica et Cosmochimica Acta,* 46**,** 1727-1745.

OHMOTO, H., MIZUKAMI, M., DRUMMOND, S., ELDRIDGE, C., PISUTHA-ARNOND, V. & LENAGH, T. 1983. Chemical processes of Kuroko formation.

ONO, S., SHANKS III, W. C., ROUXEL, O. J. & RUMBLE, D. 2007. S-33 constraints on the seawater sulfate contribution in modern seafloor hydrothermal vent sulfides. *Geochimica et Cosmochimica Acta,* 71**,** 1170-1182.

ONO, S., WING, B., JOHNSTON, D., FARQUHAR, J. & RUMBLE, D. 2006. Mass-dependent fractionation of quadruple stable sulfur isotope system as a new tracer of sulfur biogeochemical cycles. *Geochimica et Cosmochimica Acta,* 70**,** 2238-2252.

PEDERSEN, R., THORSETH, I., HELLEVANG, B., SCHULTZ, A., TAYLOR, P., KNUDSEN, H. & STEINSBU, B. Two vent fields discovered at the ultraslow spreading Arctic ridge system. AGU Fall Meeting Abstracts, 2005. OS21C-01.

PEDERSEN, R. B. & BAUMBERGER, T. 2011. Cruise Report Jan Mayen vent fields (JMVF); R/V GO Sars, Expedition No. 2011108/CGB2011, 10.–22. June 2011, Bergen–Bergen, Norway.

PEDERSEN, R. B. & BJERKGÅRD, T. 2016. Seafloor massive sulphides in Arctic waters. *Mineral Resources In The Arctic,* 1**,** 209-216.

PEDERSEN, R. B., RAPP, H. T., THORSETH, I. H., LILLEY, M. D., BARRIGA, F. J., BAUMBERGER, T., FLESLAND, K., FONSECA, R., FRÜH-GREEN, G. L. & JORGENSEN, S. L. 2010a. Discovery of a black smoker vent field and vent fauna at the Arctic Mid-Ocean Ridge. *Nature communications,* 1**,** 1-6.

PEDERSEN, R. B., THORSETH, I. H., NYGÅRD, T. E., LILLEY, M. D. & KELLEY, D. S. 2010b. Hydrothermal activity at the Arctic mid-ocean ridges. *Washington DC American Geophysical Union Geophysical Monograph Series,* 188**,** 67-89.

PETERS, M., STRAUSS, H., FARQUHAR, J., OCKERT, C., EICKMANN, B. & JOST, C. L. 2010. Sulfur cycling at the Mid-Atlantic Ridge: A multiple sulfur isotope approach. *Chemical Geology,* 269**,** 180-196.

REEVES, E. P., SEEWALD, J. S., SACCOCIA, P., BACH, W., CRADDOCK, P. R., SHANKS, W. C., SYLVA, S. P., WALSH, E., PICHLER, T. & ROSNER, M. 2011. Geochemistry of hydrothermal fluids from the PACMANUS, Northeast Pual and Vienna Woods hydrothermal fields, Manus basin, Papua New Guinea. *Geochimica et Cosmochimica Acta,* 75**,** 1088-1123.

RICKARD, D. 2012. *Sulfidic sediments and sedimentary rocks*, Newnes.

ROERDINK, D. L., MASON, P. R., FARQUHAR, J. & REIMER, T. 2012. Multiple sulfur isotopes in Paleoarchean barites identify an important role for microbial sulfate reduction in the early marine environment. *Earth and Planetary Science Letters,* 331**,** 177-186.

RONA, P., KLINKHAMMER, G., NELSEN, T., TREFRY, J. & ELDERFIELD, H. 1986. Black smokers, massive sulphides and vent biota at the Mid-Atlantic Ridge. *Nature,* 321**,** 33-37.

SEAL, R. R. 2006. Sulfur isotope geochemistry of sulfide minerals. *Reviews in mineralogy and geochemistry,* 61**,** 633-677.

SEEWALD, J. S., DOHERTY, K. W., HAMMAR, T. R. & LIBERATORE, S. P. 2002. A new gas-tight isobaric sampler for hydrothermal fluids. *Deep Sea Research Part I: Oceanographic Research Papers,* 49**,** 189-196.

SHANKS, W. C., BISCHOFF, J. L. & ROSENBAUER, R. J. 1981. Seawater sulfate reduction and sulfur isotope fractionation in basaltic systems: interaction of seawater with fayalite and magnetite at 200–350 C. *Geochimica et Cosmochimica Acta,* 45**,** 1977-1995.

SHARP, Z. 2017. Principles of stable isotope geochemistry.

STENSLAND, A., BAUMBERGER, T., LILLEY, M. D., OKLAND, I. E., DUNDAS, S. H., ROERDINK, D. L., THORSETH, I. H. & PEDERSEN, R. B. 2019. Transport of carbon dioxide and heavy metals from hydrothermal vents to shallow water by hydrate-coated gas bubbles. *Chemical Geology,* 513**,** 120-132.

TAN, P., BREIVIK, A. J., TRØNNES, R. G., MJELDE, R., AZUMA, R. & EIDE, S. 2017. Crustal structure and origin of the Eggvin Bank west of Jan Mayen, NE Atlantic. *Journal of Geophysical Research: Solid Earth,* 122**,** 43-62.

TAO, C., LIN, J., GUO, S., CHEN, Y. J., WU, G., HAN, X., GERMAN, C. R., YOERGER, D. R., ZHOU, N. & LI, H. 2012. First active hydrothermal vents on an ultraslow-spreading center: Southwest Indian Ridge. *Geology,* 40**,** 47-50.

TIVEY, M. K. 2007. Generation of seafloor hydrothermal vent fluids and associated mineral deposits. *Oceanography,* 20**,** 50-65.

VIFLOT, T. Ø. 2019. *Evidence for extensive conductive cooling and microbial carbon transformations in diffuse hydrothermal fluids from the Loki's Castle Vent Field.* Msc, University of Bergen.

WHITNEY, D. L. & EVANS, B. W. 2010. Abbreviations for names of rock-forming minerals. *American mineralogist,* 95**,** 185-187.

YEO, I. A., CW, D., LEBAS, T., AUGUSTIN, N. & STEINFÜHRER, A. 2016. Segment-scale volcanic episodicity: evidence from the North Kolbeinsey Ridge, Atlantic. *Earth and Planetary Science Letters,* 439**,** 81-87.

APPENDIXES

Appendix 1 – Standards used for multiple sulfur isotope analysis on chimney samples

Appendix 2 – Multiple sulfur isotope analysis on chimney samples

Appendix 3 – Multiple sulfur isotope analysis on fluid samples

Appendix 1 – Standards used for multiple sulfur isotope analysis on chimney samples

Run	**5040**	**5021**	**5052**	**5063**	**5074**	**5085**	**4956**	**4998**	**5019**
Reactor	1	2	3	4	5	6	7	9	10
Sample	IAEA-S1	IAEA-S1	IAEA-S1	IAEA-S1	IAEA-S1	IAEA-S1	IAEA-S1	IAEA-S1	IAEA-S1
m(Ag_2S) [mg]	2,884	2,743	2,695	2,846	2,905	2,753	2,820	3,124	2,719
p(F_2) [mbar]	30	30	30	30	30	30	30	30	30
Date analysis	02.09.21	22.07.21	07.09.21	21.09.21	23.09.21	28.09.21	15.06.21	13.07.21	20.07.21
p(SF_6, front MS) [mbar]	4,0	3,9	3,9	4,0	4,0	4,0	3,9	4,1	3,9
$\delta^{33}S$ [‰]	-0,868	-0,862	-0,832	-0,869	-0,833	-0,814	-0,820	-0,872	-0,882
$\delta^{34}S$ [‰]	-1,851	-1,802	-1,751	-1,823	-1,760	-1,715	-1,765	-1,822	-1,836
$\delta^{36}S$ [‰]	-3,010	-3,111	-2,930	-3,056	-2,993	-2,916	-3,246	-3,531	-3,262
s($\delta^{33}S$) [‰]	0,013	0,009	0,007	0,013	0,015	0,005	0,024	0,013	0,007
s($\delta^{34}S$) [‰]	0,005	0,007	0,010	0,008	0,005	0,006	0,009	0,006	0,008
s($\delta^{36}S$) [‰]	0,063	0,071	0,044	0,070	0,106	0,061	0,098	0,086	0,058
$\delta^{33}S$ vs S1 [‰]	*-0,868*	*-0,862*	*-0,832*	*-0,869*	*-0,833*	*-0,814*	*-0,820*	*-0,872*	*-0,882*
$\delta^{34}S$ vs S1 [‰]	*-1,851*	*-1,802*	*-1,751*	*-1,823*	*-1,760*	*-1,715*	*-1,765*	*-1,822*	*-1,836*
$\delta^{36}S$ vs S1 [‰]	*-3,010*	*-3,111*	*-2,930*	*-3,056*	*-2,993*	*-2,916*	*-3,246*	*-3,531*	*-3,262*
$\delta^{33}S$ vs CDT [‰]	*-0,923*	*-0,917*	*-0,887*	*-0,924*	*-0,888*	*-0,869*	*-0,875*	*-0,927*	*-0,937*
$\delta^{34}S$ vs CDT [‰]	***-2,150***	***-2,101***	***-2,050***	***-2,122***	***-2,059***	***-2,014***	***-2,064***	***-2,121***	***-2,135***
$\delta^{36}S$ vs CDT [‰]	*-4,376*	*-4,477*	*-4,296*	*-4,422*	*-4,359*	*-4,282*	*-4,612*	*-4,896*	*-4,628*
$\Delta^{33}S$ [‰]	*0,185*	*0,166*	*0,170*	*0,170*	*0,173*	*0,169*	*0,189*	*0,166*	*0,163*
$\Delta^{36}S$ [‰]	-0,294	-0,488	-0,404	-0,393	-0,450	-0,458	-0,693	-0,869	-0,574

Appendix 2 – Multiple sulfur isotope analysis on chimney samples

Run	Series	Reactor	Sample name				Date loading	m(Ag_2S) [mg]	p(F_2) [mbar]	Date analysis	T(dist.) [°C]	t(dist.) [min]	p(dist.) [mbar]	n(SF_6, MS) [µmol]	Yield [%]	p(SF_6, front MS) [mbar]	$\delta^{33}S$ vs CDT [‰]	$\delta^{34}S$ vs CDT [‰]	$\delta^{36}S$ vs CDT [‰]	log $\Delta^{33}S$ [‰]	log $\Delta^{36}S$ [‰]
5061	497	2	GS17-	ROV17-	R01-	A0	20.09.21	2,851	30	21.09.21	-124,6	10	3,9E-02	10,7	93,0	4,0	*-0,055*	***-0,300***	*-1,370*	*0,100*	-0,800
5062	497	3	GS17-	ROV17-	R01-	A1	20.09.21	3,082	30	21.09.21	-129,0	10	3,1E-02	10,7	86,0	4,0	*-0,055*	***-0,300***	*-1,370*	*0,100*	-0,800
5064	497	5	GS17-	ROV17-	R01-	A2	20.09.21	3,001	30	21.09.21	-125,2	10	3,3E-02	11,0	90,8	4,1	*-0,055*	***-0,300***	*-1,370*	*0,100*	-0,800
5065	497	6	GS17-	ROV17-	R01-	A3	20.09.21	3,075	30	21.09.21	-123,4	10	3,6E-02	11,0	88,6	4,1	*-0,055*	***-0,300***	*-1,370*	*0,100*	-0,800
5066	497	7	GS17-	ROV19-	R02-	C0	20.09.21	3,166	30	21.09.21	-120,8	10	2,8E-02	11,0	86,1	4,1	*-0,055*	***-0,300***	*-1,370*	*0,100*	-0,800
5067	497	8	GS17-	ROV19-	R02-	C1	20.09.21	3,042	30	21.09.21	-128,1	15	3,1E-02	10,7	87,2	4,0	*-0,055*	***-0,300***	*-1,370*	*0,100*	-0,800
5068	497	9	GS17-	ROV19-	R03-	D0	20.09.21	3,170	30	21.09.21	-125,8	10	3,8E-02	11,0	86,0	4,1	*-0,055*	***-0,300***	*-1,370*	*0,100*	-0,800
5069	497	10	GS17-	ROV19-	R03-	D1	20.09.21	2,779	30	21.09.21	-125,8	10	2,5E-02	10,7	95,4	4,0	*-0,055*	***-0,300***	*-1,370*	*0,100*	-0,800
5070	498	1	GS18-	ROV08-	R01-	E0	22.09.21	1,186	30	23.09.21	-124,0	10	3,7E-02	7,1	148,3	2,8	*-0,055*	***-0,300***	*-1,370*	*0,100*	-0,800
5076	498	7	GS18-	ROV08-	R05-	F0	22.09.21	3,146	30	23.09.21	-127,1	10	3,5E-02	11,0	86,6	4,1	*-0,055*	***-0,300***	*-1,370*	*0,100*	-0,800
5077	498	8	GS18-	ROV08-	R05-	F1	22.09.21	3,131	30	23.09.21	-121,7	10	2,6E-02	10,7	84,7	4,0	*-0,055*	***-0,300***	*-1,370*	*0,100*	-0,800
5071	498	2	GS18-	ROV14-	R01-	G0	22.09.21	3,114	30	23.09.21	-122,6	10	3,7E-02	11,0	87,5	4,1	*-0,055*	***-0,300***	*-1,370*	*0,100*	-0,800
5072	498	3	GS18-	ROV14-	R01-	G1	22.09.21	3,044	30	23.09.21	-117,0	10	3,1E-02	11,0	89,5	4,1	*-0,055*	***-0,300***	*-1,370*	*0,100*	-0,800
5073	498	4	GS18-	ROV14-	R03-	H0	22.09.21	3,023	30	23.09.21	-125,0	10	2,4E-02	11,0	90,2	4,1	*-0,055*	***-0,300***	*-1,370*	*0,100*	-0,800
5075	498	6	GS18-	ROV14-	R03-	H1	22.09.21	3,013	30	23.09.21	-121,4	10	2,7E-02	11,0	90,5	4,1	*-0,055*	***-0,300***	*-1,370*	*0,100*	-0,800
5078	498	9	GS18-	ROV22-	R02-	K0	22.09.21	3,039	30	23.09.21	-124,3	15	2,7E-02	11,0	89,7	4,1	*-0,055*	***-0,300***	*-1,370*	*0,100*	-0,800
5079	498	10	GS18-	ROV22-	R02-	K1	22.09.21	2,912	30	23.09.21	-122,0	10	2,6E-02	10,7	91,1	4,0	*-0,055*	***-0,300***	*-1,370*	*0,100*	-0,800
5080	499	1	GS19-	ROV16-	R02-	M0	27.09.21	2,872	30	28.09.21	-123,0	10	3,2E-02	10,7	92,3	4,0	*-0,055*	***-0,300***	*-1,370*	*0,100*	-0,800
5081	499	2	GS19-	ROV16-	R02-	M1	27.09.21	3,049	30	28.09.21	-127,9	10	3,9E-02	10,7	87,0	4,0	*-0,055*	***-0,300***	*-1,370*	*0,100*	-0,800
5082	499	3	GS19-	ROV16-	R02-	M2	27.09.21	2,891	30	28.09.21	-120,2	10	3,4E-02	10,7	91,7	4,0	*-0,055*	***-0,300***	*-1,370*	*0,100*	-0,800
5083	499	4	GS19-	ROV20-	R01-	N0	27.09.21	2,892	30	28.09.21	-121,6	10	2,9E-02	10,7	91,7	4,0	*-0,055*	***-0,300***	*-1,370*	*0,100*	-0,800
5084	499	5	GS19-	ROV20-	R01-	N1	27.09.21	2,788	30	28.09.21	-130,1	10	2,9E-02	10,7	95,1	4,0	*-0,055*	***-0,300***	*-1,370*	*0,100*	-0,800

Appendix 3 – Multiple sulfur isotope analysis on fluid samples

Run	Sample name	Date loading	m(Ag_2S) [mg]	p(F_2) [mbar]	Date analysis	log Δ33S [‰]	Δ36S [‰]	δ34S vs VCDT [‰]
4880	IAEA-S1	28.04.21	2,729	30	29.04.21	*0,065*	-0,655	*-0,256*
4903	IAEA-S1	17.05.21	2,558	30	18.05.21	*0,070*	-0,548	*-0,253*
4920	IAEA-S1	26.05.21	3,050	30	27.05.21	*0,066*	-0,917	*-0,239*
4928	GS17-ROV17-IGT3	26.05.21	2,865	30	27.05.21	*-0,018*	-0,191	*4,147*
4929	GS17-ROV17-IGT2	26.05.21	2,882	30	27.05.21	*-0,023*	0,134	*4,333*
4940	IAEA-S1	09.06.21	3,530	30	10.06.21	*0,060*	-0,975	*-0,236*
4941	GS17-ROV19-IGT2	09.06.21	2,911	30	10.06.21	*-0,029*	0,238	*4,791*
4942	GS17-ROV19-IGT3	09.06.21	2,878	30	10.06.21	*-0,017*	0,019	*4,446*
4943	GS17-ROV19-IGT4+ROV21-IGT4	09.06.21	2,929	30	10.06.21	*-0,026*	0,038	*4,161*
4944	GS18-ROV14-IGT1+IGT2	09.06.21	2,994	30	10.06.21	*-0,022*	-0,043	*2,364*
4945	GS18-ROV14-IGT3+IGT4	09.06.21	2,902	30	10.06.21	*-0,011*	0,079	*3,724*